Hybrid Perovskites for Photovoltaic Applications

Doctoral Thesis

Author:
Alexander Wyn Stewart

Supervisors:
Prof. Bernabé Marí Soucase
Prof. Davide Raffaele Ceratti

Tutor:
Prof. Bernabé Marí Soucase

December, 2023

"For a successful technology, reality must take precedence over public relations, for Nature cannot be fooled."

Richard P. Feynman

Abstract

Halide perovskite solar cells (HaPSCs) have become one of the leading candidates for the production of next generation photovoltaic devices. However, commercialisation requires them to meet stringent demands in terms of performance, safety and longevity. The intrinsic stability of halide perovskites is known to be closely related to defect chemistries occurring within them since some defects can participate in, or initiate, degradation processes. Moreover, some common defects in these systems create electronically active shallow trap states, which can influence key processes such as charge transport and recombination - making them key in determining device performance.

Solvent engineering has gained relevance as a technique for controlling the crystallisation of halide perovskite thin films, leading to experimentally observable improvements in crystal quality and stability as well as meaningful reductions in defect densities. Despite substantial recent efforts into developing HaPSCs, the performance and stability of wide-bandgap compositions has lagged behind those suitable for single-junction devices. The aim of this thesis is to address this problem by developing experimental techniques for improving mix-halide inorganic perovskites.

Although solvent engineering can introduce, reduce or passivate electronically active defects (dopants) in halide perovskites, there have been relatively few investigations into the physics occurring in doped systems. Moreover, the active chemistries in these systems, which are still under investigation, can result in transient behaviours or the activation of complex processes - complicating experimental efforts. In this thesis, these problems are overcome by employing computer simulations to investigate the origin and factors giving rise to optimal doping levels in HaPSCs.

This doctoral thesis is made up of three articles which have been published in indexed journals. Two of these develop experimental techniques for controlling the film crystallisation and stability of wide-bandgap perovskites. The third article investigates the role of electronic dopants in determining device performance, and how they may be harnessed to produce superior HaPSCs. Together, these results generate new insights and provide techniques for experimentalists working with high performance devices.

Resumen

Las células solares de perovskitas de haluros (HaPSC) se han convertido en uno de los principales candidatos para la producción de dispositivos fotovoltaicos de nueva generación. Sin embargo, su comercialización exige que cumplan estrictos requisitos de rendimiento, seguridad y longevidad. Se sabe que la estabilidad intrínseca de las perovskitas de haluro está estrechamente relacionada con la química de los defectos que se producen en su interior, ya que algún defecto puede participar o iniciar procesos de degradación. Además, algunos de los defectos más comunes en estos sistemas crean estados de trampa poco profundos y electrónicamente activos, que pueden influir en procesos clave como el transporte y recombinación de cargas, lo que los convierte en fundamentales para determinar el rendimiento de los dispositivos.

La ingeniería de disolventes ha cobrado importancia como técnica para controlar la cristalización de películas delgadas de haluros de perovskita, lo que ha dado lugar a mejoras experimentalmente observables en la calidad y estabilidad de los cristales, así como a reducciones significativas en las densidades de defectos. A pesar de los importantes esfuerzos realizados recientemente para desarrollar las HaPSC, el rendimiento y la estabilidad de las composiciones con bandas prohibidas anchas han quedado rezagados con respecto a las composiciones para los dispositivos de unión única. El objetivo de esta tesis es abordar este problema desarrollando técnicas experimentales para mejorar las perovskitas inorgánicas de haluros mixtos.

Aunque la ingeniería de disolventes puede introducir, reducir o pasivar defectos electrónicamente activos (dopantes) en las perovskitas de haluro, se han realizado relativamente pocas investigaciones sobre los procesos físicos que se producen en los sistemas dopados. Además, las químicas activas de estos sistemas, que aún se están investigando, pueden dar lugar a comportamientos transitorios o a la activación de procesos complejos, lo que complica los esfuerzos experimentales. En esta tesis, estos problemas se superan empleando simulaciones por ordenador para investigar el origen y los factores que dan lugar a niveles óptimos de dopaje en las HaPSCs.

Esta tesis doctoral se compone de tres artículos que han sido publicados en revistas indexadas. Dos de ellos desarrollan técnicas experimentales para controlar la cristalización de la película y la estabilidad de las perovskitas

de bandas prohibidas anchas. El tercer artículo investiga el papel que desempeñan los dopantes electrónicos en el rendimiento de los dispositivos y cómo pueden aprovecharse para producir HaPSC superiores. En conjunto, estos resultados aportan nuevos conocimientos y técnicas a los experimentadores que trabajan con dispositivos de alto rendimiento.

Resum

Les cèl·lules solars de perovskita d'halur (HaPSC) s'han convertit en un dels principals candidats per a la producció de dispositius fotovoltaics de nova generació. Tanmateix, la seua comercialització requereix que compleixen exigències estrictes en termes de rendiment, seguretat i longevitat. Se sap que l'estabilitat intrínseca de les perovskites d'halur està estretament relacionada amb les químiques de defectes que es produeixen dins d'elles, ja que algun defecte pot participar o iniciar processos de degradació. A més, alguns defectes predominants en aquests sistemes creen estats de trampa poc profunds i electrònicament actius, que poden influir en processos clau com el transport i la recombinació de càrregues, fent-los clau per determinar el rendiment dels dispositius.

L'enginyeria de dissolvents ha guanyat rellevància com a tècnica per controlar la cristal·lització de pel·lícules primes de perovskita d'halur, donant lloc a millores experimentalment observables en la qualitat i l'estabilitat dels cristalls, així com a reduccions significatives de la densitat de defectes. Malgrat els esforços recents substancials per desenvolupar les HaPSC, el rendiment i l'estabilitat de les composicions de bandes prohibides amples s'han quedat per darrere de les adequades per a dispositius d'unió única. L'objectiu d'aquesta tesi és abordar aquest problema mitjançant el desenvolupament de tècniques experimentals per millorar les perovskites inorgàniques d'halur mixtos.

Tot i que l'enginyeria de dissolvents pot introduir, reduir o passivar defectes electrònicament actius (dopants) en perovskites d'halur, hi ha hagut relativament poques investigacions sobre els processos físics que es produeixen en sistemes dopats. A més, les químiques actives d'aquests sistemes, que encara s'estan investigant, poden donar lloc a comportaments transitoris o a l'activació de processos complexos, cosa que complica els esforços experimentals. En aquesta tesi, aquests problemes es superen mitjançant l'ús de simulacions per ordinador per investigar l'origen i els factors que donen lloc a nivells òptims de dopatge en les HaPSC.

Aquesta tesi doctoral està formada per tres articles que s'han publicat en revistes indexades. Dos d'aquests desenvolupen tècniques experimentals per controlar la cristal·lització de la pel·lícula i l'estabilitat de les perovskites de bandes prohibides amples. El tercer article investiga el paper que tenen

els dopants electrònics a l'hora de determinar el rendiment dels dispositius i com es poden aprofitar per produir HaPSC superiors. En conjunt, aquests resultats generen noves idees i proporcionen tècniques per als experimentadors que treballen amb dispositius d'alt rendiment.

Acknowledgments

I feel very fortunate to have reached the point in my academic life where I can be writing the acknowledgement section of my doctoral thesis. Especially since its success, and enjoyability, has hinged on the input of many people.

Firstly, I would like to thank my supervisors Bernabé Marí Soucase and Davide Raffaele Ceratti for giving me the opportunity to carry out a very active PhD. Their support made it possible for me to work and learn alongside great scientists, in a range of top-institutions, across several countries. I would also like to thank my supervisors for the academic freedom which I have had over these past years, which has allowed me to develop new ideas and techniques that I have come across as a researcher. Many of these projects have not yet been finalised, and so they are not included in the doctoral thesis, however I hope they will become part of a long-term collaboration between me and my supervisors.

Secondly, I would like to thank my family for their support. Without it, I would not be where I am today. In particular, I would like to thank my sister for providing her valuable insight and proof reading all my work, including papers, grants, and other scientific documents, for almost a decade.

Lastly, I would like to thank my colleagues and the invaluable collaborations I have had over these past few years. Not only have they been central to my ability to produce high quality scientific work, but they have also been a source of great happiness and enjoyment in my life.

Contents

Chapter 1

Introduction

1.1 The Climate Crisis

Human-induced climate change poses an imminent threat to humanity and ecosystems around the world. Evidence of this threat can be seen in the increasing species extinction rates, the proliferation of animal and plant diseases, global-scale ecosystem degradation and the deterioration of key ecosystem services [1]. Concurrently, climate change-induced forces threaten basic human needs, with roughly half of Earth's population now experiencing severe water scarcity at least one month per year and 30% of global crop and livestock areas predicted to become unsuitable by 2100 [2]. Climate change has also adversely affected human health - both physically and mentally - globally, with a predicted 250,000 deaths per year attributable to climate change, by 2050 [3]. The mounting evidence has led to climate change being identified as the problem of the century, with the livelihoods of many species hinging on a successful Green Energy Transition.

Large-scale greenhouse gas emissions are the primary driver of human-induced climate change. These gases absorb terrestrial radiation, some of which is re-emitted towards Earth's surface. In 2021 record concentrations of CO_2, CH_4 and N_2O (a.k.a. "The Big Three") were broken [4]. This contributed towards the hottest day and month, since records began, that occurred in June 2023 [5]. In 2019, 77% of the EU's greenhouse gas emissions came from energy production [6], demonstrating the urgent need for large-scale deployment of renewable energy sources. Photovoltaic (PV) and wind-based systems are predicted to become the leading sources of electricity globally, with each generating over 23000TWh yearly by 2050, a number equivalent to about 90% of worldwide electricity production in 2020 [7].

PV systems are one of the most promising solutions for sustainable electricity production due to their reliability and low-cost [8]. In 2021, the total value of PV-related trade reached USD 40 billion [9] – and this is only projected to increase further [10]. As it stands, more than 95% of

global production is based on crystalline silicon (c-Si), with cadmium telluride (CdTe) and other PV technologies making up the rest [8, 9]. The c-Si market domination originates from a culmination of desirable properties, such as the abundance and nontoxicity of silicon, as well as due to circumstantial reasons such as the early invention and the parallel development of the microelectronic industry [11]. Although c-Si has become the workhorse of the PV industry, c-Si solar cells have several drawbacks including their indirect bandgap and energy intensive production. In 2021, an estimated 100TWh of energy was used for making c-Si modules which is comparable to the total energy demand of Croatia during the same period [9]. This energy demand is driven by the complex production steps in extracting and refining PV-grade silicon [12]. Recently, a high reliance on a small number of intercontinental supply chains, raw material costs, supply issues and end-of-life management of c-Si solar cells have all become crucial problems to address.

One particularly concerning problem is the large quantities of PV panels that will be decommissioned in future years, projected to be 8 million tonnes globally by 2030 [13]. Currently, recycling capacity is unable to meet this demand [14] or recover all components efficiently [15], meaning that technologies which address this problem, including alternative more-recyclable PV materials, are urgently needed.

Another pressing matter is related to production inputs, with raw materials making up 35-50% of the total c-Si module cost in 2021 [9]. The demand for raw materials is set to experience unprecedented growth due to the burgeoning PV industry. Mining projects tend to have long lead times, which can cause supply and demand mismatches. By 2050, the PV industry's demand for silver is set to exceed the total production of silver in 2020 by almost 30% [7]. The production of polysilicon, which is a high purity form of polycrystalline silicon, has also caused bottlenecks in c-Si PV production several times, both in 2015 and in 2021, leading to polysilicon prices quadrupling to around USD 35/kg in the last quarter of 2021 [9]. To make the Green Energy Transition as robust as possible it would be better to have a selection of other economically viable inputs which would likely involve the large-scale deployment of alternative PV materials. c-Si raw material production is also primarily controlled by one country, which also plays the leading role in all stages of c-Si solar cell production [9]. This can leave import-reliant countries, such as the EU, USA and India, susceptible to price hikes or stock shortages, planned or otherwise.

In China, extensive state-backed investments and subsidies have led to the continual reduction of costs and the establishment of robust systems benefiting from economies of scale. Nowadays, one out of every seven panels produced worldwide is manufactured by a single Chinese facility [9]. While not inherently bad, unforeseen events, such as COVID-19 and Ukraine war, have shown the potential to create supply chain issues which could threaten a successful Green Energy Transition. The EU has recently introduced several

programs to mitigate these supply chain vulnerabilities, such as the European Commission's Net-Zero Industry Act and the European Solar Manufacturing Council's REPowerEU. These programmes aim to create new supply lines closer to large-scale PV centres in the EU, increasing the EU's energy security and reducing demand on a small number of intercontinental distribution chains associated with purchasing c-Si PV panels from China. Supply chain diversification has the potential to both make the Green Energy Transition more robust and reduce transport-associated emissions. However, to create startups that are competitive with China, novel and disruptive technologies are needed.

PV manufacturing capacity by country and region, 2021
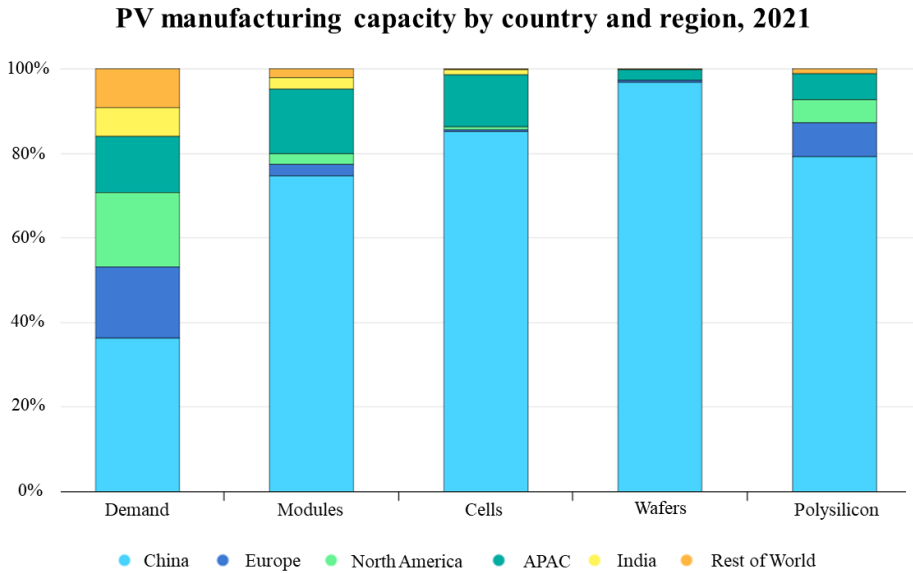

Figure 1: The global demand of crystalline silicon solar cells compared to the location of the production steps required to make them [9].

Third generation PV technology, previous generations being wafer-based and thin film-based c-Si respectively, is based on a large range of advanced thin films. These include hot carrier cells [16, 17], quaternary copper compounds [18, 19], dye-sensitized solar cells [20], plasmonic metal nanostructures [21], and quantum dots [22], among others [23, 24]. In contrast to c-Si, many of these materials have direct bandgaps which mean that solar cell mass can be significantly reduced. Thin films also allow for novel PV applications such as flexible solar cells [25].

One material class that has gained a particularly large amount of interest are metal halide perovskites (HaPs), which offer comparable performance to

c-Si solar cells [26], but at lower costs [27] and with all the advantages that thin film technologies bring. They offer competitive performance in both single-junction architectures, where the HaP absorber layer is sandwiched between two selective contacts, and multi-junction architectures, where multiple single-junction devices are stacked on top of each other in either a two-terminal or four-terminal configuration. While single-junction halide perovskite solar cells (HaPSCs) are already finding their way on to the market for niche applications, such as Saule Technologies solar blinds and electronic shelf labels, there are many companies who believe that perovskite-silicon tandem solar cells hold the key to a new range of highly efficient and inexpensive solar panels. This year, several groups reported perovskite-silicon tandems with power conversion efficiencies superior to 30% for the first time, making them become the most efficient non-concentrator two-junction solar technology [26]. Rather than trying to disrupt the status quo, perovskite-silicon tandems consist of adding a HaPSC onto the c-Si passivated emitter and rear contact (PERC) cells which now dominate the market [28], meaning that they can build upon an already well-developed technology.

HaPSCs are built from abundant raw materials and, while further research is needed, they appear to be straightforwardly recyclable [29]. Leading HaPSC producers, such as Oxford PV, are also already establishing production centres in the EU and US. For these reasons, HaPSCs appear likely to play an important role in the Green Energy Transition, and the fight against human-induced climate change, which will define the future of our planet.

1.2   Halide Perovskite Solar Cells

1.2.1   Perovskite structure and properties

The origins of the perovskite material family can be traced back to the discovery of $CaTiO_3$ in 1839 [30]. However, it was only a century later when Goldschmidt published his work on tolerance factors [31], and barium titanate's crystal structure was measured [32], that the modern basis for the perovskite material family was laid. Nowadays, perovskites are defined as a class of crystalline materials with the chemical formula A^{+n} B^{+2n} $(X^{-n})_3$. We will consider the case $n = 1$, meaning that A and B are monovalent and bivalent cations, and X is an oxide or halide. However, the initial perovskites, such as calcium $CaTiO_3$, had $n = 2$ and the X-site was occupied by oxygen.

The perovskite structure is composed of eight corner-sharing octahedral units BX_6, with an A-site cation sitting between them. In the ideal case, seen in Figure 1, this results in a cubic crystal structure. However, more
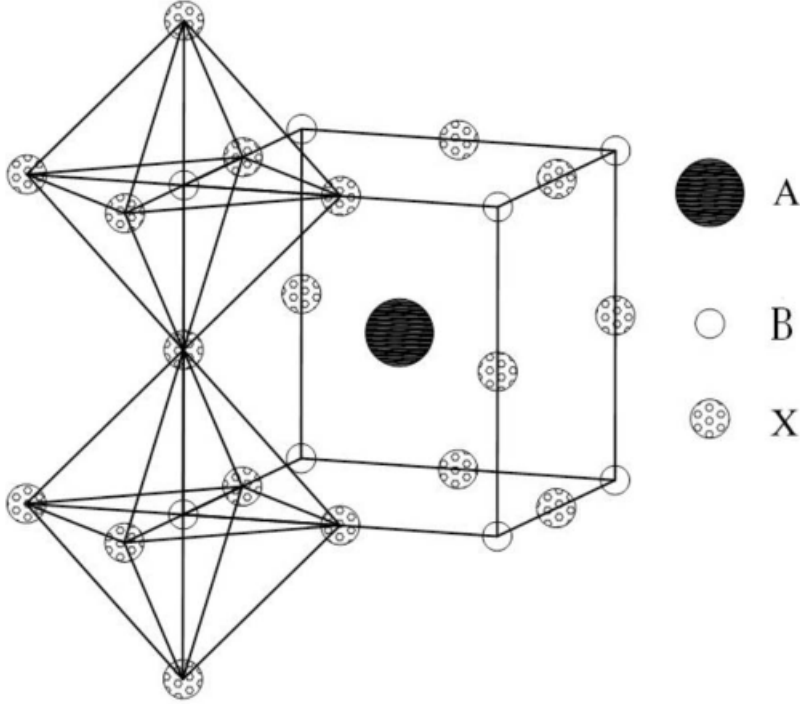
Figure 2: Cubic perovskite structure with the chemical formula ABX_3 [33].

generally, the formability and phase structure of a perovskite crystal depends on the sizes of the constituent cations and ions. This was first shown by Goldschmidt who introduced the semi-empirical tolerance factor α for predicting structure-type based on ionic size mismatch [31]

$$\alpha = \frac{r_A + r_X}{\sqrt{2}(r_B + r_X)})$$ (1.1)

Where r_A, r_B and r_X refer to the ionic radii of the A- and B-site cations and the X-site halide, respectively. Cubic perovskites tend to form for values of α between 0.9-1, whereas decreasing the A site cations size tends to result in a distortion of the lattice for values of α between 0.8-0.89 [34]. These distorted structures are better classified using the concept of octahedral tilting [35]. When the A-site cation is too small to fill the cavity between the BX_6 octahedral units, the octahedra themselves may rotate in order to maintain connectivity. These rotations can be categorised as "in-phase" or "out of phase" depending on whether or not the rotation direction is consistent between different layers.

On the other hand, if the A-site cation is made too large for the cavity between the BX_6 octahedral units, hexagonal structures tend to form with layers of face-sharing octahedra for values of α larger than 1. This is the basis

of low dimensional HaPs, in which the three-dimensional lattice is broken into two-dimensional sheets, wires or dots of BX_6 octahedra surrounded by insulating organic layers [36, 37].
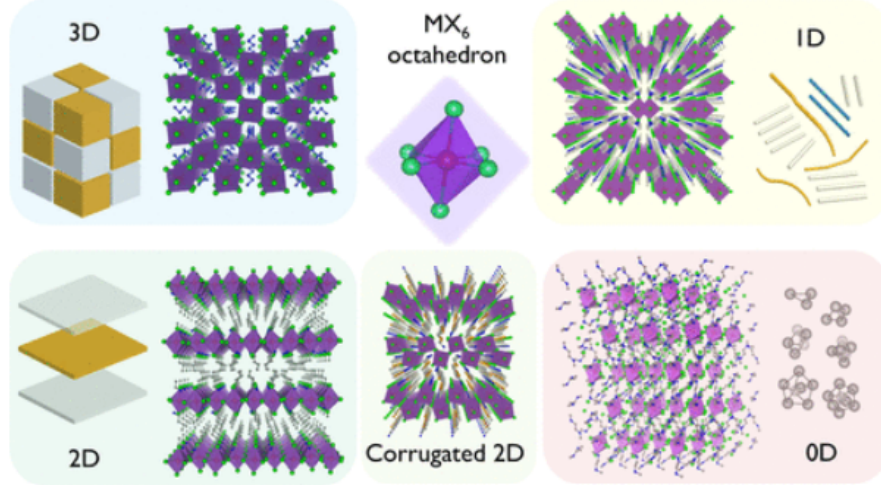

Figure 3: Comparison of 3D, 2D, 1D and 0D halide perovskites [36].

Due to the large range of suitable cations and anions, many intriguing and rich properties have been discovered taking place within perovskites, including colossal magnetoresistance [38], piezoelectricity [39, 40], large dielectric constants [41], ferroelectricity [42], spin-dependent charge transport [43], the thermoelectric effect [44, 45], and superconductivity [46].

Recently, metal halide perovskites (HaPs) have been identified for their useful optoelectronic properties, including direct bandgap, high absorption coefficient and low binding energies [47, 48]. For solution-processed semiconductors they also show unexpectedly low defect densities [49], large carrier diffusion lengths [50, 51] and suitable mobilities [52]. Many of these properties originate in the low bond energies found in these systems, which result in dynamical properties of the ionic HaP lattice which are very different from other high-quality inorganic semiconductors [53].

Defects and ions are known to be mobile in HaPs, leading to a range of electric, photoelectric and structural phenomena. There have been several reports of slow dynamic processes in HaPSCs, which which could be indicative of an accumulation of mobile ions under external electrical bias [54, 55]. Several studies have suggested that mobile ion migration and redistribution near device interfaces can lead to anomalous phenomenon, such as hysteresis [56, 57] and the poor stability of HaPSCs [58, 59]. While mobile ions can lead to current-voltage hysteresis and cause stability issues, they are

also able to passivate defects and interfaces in HaPSCs, leading to improved carrier transport and collection [60] which can improve performance under illumination [61].

Lattice dynamics are also connected to the significant anharmonic effects which occur in HaPs at room temperature [62–65]. This has led to strong electron-phonon interactions being proposed as the origin of the unique opto-electronic properties of HaPs [66]. Electron-phonon interactions can result in the formation of polarons, in which charge carriers are dressed with phonon clouds [67]. The formation of polarons can have wide-ranging effects, including modification of carrier mobilities [68], band-edge optical spectra [53], and carrier cooling [69] in HaPs.

The weak-bonds found in HaPs mean that HaP crystals tend to reach an equilibrium with their environment rather quickly. This results in a set of "self-healable" defects which improve processability via solution-based methods [70–73]. On the other hand, it is also at the heart of the short operational lifespans of HaPSCs, since weak-bonds provide small energy barriers to HaP phase decomposition.

These phenomena have led to a veritable research frenzy into the use of HaPs as emittors [51, 74], LEDs [75–77], photodetectors [78–80], and neuromorphic devices [81–83]. Another particularly promising application is their use as absorber layers in photovoltaic devices, where they have already established themselves as the fastest growing solar technology in terms of efficiency [26]. Simultaneously, they offer an unparalleled level of processability which promises to slash current production costs [27].

1.2.2 Solar cell architecture

The first perovskite-based photovoltaic device was reported in 2009 [84]. These initial perovskite solar cells were liquid-electrolyte-based dye sensitive solar cells, where the perovskite acted as an iodine redox couple. Using this structure, the power conversion efficiencies reached up to 6.5% [85] however they suffered poor device stability. It was the discovery of "mesoscopic" cells, in 2012 [86, 87], which provided the groundwork for modern high-performance devices. These devices did away with liquid electrolytes and adopted a mesoporous electron transport layer which offered both higher device stability and improved performance. Soon after this, the first planar architectures were developed in which no mesoporous scaffold was used [88, 89]. These devices had simpler structures, which led to the cost and complexity of HaPSC production falling steeply [27].
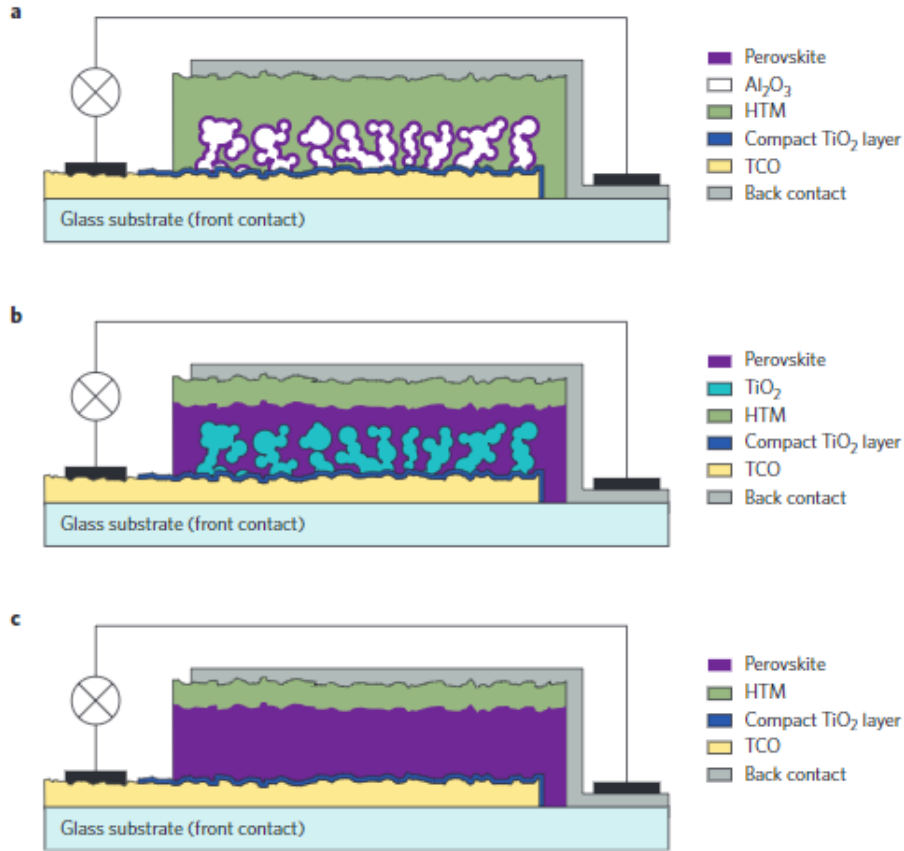
Figure 4: Evolution of HaPSCs. (a) Meso-structured devices inspired by dye-sensitized solar cells. Perovskite acts as the electron conductor. (b) Meso-scopic devices where TiO_2 scaffold is infiltrated by the perovskite, which acts as an electron and hole conductor. (c) Planar hetero-junction devices. [90].

In planar configurations a thin transparent conductive oxide (TCO), deposited on glass, is used a substrate. Upon this, an intrinsic layer of semiconducting HaP (i) is placed, sandwiched between an n-type electron transport layer (ETL) and a p-type hole transporting layer (HTL). Depending on the polarity of the front-facing charge transport layer, a device is called regular or $n - i - p$, if the HaP is deposited onto the ETL, or inverted, or $p - i - n$, if it is deposited on the HTL. For regular architectures, the purpose of the ETL is to act as a selective contact by extracting electrons from the HaP absorber while providing an energy barrier to block hole transport. The ETL also improves contact between the HaP and the electrode and acts as a

nucleation site for perovskite crystal growth [91]. Similarly, the HTL serves as an energy barrier to block electron transport, preventing photo-excited electrons in the HaP recombining with holes in the metal contact. It also improves the contact between the HaP and the electrode, and can serve as a moisture-resistant layer or metal ion diffusion barrier, leading to improved device stability [92].
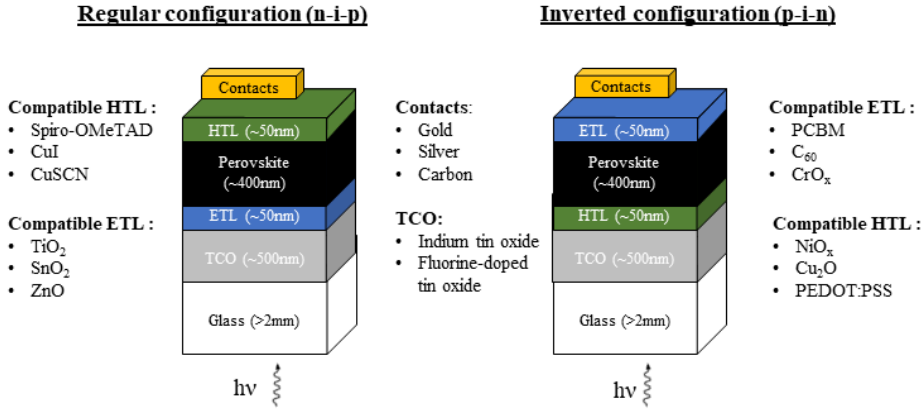

Figure 5: HaPSC stucture and components, with approximate thickness given. The contacts and TCOs used in both architectures are the same, however only some HTLs and ETLs are compatible with certain device configurations.

The heart of the HaPSC is the HaP layer itself, which is where the photo-excited carriers are generated. In planar structures, the HaP layer plays the role of both electron and hole transport material due to its ambipolar semiconducting nature [90]. Initially, all HaPSCs were based on methylamonium lead triiodide $CH_3NH_3PbI_3$ [84], also known as $MAPbI_3$, where $MA^+=CH_3NH_3$. However, in the search for HaPSCs with better performance and durability, other compositions have now been explored. The main constraints placed on these efforts is that the constituent parts of the HaP composition should be compatible in terms of electronic configuration and ionic radii. So far, two other cations which are able to form cubic perovskite structures at room temperature have been discovered, namely caesium Cs^+ and formamidinium $FA^+= CH(NH_2)_2^+$.

Spin-coating is the most common way of producing HaPSCs in laboratory environments due to its versatility, ease of use and the high controllability it offers over film thickness and crystal growth. An overview of

the spin coating technique is provided in "Methods", Section 1.3. While it is often used for deposition of the HaP film, it is also capable of producing high quality ETLs, such as TiO_2 and SnO_2, and HTLs, including spiro-OMeTAD, PEDOT:PSS and PCBM. This means that apart from the deposition of electrical contacts, which is usually carried out using a thermal evaporation process, HaPSC devices can be made entirely using spin coating.

1.2.3 Open questions

Research efforts into HaPSCs have culminated in some of the most efficient single junction devices ever produced [26] which, combined with their low production costs [27, 95, 96], is piquing the interests of entrepreneurs around the world and driving HaPSCs towards large-scale commercialisation. However, there are several points of contention that ought to be resolved before large-scale deployment can take place. These include questions about device stability and toxicity, as well as the means of producing HaPSCs at an industrial scale.

Upscaling technologies

Currently, the upscaling of HaPSCs from small cells to large modules is one of the biggest bottlenecks in large-scale deployment efforts [97]. Historically, all record-breaking efficiency devices have had small active areas of $< 0.1cm^2$ [26], which reflects the fact that it has become standard practice in most research labs to use small cells and measurement conditions which may not accurately represent deployment conditions. The PCE of large devices, with active areas $> 10cm^2$, tends to lag behind record efficiencies by up to 10% [98, 99], although significant progress has been made recently [100]. This is largely due to the widespread use of spin coating which while valuable as a platform for investigating the chemistry and physics of HaP thin films, is unsuitable for producing large substrates [101]. For this reason, in recent years a large effort has been made to develop other deposition techniques such as spray coating [102], blade-coating [103], ink jet printing [104], vacuum flash-assisted methods [105], chemical vapour deposition [106], co-evaporation [107] and slot die coating [108]. Moreover, several of these methods have been shown to be compatible with roll-to-roll production [109–111]. This combined with competitive device performance has led to cost analysis suggesting that HaPSC manufacturing may already be economically feasible using current technologies [95, 96].

Toxicity

Another subject of concern is the toxicity of HaPSCs and their potential impact on humans and ecosystems. High-performance devices tend to be

lead-based [46, 112–114] which is highly toxic to most living creatures [115]. Upon contact with water, hybrid-perovskites convert to PbI_2, a carcinogen, which is banned in many countries [90]. Occupational and environmental exposure to lead can cause neurological deficiencies, reproductive defects, genotoxicity, seizures, and death [116, 117]. The main solution proposed by the scientific community has been to try to replace lead in HaPSCs with other elements [118–122]. However, until now, lead-free devices tend to yield unsatisfactory performances, with the best results coming from tin-based HaPSCs [123–125].

While the biological half-life of tin is lower than lead [126], tin's nontoxicity is far from proven. This was highlighted by the World Health Organisation in 2005 when they published a chemical assessment of tin and inorganic tin compounds [127]. More recently, Babayigit and coworkers found that degradation by-products of tin-based HaPSCs were more lethal to zebra fish than lead-based ones, which they attributed to a higher propensity for SnI_2 to decompose to HI, leading to acidification of the marine environment [128]. Some authors argue that producing non-toxic HaPSCs is a complex problem, and that fail-safe encapsulation of devices will be critical in initial commercialisation efforts [129]. This argument can be seen yet again when considering that attempts to create lead-free HaPSCs with efficiencies comparable to record devices has until now been unsuccessful [130, 131]. The propensity of Sn^{2+} to oxidise [45, 132, 133] also aggravates the already difficult problem of making stable HaPSCs.

Long-term stability

The inherent instability of HaPSCs under operating conditions remains a major obstacle to their widespread commercialisation [134–136]. Although an increasing number of devices are reported to take more than 1000 hours for cells to drop to 95% of their original power conversion efficiency [137–141], lifespans of HaPSCs remain short, especially when compared to conventional c-Si solar cells [142].

The instability of HaP-based devices is widely accepted to originate in the HaP layer itself [137, 143, 144]. For PV applications, the desired perovskite phases are either volatile or metastable at room temperature, meaning that they are in a constant process of degradation. The rate of degradation depends on a range of factors, including ion and cation diffusion coefficients, lattice strain, defect type and density, material composition, as well as environmental conditions. HaP films are especially sensitive to the latter, some of which can rapidly induce or catalyse degradation, and include the presence of moisture, oxygen, UV light, elevated temperatures [135–137, 143–145].

In this section, the primary degradation mechanisms occurring in the prototypical HaP, $MAPbI_3$ are reviewed and compared with analogous pro-

cesses in other HaP compositions. This decision was taken, in spite of the fact that the publications making up Chapter 2 are centred on mix-halide caesium-based HaPs, due to the extensive literature available on MAPbI$_3$. This means the well-established degradation mechanisms occurring in MAPbI$_3$ can be used to provide context to those occurring in caesium-based HaPs which have been less studied. It also highlights the superior intrinsic stability of bromine-heavy caesium-based HaPs which was important in their identification as subject of investigation in Chapter 2.
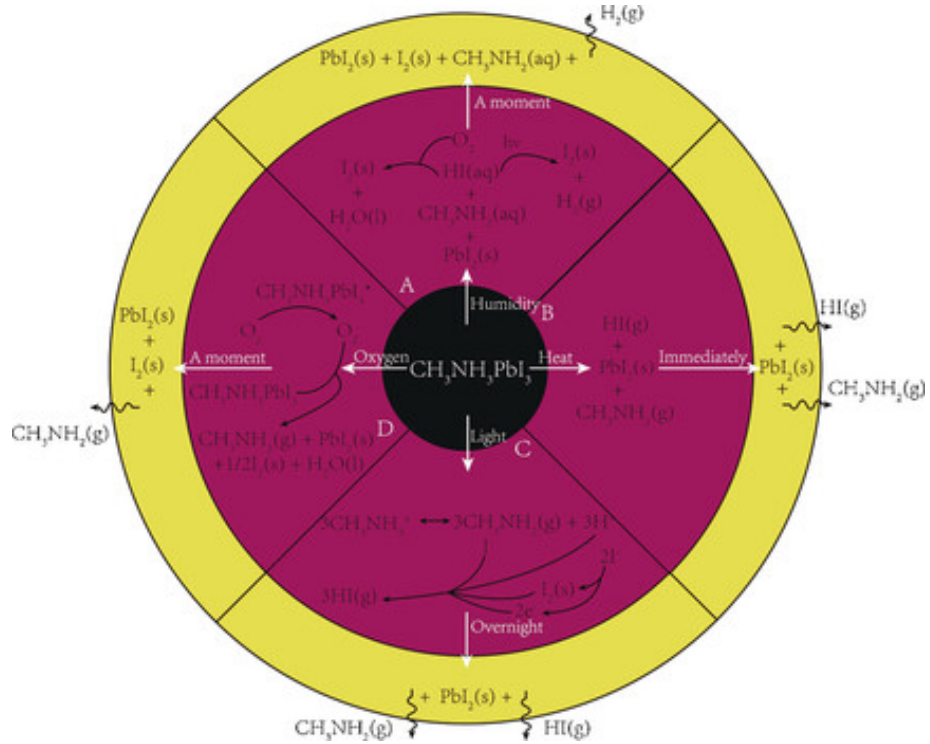
Figure 6: Degradation mechanisms that occur in methylamonium lead tri-iodide upon exposure to different external stimuli [134].

HaP films are known to become PbI$_2$ in the presence of humidity and this becomes increasingly problematic when considering the hydroscopic nature of the constituent cations [146]. Furthermore, PbI$_2$ can decompose leading to a loss of halides. MAPbI$_3$ is thought to degrade to its precursor components via the following chemical reactions [147]

$$CH_3NH_3PbI_3 \Leftrightarrow PbI_2(s) + CH_3NH_3I(aq) \qquad (1.2)$$

$$CH_3NH_3I(aq) \Leftrightarrow CH_3NH_2(aq) + HI(aq) \qquad (1.3)$$

$$4HI(aq) + O_2(g) \Leftrightarrow 2I_2(s) + 2H_2O \qquad (1.4)$$

$$2HI(aq) \Leftrightarrow H_2 + I_2 \qquad (1.5)$$
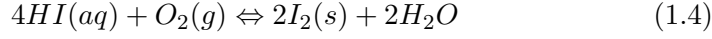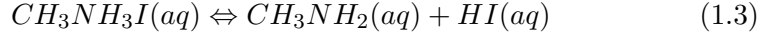
Leading to the production of hydrogen and iodine which can go on to initiate further degradation pathways [148, 149]. Alternatively, if the device is poorly encapsulated, these gases can escape making the process irreversible. Similar degradation products are thought to result from an alternative moisture-induced degradation pathway [150]. While similar degradation processes are thought to occur in MAPbBr$_3$ [151] and formamidinium-based perovskites [152], moisture induced-degradation appears to be reversible for inorganic caesium-based HaPs [153]. In fact, exposure to low levels of humidity can even improve the crystalline quality of CsPbBr$_3$ [154]. The improved moisture-tolerance provided by caesium may be related to water lowering the free-energy barrier to phase nucleation in these systems [155].

In the presence of oxygen, moisture can result in rapid degradation of organic-inorganic HaPs. Equation 1.4 shows how the reaction of HI with O$_2$ results in the release of water, triggering a chain reaction of further degradation. While this process cannot occur in caesium-based HaPs, since they do not dissociate into HI, there is both experimental [156, 157] and theoretical [158] evidence to suggest that HaPs may be unstable in dry environments when exposed to oxygen. To model this the following oxygen-induced degradation process has been proposed for MAPbI$_3$ [159]

$$CH_3NH_3PbI_3 + \frac{1}{4}O_2(g) \Leftrightarrow \frac{1}{2}H_2O + CH_3NH_2(aq) + PbI_2(s) + \frac{1}{2}I_2(s) \quad (1.6)$$
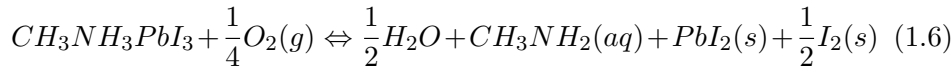
This leads to the release of water, methylamine, and the formation of PbI$_2$ and iodine. As in the case of moisture degradation, iodine may initiate further degradation [148, 149] and these volatile species may irreversibly escape if there are leakages in the device encapsulation. Simultaneously, PbI$_2$ may be able to further react with oxygen and form PbO [158]. The release of water also induces degradation via equation 1.2. These oxygen-induced degradation pathways also appear to be present in other HaPs, however at a slower rate [160]. That said, these reactions may only be kinetically favourable under illumination where phase degradation is thought to involve reactive intermediate superoxide species [160].

Photo-stability is understandably a key property for materials aiming to harness energy from the Sun. While HaP films tend to be relatively stable under illumination in the glove box, photo-induced degradation has been shown to be unavoidable under operating conditions [161]. Although there

have been numerous reports of HaPs degrading under illumination [162–164], the atomistic origin of this behaviour has not yet been fully understood. One possibility is that illumination results in an enhanced chemical potential of the halogen, resulting in a driving force for iodine flux towards the outer gas phase or to a sink [165]. Others have suggested that photo-induced degradation of HaPSC is mainly caused by the interface between the contacts and the transport layers [166]. There is also evidence that high-energy radiation can drive the dissociation of organic cations into mobile species which can diffuse out of the film [167].

Due to the volatile nature of some HaP components, elevated temperatures can also exacerbate film instability. While the volatility of iodine can be problematic for all HaPs, the intrinsic instability of MAPbI$_3$ is primarily related to volatility of the organic cation at operating temperatures [158]. On the other hand, as a consequence of both the low volatility of caesium and its inability to dissociate into other species, caesium-based perovskites show exceptional temperature stability [137, 168].

1.2.4 Outlook

Device lifespan, toxicity, and production methods are some of the most prominent factors on which HaPSC commercialisation depends. Recently, the latter has become less prominent due to steady progress and the development of new deposition methods [169–171]. That said, stability and toxicity remain key issues to be addressed. The development of high-quality fail-safe encapsulation appears to be one of the most promising solutions to date, since it simultaneously protects devices from ambient conditions [172] and contains possible leakages [173]. Aside from proper device encapsulation [174], the implementation of protective [175] and 2D perovskite capping layers [176] has also shown to be effective in combating against moisture-induced degradation. That said, there are some shortcomings with respect to relying on encapsulation only since it cannot offer protection against elevated temperatures, UV radiation or the thermodynamic instability of the HaP layers. To counter these, the intrinsic stability of HaPs must be improved.

A range of prominent experimental strategies have been developed for passivating harmful defects in HaP films, including antisolvent engineering, additive engineering, compositional engineering, and interface engineering, as well as the optimisation of the solvent type or the inclusion of co-solvents [177]. All these techniques fall under the umbrella term of "solvent engineering", which refers to the set of processing techniques that are used to improve HaP film quality during solution-based deposition [101]. Optimisation of these parameters is critical since they affect the deposition process, modify the drying of the film, and can impact crystallisation and nucleation processes.

In this section, three subjects are treated which are related to the publications that make up this thesis. Two of these, namely compositional and antisolvent engineering, were used to modulate the crystal growth of $CsPbIBr_2$ during a one-step spin coating process. The third section gives an overview of intrinsic defect states in HaPs which govern device stability and performance. This lays the groundwork for simulation-based investigations into these systems which are presented in Chapter 2.

Compositional Engineering

Compositional engineering has become one of the primary techniques for improving HaPSCs. This is due to the range of properties found in HaPs and the ease with which different compositions can be alloyed together, making it possible for traits to be selectively engineered [101]. In this section, possible candidates for each site in the ABX_3 HaP chemical formula are presented, as well as the traits which can be tuned.
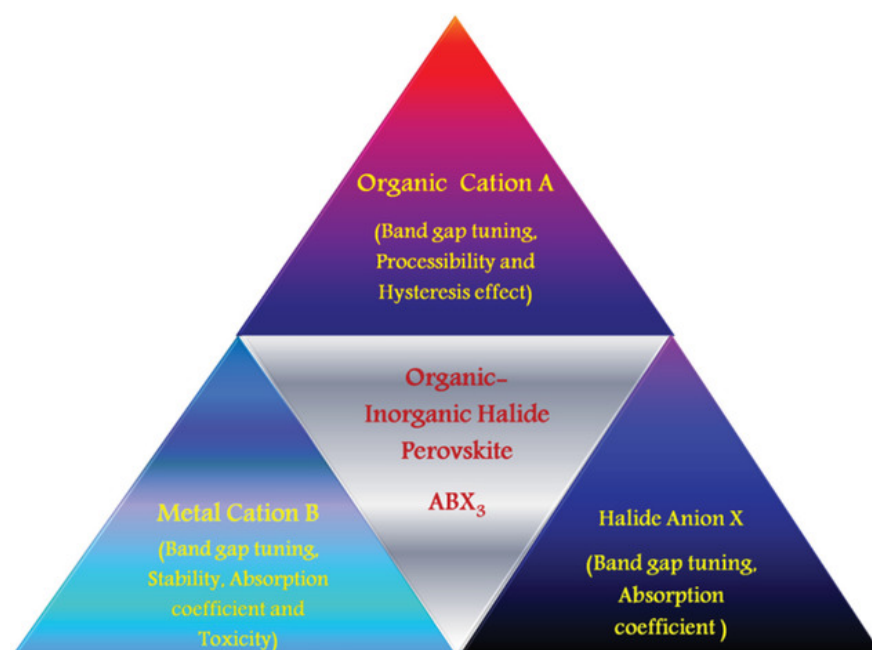

Figure 7: Properties that can be compositionally engineered into ABX_3 perovskites by site [178].

HaPs tend to have low-, room- and high-temperature phase transitions corresponding to an orthorhombic, tetragonal, cubic structure respectively

[179]. The cubic phase, which is usually desired for photovoltaic applications, is normally formed at elevated temperatures, meaning that many HaPs are metastable under operation conditions. One strategy to mitigate this metastability is to alloy HaPs, since phase transition temperatures are known to be a function of composition. For example, the phase transition temperature of cubic $CsPbI_3$ can be reduced from 310°C [180] to 130°C [181], when iodine is replaced by bromine.

In general, inclusion of smaller halides in the X-site results in increases in thermodynamic stability [158]. In fact, many bromide based compositions are stable at room temperature [154, 182]. While this does not appear to be the case for small additions of bromine, mixed halide compositions can suffer from light-induced phase segregation [183]. In general though, the increase in bandgap energy that occurs as iodine is replaced with smaller halides [155] makes it more attractive, in most cases, to substitute the cation sites instead. This is because the ideal bandgap, which maximises PCE, tends to be more easily reached using iodine-based compositions [184]. The exceptions to this are the HaPs used for top cells in tandem devices, in which bromine-heavy compositions are often used in order to reach higher bandgap values.

Compositionally engineering the B-site cation is currently an active area of research due to the toxicity of lead [124, 173]. Substituting lead for another cation has proven difficult though since it tends to lower both device performance and stability [173]. This may be due to the unusual defect chemistries in lead-based HaPs being difficult to replicate with other cations [185]. The main candidates for substituting lead in HaPs are bismuth [118–120], germanium [121], and tin [123–125]. That said, it should be noted that only the latter is able to form HaP structures which are suitable for photovoltaic applications by itself, whereas the former two can be used to make partial substitutions of lead. DFT calculations suggest that other lead-free alternatives have indirect bandgaps and therefore exhibit inferior optical absorption [122]. The exception to this are indium-based double-perovskite compositions which may have optoelectronic properties which are suitable for photovoltaic applications [122]. However, work has suggested that they may be difficult to realise experimentally due to oxidation-reduction related instabilities [186].

Of all the sites, the A-site cation tends to be the most flexible in terms of compositional engineering. However, it follows from equation 1.1 that only a subset of A-site cations can form cubic structures for a given X-site and B-site composition. For lead-iodide based systems the tolerance factor α predicts that the Cs^+ cation is too small, and the FA^+ cation too large, for the formation of a cubic structure. Although it is possible to form black cubic $CsPbI_3$ and $FAPbI_3$ phases at room temperature [112, 137], these structures are metastable and have a propensity to spontaneously degrade because of their low thermodynamic stability [152, 187]. This drove the discovery of multi-cation devices [188, 189] which are so prevalent now. Figure 8 shows

how the alloying of $FAPbI_3$ and $CsPbI_3$, which tend to arrange themselves in non-cubic structures at room temperature, can lead to the formation of a stable and cubic mix-cation composition [190]. The alloying of different cations also makes it possible to selectively engineer specific properties such as band structure, defect chemistry or optoelectronic behaviour.

Nowadays, high performance single-junction devices tend to be based on mixed-cation mixed-halide perovskites [113, 114], although impressive performances have also been obtained for pure $FAPbI_3$ [46, 112]. Important reductions in trap density have also been obtained by alloying $FAPbI_3$ with small quantities of Cs^+ [191] or MA^+ [192]. Compositional engineering of the A-site cation has also been suggested as a way of improving stability in the presence of oxygen.
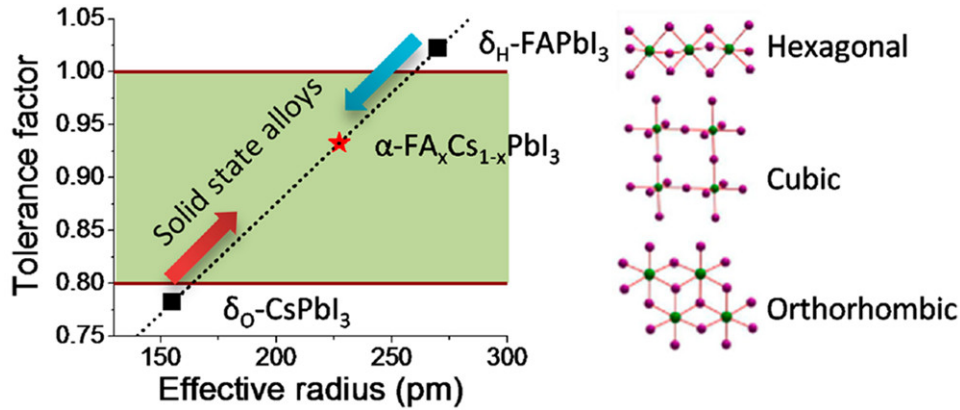

Figure 8: The tolerance factor α of $CsPbI_3$ and $FAPbI_3$ fall slightly outside the optimal values for the formation of a cubic perovskite structure, but by alloying them together it is possible to produce a cubic structure at room temperature with superior stability [190].

Wide-bandgap perovskites, based on $CsPbBr_3$, are some of the most stable HaP compositions and they are gaining attention for application as top cells in tandem devices. Unlike other HaPs, both the orthorhombic and tetragonal phases of $CsPbBr_3$ are suitable for photovoltaics, as well as the usual cubic structure [182]. This combined with the superior operational stability of $CsPbBr_3$ [168, 193], outlined in the previous section "Long-term stability", has led some to question the future of organic cations [194]. The main factor limiting $CsPbBr_3$-based HaPSCs is their rather poor performance which is a consequence of their large bandgaps [195]. Fortunately, this bandgap value can be reduced through substitution of either the A- or B-site cations, or through inclusion of iodine in the X-site. For this reason,

mixed-halide caesium-lead perovskites have been identified as particularly promising compositions for photovoltaic applications, and their improvement is the subject of two of the articles that make up this thesis.

Before the investigations that were carried out as part of this thesis, there were only a handful of reports focused on $CsPbIBr_2$ (in contrast with the thousands centred on $MAPbI_3$). This, combined with its attractive intrinsic stability, led to the improvement of this underdeveloped composition becoming a key objective of this doctoral thesis. The first article presented in Chapter 2 consists of compositionally engineering $CsPbIBr_2$ by substituting small amounts of caesium with rubidium. This was based on the fact that while rubidium has been shown to provide benefits to other HaP systems [189, 196, 197], equivalent investigations for $CsPbIBr_2$ were missing. On the other hand, the second article presented in Chapter 2 focuses on improving $CsPbIBr_2$ film quality by developing an antisolvent quenching technique.

Antisolvent engineering

When HaPSCs were first discovered, the deposition of uniform, compact and pinhole-free perovskite films was a challenge [198]. Antisolvent engineering quickly emerged as a successful technique for tackling these problems when Jeon and co-workers demonstrated the first anti-solvent quenching technique in 2014 [177]. Since then, antisolvent quenching has flourished as a technique for inducing rapid and dense nucleation in spin coated perovskite films [94], with numerous studies aiming to improve surface morphology and coverage, enlarge grains, provide highly crystalline films, or increase phase purity.

The antisolvent quenching method consists of dynamically spin coating an antisolvent on top of the already spinning precursor solution during the spin coating process. The spin coating procedure is discussed in the following "Methods" section where a schematic of the process can be found in Figure 11. The purpose of this antisolvent, which should be a nonsolvent to the chemical precursor, is to remove the precursor solvent and induce rapid HaP crystallisation [199]. This is achieved by an antisolvent-solvent interaction which creates locally supersaturated regions, resulting in crystal precipitation. In many cases, the gradient in concentration of the solvent-antisolvent mixture is enough to drive this process [94]. A schematic of the process can be seen in Figure 9.

Antisolvent quenching is notoriously difficult to carry out reproducibly due to the large number of variables which must be controlled, including ambient conditions, material sources and apparatus used. It is also usually done by hand, with many operators having their own technical interpretation of what the optimal height and angle the pipette should have when the antisolvent is ejected, as well as the force applied and the volume used. Furthermore, the antisolvent quenching process is made more challenging by

the small processing window (of a few seconds) for applying the antisolvent during the spin coating programme [94].
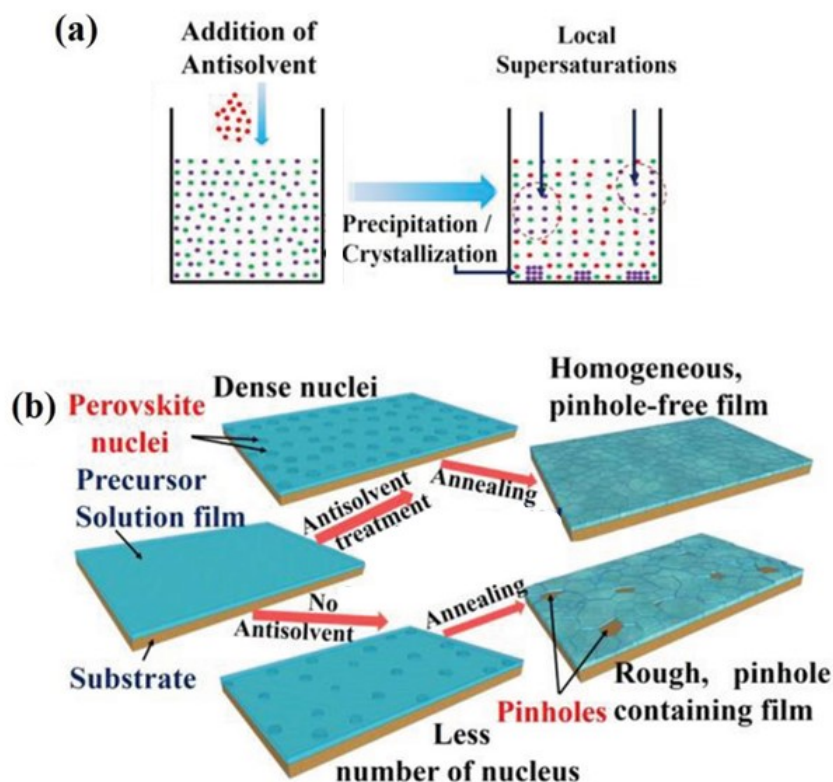

Figure 9: (a) Schematic representation of the antisolvent quenching method. Addition of the antisolvent to the precursor solution results in the creation of locally supersaturated regions leading to precipitation of the HaP. (b) Comparison of HaP film growth between films grown conventionally, without an antisolvent, and using the antisolvent quenching method [94].

Although antisolvent quenching is now one of the most widely used techniques for producing HaP films, most reports focus on establishing empirical links between deposition conditions and film properties. These findings have been succinctly summarised in several reviews [94, 200, 201]. Although antisolvent engineering continues to be carried out predominantly on the basis of trial and error, a few "rules of thumb" are now known and they can be helpful when developing an antisolvent quenching method.

Antisolvents can be categorised into three types depending on their miscibility with the precursor solvents and the solubility of the precursor components [202]. The easiest antisolvents to work with tend to be both miscible with the precursor solvent and unable to dissolve the perovskite precursors. If the antisolvent is not miscible with the host solvent, a large quantity should be applied slowly. Conversely, an antisolvent should be applied quickly if it can dissolve the organic precursors, in order to minimize damage to the film. These principles can be helpful when optimising the volume of, or speed with which, the antisolvent is applied, as well as during the initial phase of development when different antisolvents are "screened".

Defects

The nature of solution-processed HaP films results in rapid crystal growth at elevated temperatures, which can lead to the formation of a wide range of defects [203]. Structural defects play a central role in determining HaP performance and durability, since they can form initiation sites for degradation [148, 149, 204] and affect key processes such as charge transport and recombination [185, 205, 206]. Some defects also result in electronically active trap states [207–210] whose populations depend on how the HaP crystal is grown [185, 205]. Although passivation strategies can result in important reductions in harmful defect densities there is a fundamental limit, imposed by thermodynamics, on the minimum achievable defect densities in halide perovskites – and it is non-zero. For this reason, a complete understanding of defect chemistries and the role they play in determining device performance and stability is crucial.

Many defect types have now been identified in HaPs, some of which can act as p-type or n-type dopants [185, 192, 207, 211–214] leading to changes in the doping level of HaP films [45, 132, 133, 160, 209, 215–232]. The doping level in the HaP films is critical in determining HaPSC performance. Electronic doping influences the electric field inside devices which can affect key processes such as charge transportation and recombination. Moreover, non-radiative recombination mechanisms are a function of free electron and hole populations.

While the defect structure of MAPbI$_3$ has been widely studied, defect chemistries in other compositions appear to be more complicated and further investigations are needed. Early studies identified twelve intrinsic point defects in the MAPbI$_3$ crystal structures, shown in Figure 10 (a), including three types of vacancies (V_{MA}, V_{Pb} and V_I), three types of interstitials (MA_i, Pb_i and I_i) and six types of substitutions (MA_{Pb}, Pb_{MA}, MA_I, Pb_I, I_{MA} and I_{Pb}) [203]. More recent theoretical investigations have found similar defect structures in other HaP compositions [192, 211, 212]. Although DFT calculations suggest that Pb dimmers and I trimmers can give rise to deep transitional levels within the bandgap [206], defect formation en-

ergies suggest that the most abundant source of defects are shallow level traps [185, 233]. This is consistent with experimental results including the observed defect tolerance of HaPs [234] and the ability to electronically dope them by altering growth conditions [209, 215, 217, 232]. That said, while the dominant intrinsic dopants in organic-inorganic lead-iodide based systems depend on synthesis route [185, 192], bromine- and tin-based systems tend towards being more p-type due to the stability of p-type defects and self-doping mechanisms [211, 212].

Defects are often classified as either shallow or deep depending on whether the difference δE between the defect's ground state energy and the band edges is comparable to, or larger than, the thermal energy K_BT (K_B is the Boltzmann constant and T is temperature) under operating conditions [235]. For deep level states, $\delta E >> K_BT$, meaning that electrons or holes can be trapped resulting in a decrease in carrier extraction or transport efficiency [236]. On the other hand, work carried out as part of this thesis has shown that proper control over electronically active shallow defects (dopants) can result in important increases in device performance [237]. These results are presented in the third article that makes up Chapter 2.
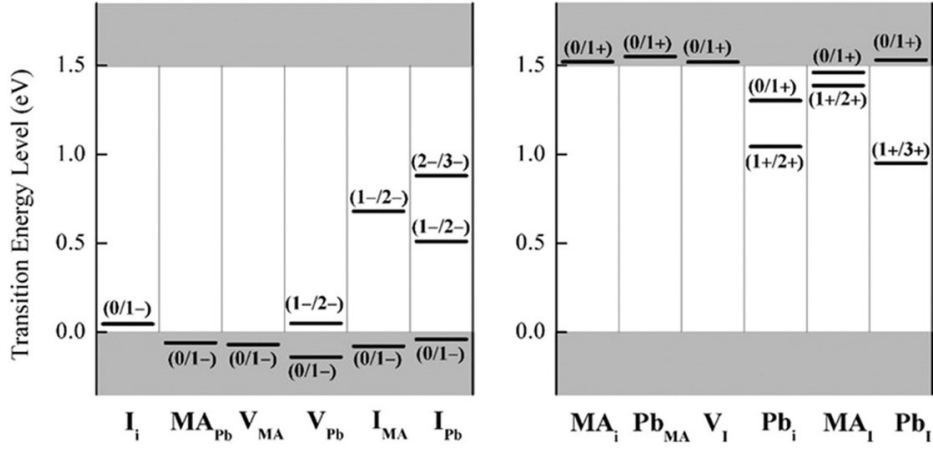
Figure 10: Intrinsic defect diagram of MAPbI$_3$ calculated using density functional theory (p-type defects are shown on the left, n-type dopants on the right) [203].

While initially p-type V_{Pb} and n-type MA_i were expected to be the dominant electronic dopants [185] in MAPbI$_3$, experimental and theoretical work has also highlighted the importance of p-type iodine defects [216, 238]. Recent studies have found that less abundant iodine defects can act as a source

of photochemically active deep electron and hole traps [239]. Activation energies for ionic migration also suggest vacancy-assisted migration of iodide ions may be central to the observed current-voltage hysteresis and low-frequency giant dielectric response in HaP systems [240]. Critically, these highly mobile ions can result from moisture- and oxygen-induced degradation (equations 1.5 and 1.6) where they can subsequently go on to initiate further degradation mechanisms [148, 149].

The decomposition of HaPs in the presence of moisture (equation 1.2) and oxygen (equation 1.6) can also lead to the creation of intrinsic structural defects. Volatile species can diffuse out of the films in the absence of proper encapsulation, leading to doping of the HaP film [218]. The creation of under-coordinated species, such as halides and Pb^{2+}, Pb clusters or antiside defects, such as PbI_3^-, can cause deep level traps [203].

While on one hand, the existence of electronically active shallow traps has been widely reported [45, 132, 133, 160, 209, 215–232], there have been relatively few investigations into the physics occurring in these systems [241, 242]. This is especially prudent when considering the fact that defect densities in polycrystalline HaP films tend to be several orders of magnitude higher than in single crystals [49, 60]. This is due to the large number of defects found at grain boundaries which play an important role in phase stability and optoelectronic performance [243]. As opposed to covalent bond-based semiconductors, such as c-Si, the ionic nature of HaPs enables unique passivation methods of charged defects to be carried out via coordinate or ionic bonding [203]. Work has shown that the successful implementation of passivation strategies can result in significant improvements in intrinsic stability [203, 236, 244] and changes in doping level [245]. These results highlight the importance of defects occurring in these systems and their associated chemistries, and why theoretical and experimental developments to control them will be central to large-scale deployment efforts.

1.3 Methods

In this section, the methods used in this thesis will be presented. These have been split into experimental techniques and computational simulations.

1.3.1 Experimental techniques

Several routine experimental techniques were used in this thesis and are briefly outlined here. Two of the three articles that make up this thesis were centred on the optimisation of thin film deposition processes. To evaluate the effectiveness of different treatments, several equipments were used to characterise film quality, including optical characterisation, x-ray diffraction (XRD) and scanning electron microscope (SEM).

Film synthesis

The HaP thin films produced as a part of this thesis were made using a spin coating method. A schematic of the spin coating process can be seen in Figure 11. Spin coating involves rotating a substrate and using the centrifugal forces to apply a thin and homogenous layer of precursor solution.
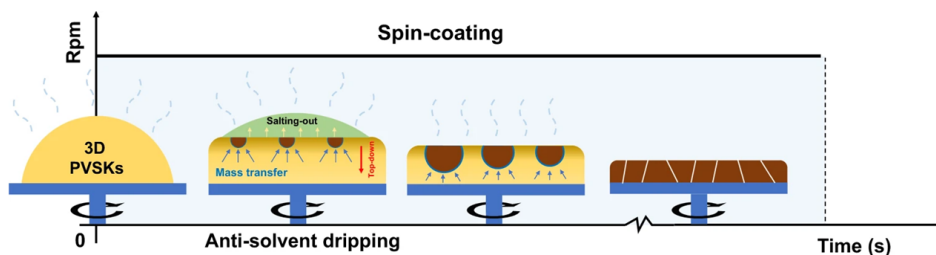

Figure 11: Schematic of the spin coating process [93].

A spin programme consists of at least one step carried out at a constant angular velocity, usually between 2000RPM and 4000RPM, with options for controlling the acceleration rate and the step duration. Solutions can be statically or dynamically spin coated, which describes whether the solution is either applied before or during the spinning of the substrate, respectively. In the one-step spin coating method, all the precursors are spun at once, whereas in the two-step method they are sequentially spun onto the substrate. The latter can be useful when it is desirable to use a set of solvents for different precursors.

Another common practice, an overview of which is presented in the previous section, is to carry out an antisolvent quenching step. This step, which involves dynamically applying a solvent to the spinning precursor solution, results in crystal precipitation, nucleation and growth. This can be used to produce highly compact and pin-hole free films [94]. HaP films prepared using spin coating are always annealed on a hotplate after thin film deposition has been carried out. This step removes any remaining solvent from the film and provides the optimal temperature for formation of the desired crystal structure.

In this doctoral thesis, HaP films were deposited using a static one-step spin coating method. Substrates were sequentially sonicated using ethanol, acetone, and isopropanol for 15 minutes before further treatment using the UV-ozone cleaner. Processed substrates were then transported into the glove box where all other steps were carried out, including precursor solution preparation, deposition, and film annealing.

Characterisation techniques

The SEM is a useful tool for characterising HaP films since it is non-destructive and can be used to quickly evaluate the morphology and topography of surface level crystal structures at high resolutions. This is achieved by focusing an electron beam on the target and using a range of detectors to measure electrons scattered from the sample caused by the beam-surface interaction.
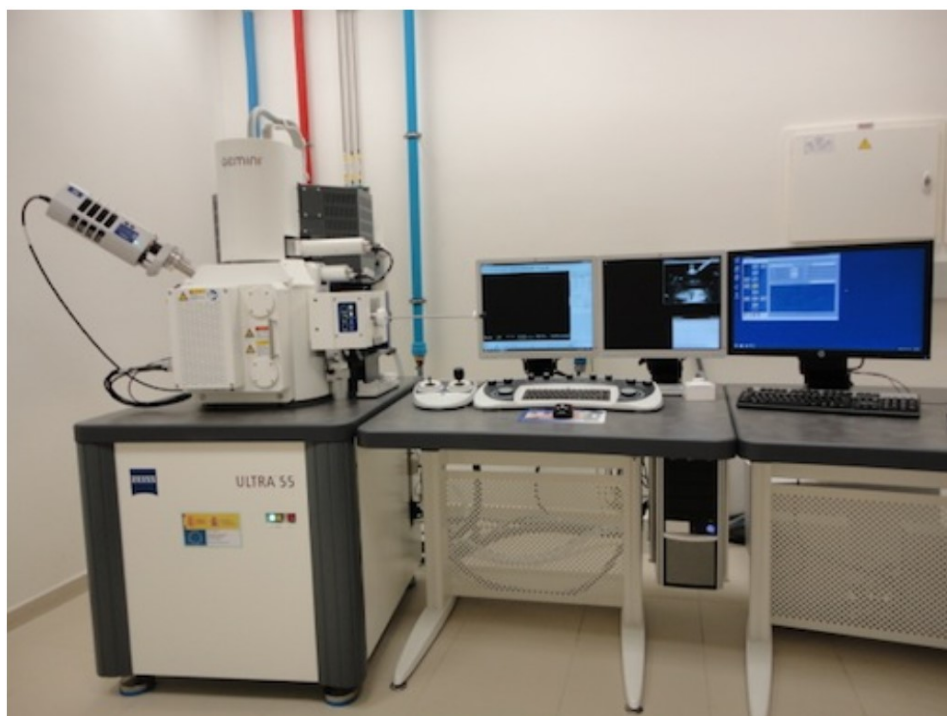
Figure 12: Photograph of the Zeiss Auriga Compact FESEM used as part of this doctoral thesis [246].

XRD has become a routine method for characterising the crystal structure of HaP films, with most HaP compositions having well-established diffraction patterns. Since the interplanar distance is also a function of crystalline phase, it can also be used to identify unconverted or degraded regions. Some degradation products, such as PbI_2, can be clearly seen using XRD. There are also a range of properties, such as crystallite size, chemical bonds and crystallographic disorder, that can be inferred from XRD patterns.

Optical characterisation of HaP films using methods such as absorbance or PL spectroscopy, can be a powerful tool for evaluating film quality and

inferring HaPSC performance. Moreover, these techniques tend to be non-destructive, quick to carry out and provide insights into key processes.

The absorption coefficient, which is related to the energy-band structure of a semiconducting material, is critical in determining its suitability for photovoltaics. The quantity of incident radiation absorbed by the HaP film is directly related to the number of photogenerated carriers present, and in turn the current density produced by solar devices. Assuming a defect-free semiconductor, the bandgap energy can be modelled from the absorption on-set using the Tauc Plot [247]. The absorption profile can also provide useful information about the density and energetic location of defects. Absorption below the bandgap is reflective of the static and dynamic disorder in the lattice, including dopants, deep trap states and carrier-phonon interactions. The energetic disorder can be modelled by fitting the exponential tail of the absorption coefficient with the Urbach Energy [248]. Below the exponential tail, external quantum efficiency measurements allow for the identification of deep trap states [249].
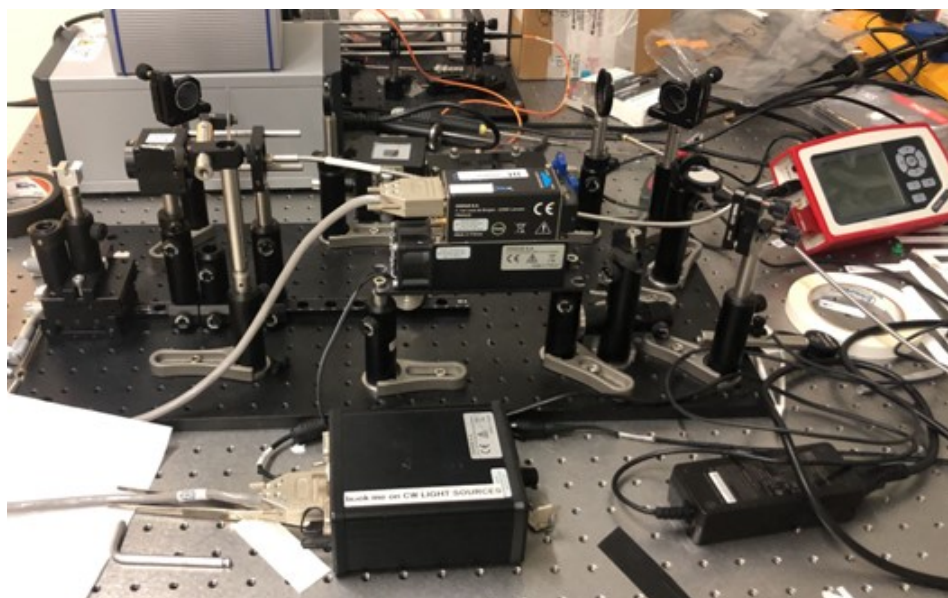
Figure 13: Photograph of the CW laser-driven PL set-up used as part of this doctoral thesis. The laser is guided to the sample holder via a series of mirrors. A high-pass filter and lens are placed perpendicular to the sample holder to capture the PL and guide it to the spectrometer using an optical fibre.

Spectrally resolved PL emission of HaP films can provide a range of useful information about their suitability for PV applications. As a first approximation, the PL emission maximum of a HaP film is a consequence of band-to-band recombination occurring at the band gap energy [250]. The

width of the emission is related to temperature effects, lattice strain and disorder, and Froehlich interactions [251, 252]. Given a calibrated set-up, the PL quantum efficiency can be calculated using a sample's PL flux density. This allows for an estimation of the quasi-Fermi level splitting and in turn the open circuit voltage of HaPSCs based on this film [253, 254]. This allows an estimation of device performance to be made, with a lower material and temporal investment than would be needed to make a real device.

1.3.2 Computational simulations

Computational simulations are a powerful tool for investigating the physics occurring in HaPSCs because they allow for precise control over a range of independent variables, some of which may be difficult or even impossible to precisely control experimentally. Simulations can also return data in a form that can be modelled and analysed using computational tools and automation techniques. This allows for a strong link to be established between a variety of dependent and independent variables. On the other hand, computer simulations often rely on simplified models of reality, which in turn are built upon current understandings of a field, meaning that in some cases they may fail to correctly reproduce experimental results or "overlook" behaviours that have not yet been fully understood.

There are several software options available for modelling the physics of solar cell devices including SETFOS [255], Advanced Semiconductor Analysis Software [256], SILVACO [257], IonMonger [258], and SCAPS [259, 260]. In this thesis, the latter was chosen for both its simplicity and reliability in reproducing experimental results [242, 261, 262], its low cost, and the ease with which simulations could be automated using external software. For the latter, MATLAB was used to automate the production of SCAPS scripts and execute them in the SCAPS environment. This led to improved productivity and throughput when studying the impact of varying material parameters. Depending on the content of the MATLAB-built SCAPS scripts, the format and content of the results returned by SCAPS could be controlled. These results were then processed and analysed using powerful in-built functions in MATLAB.

SCAPS (Solar Cell Capacitance Simulator) is a one-dimensional solar cell simulation developed by Burgelman and coworkers [259, 260]. SCAPS is designed to describe a one-dimensional structure of semiconducting layers which it achieves by solving the drift diffusion equations using the Newton-Raphson method. The drift diffusion equations are a set of five equations accounting for both electronic drift and diffusion phenomena. The application of boundary conditions to Poisson's equation and the Continuity and Constitutive relations results in a system of coupled differential equations that can, usually, be solved numerically by SCAPS. Defects and recombination centres can also be implemented in the bulk of the layers or at their

interfaces. As a result, both radiative and non-radiative recombination processes are considered.

This allows for an opto-electrical simulation of simplified one-dimensional devices to be made under a range of different bias voltages, temperatures, and illumination conditions. As a result, important solar cell performance indicators, such as a current voltage characteristics and band diagrams, can be simulated.

1.4 Thesis Motivation and Objectives

This thesis presents the results of investigations whose aim was to assist in the development of HaPSCs for their large-scale commercialisation and deployment. To achieve this, the following objectives were addressed:

- **Improve the stability of HaP films** – As mentioned previously, the instability of HaP films is the biggest barrier to their widespread commercialisation. In this thesis, a specific HaP composition was targeted, namely $CsPbIBr_2$. It was felt that the large bandgap of mixed halide inorganic perovskites makes them particularly useful for tandem solar cells, which are expected to be one of the most impactful perovskite-based technologies to first reach the market.

- **Improve HaPSC efficiency** – Although the bulk of research efforts are now focused on improving HaP stability, improvements in HaPSC PCE will also play an important role in determining the prospects for commercialisation. This is because the higher the efficiency of the device, the lower the levelized cost of electricity becomes, which is related to the cost per watt produced over a device's operational lifespan.

- **Investigate the fundamental physics and chemistry of HaPs** – A comprehensive understanding of the underlying mechanisms occurring in HaPs will be central to large-scale deployment. This is because it is likely to lead to novel applications, the development of new techniques for improving stability and performance, as well as the creation of tools and metrics for predicting their performance.

These objectives, which are rather broad in scope, were tackled by targetting specific gaps in the literature. The scientific questions targetted in this work, along with the strategies used to address them, are presented here:

1. **Investigate how compositional engineering can be used to improve $CsPbIBr_2$.** While rubidium has been shown to improve certain HaP systems, equivalent studies were lacking for $CsPbIBr_2$. In

this thesis, the effect of compositionally engineering $CsPbIBr_2$ with rubidium is systematically investigated.

2. **Improvement of the one-step spin coating method used to produce $CsPbIBr_2$.** Although antisolvent quenching has been key in producing many high quality HaP systems, before this thesis, $CsPbIBr_2$ was made almost exclusively without the use of an antisolvent. In this thesis, the one-step spin coating process for producing $CsPbIBr_2$ is improved by developing and implementing an antisolvent quenching step.

3. **Investigate the role of electronically active defects.** Defects are known to be critical in determining device stability and performance, however there are few studies investigating the relationship between processing conditions and the physics occurring in devices. In this thesis, the origin of optimal doping levels in HaP devices is investigated, resulting in guiding principles and experimental tools for the development of high-performance devices.

The research undertaken to accomplish these objectives has resulted in three publications in index journals. These publications make up the sections of Chapter 2 and are presented in the following order:

1. **Stewart, A. W.**, Bouich, A. & Marí, B. *"Inorganic perovskites improved film and crystal quality of $CsPbIBr_2$ when doped with rubidium"*. Journal of Materials Science: Materials in Electronics 1–9 (2021).

   These results were presented at as an oral presentation, titled *"Improving the Stability of $CsPbIBr_2$ through Solvent Engineering"*, at The 8th World Conference on Photovoltaic Energy Conversion (Milan, Italy. 26th to 20th September 2022).

2. **Stewart, A. W.**, Bouich, A. & Marí Soucase, B. *"Enhancing the stability and crystallinity of $CsPbIBr_2$ through antisolvent engineering"*. Journal of Materials Science (2021).

   These results were presented as an oral presentation, titled *"Antisolvent quenched $CsPbIBr_2$ for stable tandem devices"*, at the E-MRS Fall Meeting (Online. 20th to 23rd September 2021) and as a poster, titled *"Stable antisolvent quenched $CsPbIBr_2$ thin films"*, at the PV School 2022 (Les Houches, France. 3rd to 8th of April 2022).

3. **Stewart, A. W.** et al. *"Shedding light on electronically doped perovskites"*. Materials Today Chemistry 29, 101380 (2023).

   These results were presented as an oral presentation, titled *"Electronic doping in Halide Perovskite Solar Cells"*, at the Sustainable Metal-Halide Perovskites for Photovoltaics, Optoelectronics and Photonics

Conference (Valencia, Spain. 12th to 13th December 2022) and as a poster titled *"Electronic doping: Insights for highly efficient devices"* at the International Conference on Hybrid and Organic Photovoltaics (London, United Kingdom. 12th to 14th June 2023).

After these publications are presented in Chapter 2, a discussion of this research taking into consideration some developments in the field, subsequent to publication, are presented in Chater 3. Finally, Chapter 4 provides an overall summary as well as some indication of future work to be undertaken as a result of these investigations.

Bibliography

[1] Intergovernmental Panel on Climate Change, "Sixth assessment report: Fact sheet - biodiversity," 2022.

[2] Intergovernmental Panel on Climate Change, "Sixth assessment report: Fact sheet - food and water," 2022.

[3] Intergovernmental Panel on Climate Change, "Sixth assessment report: Fact sheet - health," 2023.

[4] J. Blunden, T. Boyer, and E. Bartow-Gillies, "State of the climate in 2022," *Bulletin of the American Meteorological Society*, vol. 104, 2023.

[5] H. Hersbach, B. Bell, P. Berrisford, G. Biavati, A. Horányi, J. M. Sabater, J. Nicolas, C. Peubey, R. Radu, I. Rozum, and D. Schepers, "Era5 hourly data on single levels from 1940 to present," 2023.

[6] European Parliament, "Greenhouse gas emissions by country and sector (infographic)," *Ref: 20180301STO98928*, 2023.

[7] International Energy Agency, "Net zero by 2050 - a roadmap for the global energy sector," 2021.

[8] C. Ballif, F. J. Haug, M. Boccard, P. J. Verlinden, and G. Hahn, "Status and perspectives of crystalline silicon photovoltaics in research and industry," *Nature Reviews Materials 2022 7:8*, vol. 7, pp. 597–616, 3 2022.

[9] H. Bahar, Y. Abdelilah, H. Bahar, F. Briens, P. Bojek, T. Criswell, T. Kurumi, T. Moorhouse, G. Rodríguez, and K. Veerakuma, "Special report on solar pv global supply chains," 2022.

[10] M. S. Chowdhury, K. S. Rahman, T. Chowdhury, N. Nuthammachot, K. Techato, M. Akhtaruzzaman, S. K. Tiong, K. Sopian, and N. Amin, "An overview of solar photovoltaic panels' end-of-life material recycling," *Energy Strategy Reviews*, vol. 27, p. 100431, 1 2020.

[11] S. W. Glunz, R. Preu, and D. Biro, "Crystalline silicon solar cells – state-of-the-art and future developments," 2012.

[12] T. Saga, "Advances in crystalline silicon solar cell technology for industrial mass production," *NPG Asia Materials 2010 2:3*, vol. 2, pp. 96–102, 7 2010.

[13] S. Weckend, A. Wade, and G. Heath, "End-of-life management: Solar photovoltaic panels," 2016.

[14] T. L. Curtis, H. Buchanan, G. Heath, L. Smith, and S. Shaw, "Solar photovoltaic module recycling: A survey of u.s. policies and initiatives," 2021.

[15] G. A. Heath, T. J. Silverman, M. Kempe, M. Deceglie, D. Ravikumar, T. Remo, H. Cui, P. Sinha, C. Libby, S. Shaw, K. Komoto, K. Wambach, E. Butler, T. Barnes, and A. Wade, "Research and development priorities for silicon photovoltaic module recycling to support a circular economy," *Nature Energy 2020 5:7*, vol. 5, pp. 502–510, 7 2020.

[16] K. K. Paul, J. H. Kim, and Y. H. Lee, "Hot carrier photovoltaics in van der waals heterostructures," *Nature Reviews Physics 2021 3:3*, vol. 3, pp. 178–192, 1 2021.

[17] S. Kahmann and M. A. Loi, "Hot carrier solar cells and the potential of perovskites for breaking the shockley–queisser limit," *Journal of Materials Chemistry C*, vol. 7, pp. 2471–2486, 2 2019.

[18] V. V. Rakitin and G. F. Novikov, "Third-generation solar cells based on quaternary copper compounds with the kesterite-type structure," *Russian Chemical Reviews*, vol. 86, pp. 99–112, 2 2017.

[19] G. F. Novikov and M. V. Gapanovich, "Third-generation cu-in-ga-(s, se)-based solar inverters," *Physics-Uspekhi*, vol. 60, pp. 161–178, 2 2017.

[20] S. Alhorani, S. Kumar, M. Genwa, and P. L. Meena, "Review of latest efficient sensitizer in dye-sensitized solar cells," *AIP Conference Proceedings*, vol. 2265, 11 2020.

[21] D. T. Gangadharan, Z. Xu, Y. Liu, R. Izquierdo, and D. Ma, "Recent advancements in plasmon-enhanced promising third-generation solar cells," *Nanophotonics*, vol. 6, pp. 153–175, 1 2017.

[22] A. J. Nozik, M. C. Beard, J. M. Luther, M. Law, R. J. Ellingson, and J. C. Johnson, "Semiconductor quantum dots and quantum dot arrays and applications of multiple exciton generation to third-generation photovoltaic solar cells," *Chemical Reviews*, vol. 110, pp. 6873–6890, 11 2010.

[23] M. A. Green, "Third generation photovoltaics: solar cells for 2020 and beyond," *Physica E: Low-dimensional Systems and Nanostructures*, vol. 14, pp. 65–70, 4 2002.

[24] J. Yan and B. R. Saunders, "Third-generation solar cells: a review and comparison of polymer:fullerene, hybrid polymer and perovskite solar cells," *RSC Advances*, vol. 4, pp. 43286–43314, 9 2014.

[25] X. Li, P. Li, Z. Wu, D. Luo, H. Y. Yu, and Z. H. Lu, "Review and perspective of materials for flexible solar cells," *Materials Reports: Energy*, vol. 1, p. 100001, 2 2021.

[26] National Renewable Energy Laboratory, "Best research-cell efficiency chart — photovoltaic research," 2023.

[27] H. J. Snaith, "Perovskites: The emergence of a new era for low-cost, high-efficiency solar cells," *Journal of Physical Chemistry Letters*, vol. 4, pp. 3623–3630, 11 2013.

[28] M. A. Green, "The passivated emitter and rear cell (perc): From conception to mass production," *Solar Energy Materials and Solar Cells*, vol. 143, pp. 190–197, 12 2015.

[29] J. M. Kadro, N. Pellet, F. Giordano, A. Ulianov, O. Müntener, J. Maier, M. Grätzel, and A. Hagfeldt, "Proof-of-concept for facile perovskite solar cell recycling," *Energy & Environmental Science*, vol. 9, pp. 3172–3179, 10 2016.

[30] E. A. Katz, "Perovskite: Name puzzle and german-russian odyssey of discovery," *Helvetica Chimica Acta*, vol. 103, p. e2000061, 6 2020.

[31] V. M. Goldschmidt, "Die gesetze der krystallochemie," *Die Naturwissenschaften*, vol. 14, pp. 477–485, 5 1926.

[32] H. D. Megaw, "Crystal structure of barium titanate," *Nature 1945 155:3938*, vol. 155, pp. 484–485, 1945.

[33] C. Li, X. Lu, W. Ding, L. Feng, Y. Gao, and Z. Guo, "Formability of abx 3 (x = f, cl, br, i) halide perovskites," *Acta Crystallographica Section B: Structural Science*, vol. 64, pp. 702–707, 2008.

[34] G. Kieslich, S. Sun, and A. K. Cheetham, "Solid-state principles applied to organic–inorganic perovskites: new tricks for an old dog," *Chemical Science*, vol. 5, pp. 4712–4715, 10 2014.

[35] A. M. Glazer, "The classification of tilted octahedra in perovskites," *Acta Crystallographica Section B Structural Crystallography and Crystal Chemistry*, vol. 28, pp. 3384–3392, 11 1972.

[36] H. Lin, C. Zhou, Y. Tian, T. Siegrist, and B. Ma, "Low-dimensional organometal halide perovskites," *ACS Energy Letters*, vol. 3, pp. 54–62, 1 2018.

[37] J. Hu, L. Yan, W. You, J. Hu, L. Yan, and W. You, "Two-dimensional organic–inorganic hybrid perovskites: A new platform for optoelectronic applications," *Advanced Materials*, vol. 30, p. 1802041, 11 2018.

[38] K. I. Kobayashi, T. Kimura, H. Sawada, K. Terakura, and Y. Tokura, "Room-temperature magnetoresistance in an oxide material with an ordered double-perovskite structure," *Nature 1998 395:6703*, vol. 395, pp. 677–680, 10 1998.

[39] H. Park, C. Ha, and J. H. Lee, "Advances in piezoelectric halide perovskites for energy harvesting applications," *Journal of Materials Chemistry A*, vol. 8, pp. 24353–24367, 12 2020.

[40] S. Ippili, V. Jella, J. H. Eom, J. Kim, S. Hong, J. S. Choi, V. D. Tran, N. V. Hieu, Y. J. Kim, H. J. Kim, and S. G. Yoon, "An eco-friendly flexible piezoelectric energy harvester that delivers high output performance is based on lead-free masni3 films and masni3-pvdf composite films," *Nano Energy*, vol. 57, pp. 911–923, 3 2019.

[41] E. J. Juarez-Perez, R. S. Sanchez, L. Badia, G. Garcia-Belmonte, Y. S. Kang, I. Mora-Sero, and J. Bisquert, "Photoinduced giant dielectric constant in lead halide perovskite solar cells," *Journal of Physical Chemistry Letters*, vol. 5, pp. 2390–2394, 7 2014.

[42] M. Manzi, G. Pica, M. D. Bastiani, S. Kundu, G. Grancini, and M. I. Saidaminov, "Ferroelectricity in hybrid perovskites," *Journal of Physical Chemistry Letters*, vol. 14, pp. 3535–3552, 4 2023.

[43] H. Lu, J. Wang, C. Xiao, X. Pan, X. Chen, R. Brunecky, J. J. Berry, K. Zhu, M. C. Beard, and Z. V. Vardeny, "Spin-dependent charge transport through 2d chiral hybrid lead-iodide perovskites," *Science Advances*, vol. 5, 12 2019.

[44] H. Xie, S. Hao, J. Bao, T. J. Slade, G. J. Snyder, C. Wolverton, and M. G. Kanatzidis, "All-inorganic halide perovskites as potential thermoelectric materials: Dynamic cation off-centering induces ultralow thermal conductivity," *Journal of the American Chemical Society*, vol. 142, pp. 9553–9563, 5 2020.

[45] M. A. Haque, J. Troughton, and D. Baran, "Processing-performance evolution of perovskite solar cells: From large grain polycrystalline films to single crystals," *Advanced Energy Materials*, vol. 10, p. 1902762, 4 2020.

[46] M. Kim, J. Jeong, H. Lu, T. K. Lee, F. T. Eickemeyer, Y. Liu, I. W. Choi, S. J. Choi, Y. Jo, H. B. Kim, S. I. Mo, Y. K. Kim, H. Lee, N. G. An, S. Cho, W. R. Tress, S. M. Zakeeruddin, A. Hagfeldt, J. Y. Kim, M. Grätzel, and D. S. Kim, "Conformal quantum dot-sno2 layers as electron transporters for efficient perovskite solar cells," *Science*, vol. 375, pp. 302–306, 2022.

[47] A. Miyata, A. Mitioglu, P. Plochocka, O. Portugall, J. T. W. Wang, S. D. Stranks, H. J. Snaith, and R. J. Nicholas, "Direct measurement of the exciton binding energy and effective masses for charge carriers in organic-inorganic tri-halide perovskites," *Nature Physics*, vol. 11, pp. 582–587, 2015.

[48] V. D'Innocenzo, G. Grancini, M. J. Alcocer, A. R. S. Kandada, S. D. Stranks, M. M. Lee, G. Lanzani, H. J. Snaith, and A. Petrozza, "Excitons versus free charges in organo-lead tri-halide perovskites," *Nature Communications*, vol. 5, 4 2014.

[49] A. Musiienko, D. R. Ceratti, J. Pipek, M. Brynza, H. Elhadidy, E. Belas, M. Betušiak, G. Delport, and P. Praus, "Defects in hybrid perovskites: The secret of efficient charge transport," *Advanced Functional Materials*, vol. 31, 2021.

[50] M. J. P. Alcocer, T. Leijtens, L. M. Herz, A. Petrozza, and H. J. Snaith, "Electron-hole diffusion lengths exceeding trihalide perovskite absorber," *Science*, vol. 342, pp. 341–344, 2013.

[51] G. Xing, N. Mathews, S. S. Lim, N. Yantara, X. Liu, D. Sabba, M. Grätzel, S. Mhaisalkar, and T. C. Sum, "Low-temperature solution-processed wavelength-tunable perovskites for lasing," *Nature Materials 2014 13:5*, vol. 13, pp. 476–480, 3 2014.

[52] L. M. Herz, "Charge-carrier mobilities in metal halide perovskites: Fundamental mechanisms and limits," *ACS Energy Letters*, vol. 2, pp. 1539–1548, 7 2017.

[53] M. J. Schilcher, P. J. Robinson, D. J. Abramovitch, L. Z. Tan, A. M. Rappe, D. R. Reichman, and D. A. Egger, "The significance of polarons and dynamic disorder in halide perovskites," *ACS Energy Letters*, vol. 18, p. 34, 2021.

[54] O. Almora, I. Zarazua, E. Mas-Marza, I. Mora-Sero, J. Bisquert, and G. Garcia-Belmonte, "Capacitive dark currents, hysteresis, and electrode polarization in lead halide perovskite solar cells," *Journal of Physical Chemistry Letters*, vol. 6, pp. 1645–1652, 5 2015.

[55] R. S. Sanchez, V. Gonzalez-Pedro, J. W. Lee, N. G. Park, Y. S. Kang, I. Mora-Sero, and J. Bisquert, "Slow dynamic processes in lead halide perovskite solar cells. characteristic times and hysteresis," *Journal of Physical Chemistry Letters*, vol. 5, pp. 2357–2363, 7 2014.

[56] H. J. Snaith, A. Abate, J. M. Ball, G. E. Eperon, T. Leijtens, N. K. Noel, S. D. Stranks, J. T. W. Wang, K. Wojciechowski, and W. Zhang, "Anomalous hysteresis in perovskite solar cells," *Journal of Physical Chemistry Letters*, vol. 5, pp. 1511–1515, 5 2014.

[57] E. L. Unger, E. T. Hoke, C. D. Bailie, W. H. Nguyen, A. R. Bowring, T. Heumüller, M. G. Christoforo, and M. D. McGehee, "Hysteresis and transient behavior in current–voltage measurements of hybrid-perovskite absorber solar cells," *Energy & Environmental Science*, vol. 7, pp. 3690–3698, 10 2014.

[58] K. Domanski, J. P. Correa-Baena, N. Mine, M. K. Nazeeruddin, A. Abate, M. Saliba, W. Tress, A. Hagfeldt, and M. Grätzel, "Not all that glitters is gold: Metal-migration-induced degradation in perovskite solar cells," *ACS Nano*, vol. 10, pp. 6306–6314, 6 2016.

[59] H. Yuan, E. Debroye, K. Janssen, H. Naiki, C. Steuwe, G. Lu, M. Moris, E. Orgiu, H. Uji-I, F. D. Schryver, P. Samorì, J. Hofkens, and M. Roeffaers, "Degradation of methylammonium lead iodide perovskite structures through light and electron beam driven ion migration," *Journal of Physical Chemistry Letters*, vol. 7, pp. 561–566, 2 2016.

[60] T. Zhang, C. Hu, and S. Yang, "Ion migration: A "double-edged sword" for halide-perovskite-based electronic devices," *Small Methods*, vol. 4, p. 1900552, 5 2020.

[61] C. Zhao, B. Chen, X. Qiao, L. Luan, K. Lu, B. Hu, C. Zhao, B. Chen, X. Qiao, L. Luan, K. Lu, and B. Hu, "Revealing underlying processes involved in light soaking effects and hysteresis phenomena in perovskite solar cells," *Advanced Energy Materials*, vol. 5, p. 1500279, 7 2015.

[62] A. Marronnier, H. Lee, B. Geffroy, J. Even, Y. Bonnassieux, and G. Roma, "Structural instabilities related to highly anharmonic phonons in halide perovskites," *Journal of Physical Chemistry Letters*, vol. 8, pp. 2659–2665, 6 2017.

[63] M. A. Carignano, S. A. Aravindh, I. S. Roqan, J. Even, C. Katan, C. K. Fluctua, M. A. Carignano, and S. Arabia, "Fluctuations and anharmonicity in lead iodide perovskites from molecular dynamics supercell simulationss critical fluctuations and anharmonicity in lead iodide perovskites from molecular dynamics supercell simulations," *Journal of Physical Chemistry C*, vol. 121, pp. 20729–20738, 2017.

[64] O. Yaffe, Y. Guo, L. Z. Tan, D. A. Egger, T. Hull, C. C. Stoumpos, F. Zheng, T. F. Heinz, L. Kronik, M. G. Kanatzidis, J. S. Owen, A. M. Rappe, M. A. Pimenta, and L. E. Brus, "Local polar fluctuations in lead halide perovskite crystals," *Physical Review Letters*, vol. 118, p. 136001, 3 2017.

[65] L. D. Whalley, J. M. Skelton, J. M. Frost, and A. Walsh, "Phonon anharmonicity, lifetimes, and thermal transport in ch3nh3pbi3 from many-body perturbation theory," *Physical Review B*, vol. 94, p. 220301, 12 2016.

[66] Y. Yamada and Y. Kanemitsu, "Electron-phonon interactions in halide perovskites," *NPG Asia Materials 2022 14:1*, vol. 14, pp. 1–15, 6 2022.

[67] C. Franchini, M. Reticcioli, M. Setvin, and U. Diebold, "Polarons in materials," *Nature Reviews Materials*, vol. 6, pp. 560–586, 7 2021.

[68] J. M. Frost, "Calculating polaron mobility in halide perovskites," *Physical Review B*, vol. 96, p. 195202, 11 2017.

[69] M. Li, J. Fu, Q. Xu, and T. C. Sum, "Slow hot-carrier cooling in halide perovskites: Prospects for hot-carrier solar cells," *Advanced Materials*, vol. 31, p. 1802486, 11 2019.

[70] D. R. Ceratti, Y. Rakita, L. Cremonesi, R. Tenne, V. Kalchenko, M. Elbaum, D. Oron, M. A. C. Potenza, G. Hodes, and D. Cahen, "Self-healing inside apbbr3 halide perovskite crystals," *Advanced Materials*, vol. 30, p. 1706273, 3 2018.

[71] D. R. Ceratti, A. V. Cohen, R. Tenne, Y. Rakita, L. Snarski, N. P. Jasti, L. Cremonesi, R. Cohen, M. Weitman, I. Rosenhek-Goldian, I. Kaplan-Ashiri, T. Bendikov, V. Kalchenko, M. Elbaum, M. A. Potenza, L. Kronik, G. Hodes, and D. Cahen, "The pursuit of stability in halide perovskites: The monovalent cation and the key for surface and bulk self-healing," *Materials Horizons*, vol. 8, pp. 1570–1586, 2021.

[72] D. R. Ceratti, R. Tenne, A. Bartezzaghi, L. Cremonesi, L. Segev, V. Kalchenko, D. Oron, M. A. C. Potenza, G. Hodes, and D. Cahen, "Self-healing and light-soaking in mapbi 3 : the effect of h 2 o," *Advanced Materials*, 6 2022.

[73] S. Aharon, D. R. Ceratti, N. P. Jasti, L. Cremonesi, Y. Feldman, M. A. C. Potenza, G. Hodes, and D. Cahen, "2d pb-halide perovskites can self-heal photodamage better than 3d ones," *Advanced Functional Materials*, vol. 32, 2022.

[74] F. Deschler, M. Price, S. Pathak, L. E. Klintberg, D. D. Jarausch, R. Higler, S. Hüttner, T. Leijtens, S. D. Stranks, H. J. Snaith, M. Atatüre, R. T. Phillips, and R. H. Friend, "High photoluminescence efficiency and optically pumped lasing in solution-processed mixed halide perovskite semiconductors," *Journal of Physical Chemistry Letters*, vol. 5, pp. 1421–1426, 4 2014.

[75] X. Zhu, S. Yang, Y. Cao, L. Duan, M. Du, J. Feng, Y. Jiao, X. Jiang, Y. Sun, H. Wang, S. Zuo, Y. Liu, S. . Frank, and . Liu, "Ionic-liquid-perovskite capping layer for stable 24.33%-efficient solar cell," *Advanced Energy Materials*, p. 2103491, 12 2021.

[76] T. Chiba, Y. Hayashi, H. Ebe, K. Hoshi, J. Sato, S. Sato, Y. J. Pu, S. Ohisa, and J. Kido, "Anion-exchange red perovskite quantum dots with ammonium iodine salts for highly efficient light-emitting devices," *Nature Photonics 2018 12:11*, vol. 12, pp. 681–687, 10 2018.

[77] C. Liu, Y. Yang, K. Rakstys, A. Mahata, M. Franckevicius, E. Mosconi, R. Skackauskaite, B. Ding, K. G. Brooks, O. J. Usiobo, J. N. Audinot, H. Kanda, S. Driukas, G. Kavaliauskaite, V. Gulbinas, M. Dessimoz, V. Getautis, F. D. Angelis, Y. Ding, S. Dai, P. J. Dyson, and M. K. Nazeeruddin, "Tuning structural isomers of phenylenedi-ammonium to afford efficient and stable perovskite solar cells and modules," *Nature Communications 2021 12:1*, vol. 12, pp. 1–9, 11 2021.

[78] Y. He, I. Hadar, and M. G. Kanatzidis, "Detecting ionizing radiation using halide perovskite semiconductors processed through solution and alternative methods," *Nature Photonics 2021 16:1*, vol. 16, pp. 14–26, 12 2021.

[79] S. Deumel, A. van Breemen, G. Gelinck, B. Peeters, J. Maas, R. Verbeek, S. Shanmugam, H. Akkerman, E. Meulenkamp, J. E. Huerdler, M. Acharya, M. García-Batlle, O. Almora, A. Guerrero, G. Garcia-Belmonte, W. Heiss, O. Schmidt, and S. F. Tedde, "High-sensitivity high-resolution x-ray imaging with soft-sintered metal halide perovskites," *Nature Electronics 2021 4:9*, vol. 4, pp. 681–688, 9 2021.

[80] X. Zhan, X. Zhang, Z. Liu, C. Chen, L. Kong, S. Jiang, S. Xi, G. Liao, and X. Liu, "Boosting the performance of self-powered cspbcl3-based uv photodetectors by a sequential vapor-deposition strategy and heterojunction engineering," *ACS Applied Materials and Interfaces*, vol. 13, pp. 45744–45757, 9 2021.

[81] R. A. John, N. Yantara, Y. F. Ng, G. Narasimman, E. Mosconi, D. Meggiolaro, M. R. Kulkarni, P. K. Gopalakrishnan, C. A. Nguyen, F. D. Angelis, S. G. Mhaisalkar, A. Basu, and N. Mathews, "Ionotronic halide perovskite drift-diffusive synapses for low-power neuromorphic computation," *Advanced Materials*, vol. 30, p. 1805454, 12 2018.

[82] J. Choi, J. S. Han, K. Hong, S. Y. Kim, H. W. Jang, J. Choi, J. S. Han, K. Hong, H. W. Jang, and S. Y. Kim, "Organic–inorganic hybrid halide perovskites for memories, transistors, and artificial synapses," *Advanced Materials*, vol. 30, p. 1704002, 10 2018.

[83] Y. Park, S. H. Kim, D. Lee, and J. S. Lee, "Designing zero-dimensional dimer-type all-inorganic perovskites for ultra-fast switching memory," *Nature Communications 2021 12:1*, vol. 12, pp. 1–8, 6 2021.

[84] A. Kojima, K. Teshima, Y. Shirai, and T. Miyasaka, "Organometal halide perovskites as visible-light sensitizers for photovoltaic cells," *Journal of the American Chemical Society*, vol. 131, pp. 6050–6051, 2009. First perovskite solar cell.

[85] J. H. Im, C. R. Lee, J. W. Lee, S. W. Park, and N. G. Park, "6.5perovskite quantum-dot-sensitized solar cell," *Nanoscale*, vol. 3, pp. 4088–4093, 10 2011.

[86] M. M. Lee, J. Teuscher, T. Miyasaka, T. N. Murakami, and H. J. Snaith, "Efficient hybrid solar cells based on meso-superstructured organometal halide perovskites," *Science (New York, N.Y.)*, vol. 338, pp. 643–647, 11 2012. Shows perovskite can act as an ETL.

[87] L. Etgar, P. Gao, Z. Xue, Q. Peng, A. K. Chandiran, B. Liu, M. K. Nazeeruddin, and M. Grätzel, "Mesoscopic ch3nh3pbi3/tio2 heterojunction solar cells," *Journal of the American Chemical Society*, vol. 134, pp. 17396–17399, 10 2012. Shows perovskite can act as a HTL.

[88] D. Liu and T. L. Kelly, "Perovskite solar cells with a planar heterojunction structure prepared using room-temperature solution processing techniques," *Nature Photonics 2013 8:2*, vol. 8, pp. 133–138, 12 2013.

[89] M. Liu, M. B. Johnston, and H. J. Snaith, "Efficient planar heterojunction perovskite solar cells by vapour deposition," *Nature 2013 501:7467*, vol. 501, pp. 395–398, 9 2013.

[90] M. Grätzel, "The light and shade of perovskite solar cells," *Nature Materials 2014 13:9*, vol. 13, pp. 838–842, 8 2014.

[91] L. Lin, T. W. Jones, T. C. J. Yang, N. W. Duffy, J. Li, L. Zhao, B. Chi, X. Wang, and G. J. Wilson, "Inorganic electron transport materials in perovskite solar cells," *Advanced Functional Materials*, vol. 31, 1 2021.

[92] P. K. Kung, M. H. Li, P. Y. Lin, Y. H. Chiang, C. R. Chan, T. F. Guo, and P. Chen, "A review of inorganic hole transport materials for perovskite solar cells," *Advanced Materials Interfaces*, vol. 5, p. 1800882, 11 2018.

[93] Y. Yan, Y. Yang, M. Liang, M. Abdellah, T. Pullerits, K. Zheng, and Z. Liang, "Implementing an intermittent spin-coating strategy to enable bottom-up crystallization in layered halide perovskites," *Nature communications*, 2021.

[94] S. Ghosh, S. Mishra, and T. Singh, "Antisolvents in perovskite solar cells: Importance, issues, and alternatives," *Advanced Materials Interfaces*, vol. 7, p. 2000950, 9 2020.

[95] P. Čulík, K. Brooks, C. Momblona, M. Adams, S. Kinge, F. Maréchal, P. J. Dyson, and M. K. Nazeeruddin, "Design and cost analysis of 100 mw perovskite solar panel manufacturing process in different locations," *ACS Energy Letters*, pp. 3039–3044, 2022.

[96] N. L. Chang, A. W. Y. Ho-Baillie, D. Vak, M. Gao, M. A. Green, and R. J. Egan, "Manufacturing cost and market potential analysis of demonstrated roll-to-roll perovskite photovoltaic cell processes," *Solar Energy Materials and Solar Cells*, vol. 174, pp. 314–324, 1 2018.

[97] P. Wang, X. Zhang, Y. Zhou, Q. Jiang, Q. Ye, Z. Chu, X. Li, X. Yang, Z. Yin, and J. You, "Solvent-controlled growth of inorganic perovskite films in dry environment for efficient and stable solar cells," *Nature Communications*, vol. 9, 12 2018.

[98] F. Wang, Y. Cao, C. Chen, Q. Chen, X. Wu, X. Li, T. Qin, and W. Huang, "Materials toward the upscaling of perovskite solar cells: Progress, challenges, and strategies," *Advanced Functional Materials*, vol. 28, 12 2018.

[99] S.-W. Lee, S. Bae, D. Kim, H.-S. Lee, S. w Lee, D. Kim, S. Bae, and H. s Lee, "Historical analysis of high-efficiency, large-area solar cells: Toward upscaling of perovskite solar cells," *Advanced Materials*, vol. 32, p. 2002202, 12 2020.

[100] M. Jeong, I. W. Choi, K. Yim, S. Jeong, M. Kim, S. J. Choi, Y. Cho, J. H. An, H. B. Kim, Y. Jo, S. H. Kang, J. H. Bae, C. W. Lee, D. S. Kim, and C. Yang, "Large-area perovskite solar cells employing spiro-naph hole transport material," *Nature Photonics 2022 16:2*, vol. 16, pp. 119–125, 1 2022.

[101] S. L. Hamukwaya, H. Hao, Z. Zhao, J. Dong, T. Zhong, J. Xing, L. Hao, and M. M. Mashingaidze, "A review of recent developments in preparation methods for large-area perovskite solar cells," *Coatings 2022, Vol. 12, Page 252*, vol. 12, p. 252, 2 2022.

[102] C. F. J. Lau, X. Deng, Q. Ma, J. Zheng, J. S. Yun, M. A. Green, S. Huang, and A. W. Ho-Baillie, "Cspbibr2 perovskite solar cell by

spray-assisted deposition," *ACS Energy Letters*, vol. 1, pp. 573–577, 9 2016.

[103] Z. Yang, C. C. Chueh, F. Zuo, J. H. Kim, P. W. Liang, and A. K. Jen, "High-performance fully printable perovskite solar cells via blade-coating technique under the ambient condition," *Advanced Energy Materials*, vol. 5, 7 2015.

[104] B. Gao and J. Meng, "Flexible ch3nh3pbi3 perovskite solar cells with high stability based on all inkjet printing," *Solar Energy*, vol. 230, pp. 598–604, 12 2021.

[105] X. Li, D. Bi, C. Yi, J. D. Décoppet, J. Luo, S. M. Zakeeruddin, A. Hagfeldt, and M. Grätzel, "A vacuum flash-assisted solution process for high-efficiency large-area perovskite solar cells," *Science*, vol. 353, pp. 58–62, 2016.

[106] M. M. Tavakoli, L. Gu, Y. Gao, and C. Reckmeier, "Fabrication of efficient planar perovskite solar cells using a one-step chemical vapor deposition method," *Scientific Reports*, vol. 5, 2015.

[107] J. Li, H. Wang, X. Y. Chin, H. A. Dewi, K. Vergeer, T. W. Goh, J. W. M. Lim, J. H. Lew, K. P. Loh, C. Soci, T. C. Sum, H. J. Bolink, N. Mathews, S. Mhaisalkar, and A. Bruno, "Highly efficient thermally co-evaporated perovskite solar cells and mini-modules," *Joule*, vol. 4, pp. 1035–1053, 5 2020.

[108] X. Liu, J. Li, Z. Liu, X. Tan, B. Sun, S. Xi, T. Shi, Z. Tang, and G. Liao, "Vapor-assisted deposition of cspbibr2 films for highly efficient and stable carbon-based planar perovskite solar cells with superior voc," *Electrochimica Acta*, vol. 330, p. 135266, 2020.

[109] K. Hwang, Y. S. Jung, Y. J. Heo, F. H. Scholes, S. E. Watkins, J. Subbiah, D. J. Jones, D. Y. Kim, and D. Vak, "Toward large scale roll-to-roll production of fully printed perovskite solar cells," *Advanced Materials*, vol. 27, pp. 1241–1247, 2 2015.

[110] B. Dou, J. B. Whitaker, K. Bruening, D. T. Moore, L. M. Wheeler, J. Ryter, N. J. Breslin, J. J. Berry, S. M. Garner, F. S. Barnes, S. E. Shaheen, C. J. Tassone, K. Zhu, and M. F. V. Hest, "Roll-to-roll printing of perovskite solar cells," *ACS Energy Letters*, vol. 3, pp. 2558–2565, 10 2018.

[111] C. Zuo, D. Vak, D. Angmo, L. Ding, and M. Gao, "One-step roll-to-roll air processed high efficiency perovskite solar cells," *Nano Energy*, vol. 46, pp. 185–192, 4 2018.

[112] J. Jeong, M. Kim, J. Seo, H. Lu, P. Ahlawat, A. Mishra, Y. Yang, M. A. Hope, F. T. Eickemeyer, M. Kim, Y. J. Yoon, I. W. Choi, B. P. Darwich, S. J. Choi, Y. Jo, J. H. Lee, B. Walker, S. M. Zakeeruddin, L. Emsley, U. Rothlisberger, A. Hagfeldt, D. S. Kim, M. Grätzel, and J. Y. Kim, "Pseudo-halide anion engineering for α-fapbi3 perovskite solar cells," *Nature*, vol. 592, pp. 381–385, 2021.

[113] J. J. Yoo, G. Seo, M. R. Chua, T. G. Park, Y. Lu, F. Rotermund, Y. K. Kim, C. S. Moon, N. J. Jeon, J. P. Correa-Baena, V. Bulović, S. S. Shin, M. G. Bawendi, and J. Seo, "Efficient perovskite solar cells via improved carrier management," *Nature*, vol. 590, pp. 587–593, 2021.

[114] G. Kim, H. Min, K. S. Lee, D. Y. Lee, S. M. Yoon, and S. I. Seok, "Impact of strain relaxation on performance of a-formamidinium lead iodide perovskite solar cells," *Science*, vol. 370, pp. 108–112, 10 2020.

[115] A. L. Wani, A. Ara, and J. A. Usmani, "Lead toxicity: A review," 6 2015.

[116] World Health Organization, *Exposure to lead: a major public health concern, 2nd edition.* 2021.

[117] L. Fewtrell, R. Kaufmann, A. Prüss-Üstün, D. Campbell-Lendrum, C. Corvalán, and A. Woodward, "Lead assessing the environmental burden of disease at national and local levels," 2003.

[118] B.-W. Park, B. Philippe, X. Zhang, H. Rensmo, G. Boschloo, E. M. J. Johansson, B.-W. Park, X. Zhang, G. Boschloo, E. M. J. Johansson, B. Philippe, and H. Rensmo, "Bismuth based hybrid perovskites a3bi2i9 (a: Methylammonium or cesium) for solar cell application," *Advanced Materials*, vol. 27, pp. 6806–6813, 11 2015.

[119] M. Lyu, J. H. Yun, M. Cai, Y. Jiao, P. V. Bernhardt, M. Zhang, Q. Wang, A. Du, H. Wang, G. Liu, and L. Wang, "Organic–inorganic bismuth (iii)-based material: A lead-free, air-stable and solution-processable light-absorber beyond organolead perovskites," *Nano Research*, vol. 9, pp. 692–702, 3 2016.

[120] R. L. Z. Hoye, R. E. Brandt, A. Osherov, . Vladan, S. Stevanovic´, S. S. Tranks, M. W. B. Wilson, H. Kim, A. J. Akey, J. D. Perkins, R. K. Urchin, J. R. Poindexter, E. N. Wang, M. G. Bawendi, B. Vladimir Bulovic´, and T. N. Buonassisi, "Methylammonium bismuth iodide as a lead-free, stable hybrid organic–inorganic solar absorber," *Chemistry – A European Journal*, vol. 22, pp. 2605–2610, 2 2016.

[121] W. Ming, H. Shi, and M. H. Du, "Large dielectric constant, high acceptor density, and deep electron traps in perovskite solar cell material csgei3," *Journal of Materials Chemistry A*, vol. 4, pp. 13852–13858, 2016.

[122] W. Meng, X. Wang, Z. Xiao, J. Wang, D. B. Mitzi, and Y. Yan, "Parity-forbidden transitions and their impact on the optical absorption properties of lead-free metal halide perovskites and double perovskites," *Journal of Physical Chemistry Letters*, vol. 6, pp. 2999–3007, 2017.

[123] N. K. Noel, S. D. Stranks, A. Abate, C. Wehrenfennig, S. Guarnera, A. A. Haghighirad, A. Sadhanala, G. E. Eperon, S. K. Pathak, M. B. Johnston, A. Petrozza, L. M. Herz, and H. J. Snaith, "Lead-free organic-inorganic tin halide perovskites for photovoltaic applications," *Energy and Environmental Science*, vol. 7, pp. 3061–3068, 2014.

[124] M. Pitaro, E. K. Tekelenburg, S. Shao, and M. A. Loi, "Tin halide perovskites: From fundamental properties to solar cells," *Advanced Materials*, vol. 34, p. 2105844, 1 2022.

[125] C. C. Stoumpos, C. D. Malliakas, and M. G. Kanatzidis, "Semiconducting tin and lead iodide perovskites with organic cations: Phase transitions, high mobilities, and near-infrared photoluminescent properties," *Inorganic Chemistry*, vol. 52, pp. 9019–9038, 2013.

[126] R. A. Hiles, "Absorption, distribution and excretion of inorganic tin in rats," *Toxicology and Applied Pharmacology*, vol. 27, pp. 366–379, 2 1974.

[127] P. Howe, P. Watts, U. N. E. Programme., I. L. Organisation., W. H. Organization., I.-O. P. for the Sound Management of Chemicals., and I. P. on Chemical Safety., "Tin and inorganic tin compounds," p. 73, 2005.

[128] A. Babayigit, D. D. Thanh, A. Ethirajan, J. Manca, M. Muller, H. G. Boyen, and B. Conings, "Assessing the toxicity of pb- and sn-based perovskite solar cells in model organism danio rerio," *Scientific Reports 2016 6:1*, vol. 6, pp. 1–11, 1 2016.

[129] A. Babayigit, A. Ethirajan, M. Muller, and B. Conings, "Toxicity of organometal halide perovskite solar cells," *Nature Materials 2016 15:3*, vol. 15, pp. 247–251, 2 2016.

[130] F. Hao, C. C. Stoumpos, D. H. Cao, R. P. Chang, and M. G. Kanatzidis, "Lead-free solid-state organic–inorganic halide perovskite solar cells," *Nature Photonics 2014 8:6*, vol. 8, pp. 489–494, 5 2014.

[131] W. Liao, D. Zhao, Y. Yu, C. R. Grice, C. Wang, A. J. Cimaroli, P. Schulz, W. Meng, K. Zhu, R.-G. Xiong, Y. Yan, W. Liao, D. Zhao, Y. Yu, C. R. Grice, C. Wang, A. J. Cimaroli, W. Meng, Y. Yan, R. g Xiong, P. Schulz, and K. Zhu, "Lead-free inverted planar formamidinium tin triiodide perovskite solar cells achieving power conversion efficiencies up to 6.22%," *Advanced Materials*, vol. 28, pp. 9333–9340, 11 2016.

[132] Y. Takahashi, H. Hasegawa, Y. Takahashi, and T. Inabe, "Hall mobility in tin iodide perovskite ch3nh3sni 3: Evidence for a doped semiconductor," *Journal of Solid State Chemistry*, vol. 205, pp. 39–43, 2013.

[133] T. Liu, X. Zhao, J. Li, Z. Liu, F. Liscio, S. Milita, B. C. Schroeder, and O. Fenwick, "Enhanced control of self-doping in halide perovskites for improved thermoelectric performance," *Nature Communications*, vol. 10, pp. 1–9, 2019.

[134] D. Wang, M. Wright, N. K. Elumalai, and A. Uddin, "Stability of perovskite solar cells," *Solar Energy Materials and Solar Cells*, vol. 147, pp. 255–275, 2016.

[135] H. Zhang, K. Darabi, N. Y. Nia, A. Krishna, P. Ahlawat, B. Guo, M. H. S. Almalki, T. S. Su, D. Ren, V. Bolnykh, L. A. Castriotta, M. Zendehdel, L. Pan, S. S. Alonso, R. Li, S. M. Zakeeruddin, A. Hagfeldt, U. Rothlisberger, A. D. Carlo, A. Amassian, and M. Grätzel, "A universal co-solvent dilution strategy enables facile and cost-effective fabrication of perovskite photovoltaics," *Nature Communications*, vol. 13, pp. 1–12, 1 2022.

[136] S. Mazumdar, Y. Zhao, and X. Zhang, "Stability of perovskite solar cells: Degradation mechanisms and remedies," *Frontiers in Electronics*, vol. 0, p. 8, 8 2021.

[137] Y. Wang, M. I. Dar, L. K. Ono, T. Zhang, M. Kan, Y. Li, L. Zhang, X. Wang, Y. Yang, X. Gao, Y. Qi, M. Grätzel, and Y. Zhao, "Thermodynamically stabilized b-cspbi3–based perovskite solar cells with efficiencies >18%," *Science*, vol. 365, pp. 591–595, 8 2019.

[138] X. Zheng, Y. Hou, C. Bao, J. Yin, F. Yuan, Z. Huang, K. Song, J. Liu, J. Troughton, N. Gasparini, C. Zhou, Y. Lin, D. J. Xue, B. Chen, A. K. Johnston, N. Wei, M. N. Hedhili, M. Wei, A. Y. Alsalloum, P. Maity, B. Turedi, C. Yang, D. Baran, T. D. Anthopoulos, Y. Han, Z. H. Lu, O. F. Mohammed, F. Gao, E. H. Sargent, and O. M. Bakr, "Managing grains and interfaces via ligand anchoring enables 22.3%-efficiency inverted perovskite solar cells," *Nature Energy*, vol. 5, pp. 131–140, 1 2020.

[139] Y. H. Lin, N. Sakai, P. Da, J. Wu, H. C. Sansom, A. J. Ramadan, S. Mahesh, J. Liu, R. D. Oliver, J. Lim, L. Aspitarte, K. Sharma, P. K. Madhu, A. B. Morales-Vilches, P. K. Nayak, S. Bai, F. Gao, C. R. Grovenor, M. B. Johnston, J. G. Labram, J. R. Durrant, J. M. Ball, B. Wenger, B. Stannowski, and H. J. Snaith, "A piperidinium salt stabilizes efficient metal-halide perovskite solar cells," *Science*, vol. 369, pp. 96–102, 7 2020.

[140] S. Bai, P. Da, C. Li, Z. Wang, Z. Yuan, F. Fu, M. Kawecki, X. Liu, N. Sakai, J. T. W. Wang, S. Huettner, S. Buecheler, M. Fahlman, F. Gao, and H. J. Snaith, "Planar perovskite solar cells with long-term stability using ionic liquid additives," *Nature*, vol. 571, pp. 245–250, 7 2019.

[141] J. A. Christians, P. Schulz, J. S. Tinkham, T. H. Schloemer, S. P. Harvey, B. J. T. D. Villers, A. Sellinger, J. J. Berry, and J. M. Luther, "Tailored interfaces of unencapsulated perovskite solar cells for ¿1,000 hour operational stability," *Nature Energy*, vol. 3, pp. 68–74, 2018.

[142] D. C. Jordan and S. R. Kurtz, "Photovoltaic degradation rates-an analytical review," *Progress in Photovoltaics: Research and Applications*, vol. 21, pp. 12–29, 1 2013.

[143] B. Li and W. Zhang, "Improving the stability of inverted perovskite solar cells towards commercialization," *Communications Materials 2022 3:1*, vol. 3, pp. 1–13, 9 2022.

[144] M. I. Asghar, J. Zhang, H. Wang, and P. D. Lund, "Device stability of perovskite solar cells – a review," *Renewable and Sustainable Energy Reviews*, vol. 77, pp. 131–146, 9 2017.

[145] N. H. Tiep, Z. Ku, and H. J. Fan, "Recent advances in improving the stability of perovskite solar cells," *Advanced Energy Materials*, vol. 6, 2 2016.

[146] H. Wang, J. Sun, Y. Gu, C. Xu, Y. Lu, J. Hu, T. Chen, C. Zhu, and P. Luo, "Solvent-engineering-processed cspbibr2 inorganic perovskite solar cells with efficiency of 11%," *Solar Energy Materials and Solar Cells*, vol. 238, p. 111640, 5 2022.

[147] R. Wang, M. Mujahid, Y. Duan, Z. K. Wang, J. Xue, and Y. Yang, "A review of perovskites solar cell stability," *Advanced Functional Materials*, vol. 29, p. 1808843, 11 2019.

[148] F. Fu, S. Pisoni, Q. Jeangros, J. Sastre-Pellicer, M. Kawecki, A. Paracchino, T. Moser, J. Werner, C. Andres, L. Duchêne, P. Fiala, M. Rawlence, S. Nicolay, C. Ballif, A. N. Tiwari, and S. Buecheler, "I2

vapor-induced degradation of formamidinium lead iodide based perovskite solar cells under heat-light soaking conditions," *Energy and Environmental Science*, vol. 12, pp. 3074–3088, 10 2019.

[149] S. Wang, Y. Jiang, E. J. Juarez-Perez, L. K. Ono, and Y. Qi, "Accelerated degradation of methylammonium lead iodide perovskites induced by exposure to iodine vapour," *Nature Energy*, vol. 2, p. 16195, 2016.

[150] J. M. Frost, K. T. Butler, F. Brivio, C. H. Hendon, M. V. Schilfgaarde, and A. Walsh, "Atomistic origins of high-performance in hybrid halide perovskite solar cells," *Nano Letters*, vol. 14, pp. 2584–2590, 5 2014.

[151] J. I. J. Choi, M. E. Khan, Z. Hawash, K. J. Kim, H. Lee, L. K. Ono, Y. Qi, Y. H. Kim, and J. Y. Park, "Atomic-scale view of stability and degradation of single-crystal mapbbr 3 surfaces," *Journal of Materials Chemistry A*, vol. 7, pp. 20760–20766, 9 2019.

[152] X. Zhou, L. Zhang, H. Hu, Z. Jiang, D. Wang, J. Chen, Y. Li, J. Wu, Y. Zhang, M. Zhang, C. Liu, Y. Peng, X. Wang, and B. Xu, "Highly efficient and stable hole-transport-layer-free inverted perovskite solar cells achieved 22% efficiency through p-type molecular synergistic doping," *Nano Energy*, vol. 104, 12 2022.

[153] J. Lin, M. Lai, L. Dou, C. S. Kley, H. Chen, F. Peng, J. Sun, D. Lu, S. A. Hawks, C. Xie, F. Cui, A. P. Alivisatos, D. T. Limmer, and P. Yang, "Thermochromic halide perovskite solar cells," *Nature Materials*, vol. 17, pp. 261–267, 1 2018.

[154] D. D. Girolamo, M. I. Dar, D. Dini, L. Gontrani, R. Caminiti, A. Mattoni, M. Graetzel, and S. Meloni, "Dual effect of humidity on cesium lead bromide: enhancement and degradation of perovskite films," *Journal of Materials Chemistry A*, vol. 7, pp. 12292–12302, 5 2019.

[155] S. Dastidar, D. A. Egger, L. Z. Tan, S. B. Cromer, A. D. Dillon, S. Liu, L. Kronik, A. M. Rappe, and A. T. Fafarman, "High chloride doping levels stabilize the perovskite phase of cesium lead iodide," *Nano Lett*, vol. 16, p. 3570, 2016.

[156] Q. Sun, P. Fassl, D. Becker-Koch, A. Bausch, B. Rivkin, S. Bai, P. E. Hopkinson, H. J. Snaith, Y. Vaynzof, Q. Sun, P. Fassl, D. Becker-Koch, A. Bausch, B. Rivkin, P. E. Hopkinson, Y. Vaynzof, S. Bai, and H. J. Snaith, "Role of microstructure in oxygen induced photodegradation of methylammonium lead triiodide perovskite films," *Advanced Energy Materials*, vol. 7, p. 1700977, 10 2017.

[157] A. J. Pearson, G. E. Eperon, P. E. Hopkinson, S. N. Habisreutinger, J. T. W. Wang, H. J. Snaith, and N. C. Greenham, "Oxygen degradation in mesoporous al2o3/ch3nh3pbi3-xclx perovskite solar

cells: Kinetics and mechanisms," *Advanced Energy Materials*, vol. 6, p. 1600014, 7 2016.

[158] A. Senocrate, G. Y. Kim, M. Grätzel, and J. Maier, "Thermochemical stability of hybrid halide perovskites," *ACS Energy Letters*, vol. 4, pp. 2859–2870, 12 2019.

[159] N. Aristidou, I. Sanchez-Molina, T. Chotchuangchutchaval, M. Brown, L. Martinez, T. Rath, and S. A. Haque, "The role of oxygen in the degradation of methylammonium lead trihalide perovskite photoactive layers," *Angewandte Chemie International Edition*, vol. 54, pp. 8208–8212, 7 2015.

[160] A. Senocrate, T. Acartürk, G. Y. Kim, R. Merkle, U. Starke, M. Grätzel, and J. Maier, "Interaction of oxygen with halide perovskites," *Journal of Materials Chemistry A*, vol. 6, pp. 10847–10855, 2018.

[161] X. Tang, M. Brandl, B. May, I. Levchuk, Y. Hou, M. Richter, H. Chen, S. Chen, S. Kahmann, A. Osvet, F. Maier, H. P. Steinrück, R. Hock, G. J. Matt, and C. J. Brabec, "Photoinduced degradation of methylammonium lead triiodide perovskite semiconductors," *Journal of Materials Chemistry A*, vol. 4, pp. 15896–15903, 10 2016.

[162] G. Abdelmageed, C. Mackeen, K. Hellier, L. Jewell, L. Seymour, M. Tingwald, F. Bridges, J. Z. Zhang, and S. Carter, "Effect of temperature on light induced degradation in methylammonium lead iodide perovskite thin films and solar cells," *Solar Energy Materials and Solar Cells*, vol. 174, pp. 566–571, 2018.

[163] G. Murugadoss, S. Tanaka, G. Mizuta, S. Kanaya, H. Nishino, T. Umeyama, H. Imahori, and S. Ito, "Light stability tests of methylammonium and formamidinium pb-halide perovskites for solar cell applications," *Japanese Journal of Applied Physics*, vol. 54, p. 08KF08, 8 2015.

[164] W. Li, M. U. Rothmann, A. Liu, Z. Wang, Y. Zhang, A. R. Pascoe, J. Lu, L. Jiang, Y. Chen, F. Huang, Y. Peng, Q. Bao, J. Etheridge, U. Bach, and Y. B. Cheng, "Phase segregation enhanced ion movement in efficient inorganic cspbibr2 solar cells," *Advanced Energy Materials*, vol. 7, pp. 1–8, 2017.

[165] G. Y. Kim, A. Senocrate, T. Y. Yang, G. Gregori, M. Grätzel, and J. Maier, "Large tunable photoeffect on ion conduction in halide perovskites and implications for photodecomposition," *Nature Materials 2018 17:5*, vol. 17, pp. 445–449, 3 2018.

[166] D. Wei, T. Wang, J. Ji, M. Li, P. Cui, Y. Li, G. Li, J. M. Mbengue, and D. Song, "Photo-induced degradation of lead halide perovskite solar cells caused by the hole transport layer/metal electrode interface," *Journal of Materials Chemistry A*, vol. 4, pp. 1991–1998, 1 2016.

[167] N. H. Nickel, F. Lang, V. V. Brus, O. Shargaieva, and J. Rappich, "Unraveling the light-induced degradation mechanisms of ch3nh3pbi3 perovskite films," *Advanced Electronic Materials*, vol. 3, p. 1700158, 12 2017.

[168] X. Chang, W. Li, L. Zhu, H. Liu, H. Geng, S. Xiang, J. Liu, and H. Chen, "Carbon-based cspbbr3 perovskite solar cells: All-ambient processes and high thermal stability," *ACS Applied Materials and Interfaces*, vol. 8, pp. 33649–33655, 12 2016.

[169] O. Malinkiewicz, A. Yella, Y. H. Lee, G. M. Espallargas, M. Graetzel, M. K. Nazeeruddin, and H. J. Bolink, "Perovskite solar cells employing organic charge-transport layers," *Nature Photonics 2013 8:2*, vol. 8, pp. 128–132, 12 2013.

[170] H. Y. Chen and G. W. Fu, "Influences of post-annealing conditions on the formation of delafossite–cufeo2 thin films," *Applied Surface Science*, vol. 288, pp. 258–264, 1 2014.

[171] A. Yella, L. P. Heiniger, P. Gao, M. K. Nazeeruddin, and M. Grätzel, "Nanocrystalline rutile electron extraction layer enables low-temperature solution processed perovskite photovoltaics with 13.7% efficiency," *Nano Letters*, vol. 14, pp. 2591–2596, 5 2014.

[172] Q. Lu, Z. Yang, X. Meng, Y. Yue, M. A. Ahmad, W. Zhang, S. Zhang, Y. Zhang, Z. Liu, and W. Chen, "A review on encapsulation technology from organic light emitting diodes to organic and perovskite solar cells," *Advanced Functional Materials*, vol. 31, p. 2100151, 6 2021.

[173] Y. Gao, Y. Hu, C. Yao, and S. Zhang, "Recent advances in lead-safe perovskite solar cells," *Advanced Functional Materials*, vol. 32, 12 2022.

[174] S. Ma, Y. Bai, H. Wang, H. Zai, J. Wu, L. Li, S. Xiang, N. Liu, L. Liu, C. Zhu, G. Liu, X. Niu, H. Chen, H. Zhou, Y. Li, and Q. Chen, "1000 h operational lifetime perovskite solar cells by ambient melting encapsulation," *Advanced Energy Materials*, vol. 10, 3 2020.

[175] J. Cao, J. Yin, S. Yuan, Y. Zhao, J. Li, and N. Zheng, "Thiols as interfacial modifiers to enhance the performance and stability of perovskite solar cells," *Nanoscale*, vol. 7, pp. 9443–9447, 5 2015.

[176] P. Chen, Y. Bai, S. Wang, M. Lyu, J.-H. Yun, L. Wang, P. Chen, Y. Bai, S. Wang, M. Lyu, J. h Yun, and L. Wang, "In situ growth of 2d perovskite capping layer for stable and efficient perovskite solar cells," *Advanced Functional Materials*, vol. 28, p. 1706923, 4 2018.

[177] N. J. Jeon, J. H. Noh, Y. C. Kim, W. S. Yang, S. Ryu, and S. I. Seok, "Solvent engineering for high-performance inorganic-organic hybrid perovskite solar cells," *Nature materials*, vol. 13, pp. 897–903, 2014.

[178] S. Sahare, H. D. Pham, D. Angmo, P. Ghoderao, J. MacLeod, S. B. Khan, S. L. Lee, S. P. Singh, and P. Sonar, "Emerging perovskite solar cell technology: Remedial actions for the foremost challenges," *Advanced Energy Materials*, vol. 11, p. 2101085, 11 2021.

[179] T. Haeger, R. Heiderhoff, and T. Riedl, "Thermal properties of metal-halide perovskites," *Journal of Materials Chemistry C*, vol. 8, pp. 14289–14311, 10 2020.

[180] R. E. Beal, D. J. Slotcavage, T. Leijtens, A. R. Bowring, R. A. Belisle, W. H. Nguyen, G. F. Burkhard, E. T. Hoke, and M. D. McGehee, "Cesium lead halide perovskites with improved stability for tandem solar cells," *Journal of Physical Chemistry Letters*, vol. 7, pp. 746–751, 2016.

[181] R. J. Sutton, G. E. Eperon, L. Miranda, E. S. Parrott, B. A. Kamino, J. B. Patel, M. T. Hörantner, M. B. Johnston, A. A. Haghighirad, D. T. Moore, and H. J. Snaith, "Bandgap-tunable cesium lead halide perovskites with high thermal stability for efficient solar cells," *Advanced Energy Materials*, vol. 6, pp. 1–6, 2016.

[182] D. Ceratti, A. Alberti, G. Mannino, I. Deretzis, E. Smecca, F. Giannazzo, S. Valastro, G. Fisicaro, and A. L. Magna, "Cspbbr3, mapbbr3, and fapbbr3 bromide perovskite single crystals: Interband critical points under dry n2 and optical degradation under humid air," *Journal of Physical Chemistry C*, vol. 125, pp. 4938–4945, 3 2021.

[183] E. T. Hoke, D. J. Slotcavage, E. R. Dohner, A. R. Bowring, H. I. Karunadasa, and M. D. McGehee, "Reversible photo-induced trap formation in mixed-halide hybrid perovskites for photovoltaics," *Chemical Science*, vol. 6, pp. 613–617, 1 2015.

[184] W. Shockley and H. J. Queisser, "Detailed balance limit of efficiency of p-n junction solar cells," *Journal of Applied Physics*, vol. 32, pp. 510–519, 3 1961.

[185] W. J. Yin, T. Shi, and Y. Yan, "Unusual defect physics in ch3nh3pbi3 perovskite solar cell absorber," *Applied Physics Letters*, vol. 104, p. 63903, 10 2014.

[186] Z. Xiao, K. Z. Du, W. Meng, J. Wang, D. B. Mitzi, and Y. Yan, "Intrinsic instability of cs2in(i)m(iii)x6 (m = bi, sb; x = halogen) double perovskites: A combined density functional theory and experimental study," *Journal of the American Chemical Society*, vol. 139, pp. 6054–6057, 5 2017.

[187] D. B. Straus, S. Guo, A. M. Abeykoon, and R. J. Cava, "Understanding the instability of the halide perovskite cspbi3 through temperature-dependent structural analysis," *Advanced Materials*, vol. 32, pp. 1–8, 2020.

[188] M. Saliba, T. Matsui, J. Y. Seo, K. Domanski, J. P. Correa-Baena, M. K. Nazeeruddin, S. M. Zakeeruddin, W. Tress, A. Abate, A. Hagfeldt, and M. Grätzel, "Cesium-containing triple cation perovskite solar cells: Improved stability, reproducibility and high efficiency," *Energy and Environmental Science*, vol. 9, pp. 1989–1997, 2016.

[189] M. Saliba, T. Matsui, K. Domanski, J. Y. Seo, A. Ummadisingu, S. M. Zakeeruddin, J. P. Correa-Baena, W. R. Tress, A. Abate, A. Hagfeldt, and M. Grätzel, "Incorporation of rubidium cations into perovskite solar cells improves photovoltaic performance," *Science (New York, N.Y.)*, vol. 354, pp. 206–209, 10 2016.

[190] Z. Li, M. Yang, J. S. Park, S. H. Wei, J. J. Berry, and K. Zhu, "Stabilizing perovskite structures by tuning tolerance factor: Formation of formamidinium and cesium lead iodide solid-state alloys," *Chemistry of Materials*, vol. 28, pp. 284–292, 1 2016.

[191] J. W. Lee, D. H. Kim, H. S. Kim, S. W. Seo, S. M. Cho, and N. G. Park, "Formamidinium and cesium hybridization for photo- and moisture-stable perovskite solar cell," *Advanced Energy Materials*, vol. 5, 10 2015.

[192] N. Liu and C. Y. Yam, "First-principles study of intrinsic defects in formamidinium lead triiodide perovskite solar cell absorbers," *Physical Chemistry Chemical Physics*, vol. 20, pp. 6800–6804, 2018.

[193] N. Kumar, J. Rani, and R. Kurchania, "Advancement in cspbbr3 inorganic perovskite solar cells: Fabrication, efficiency and stability," *Solar Energy*, vol. 221, pp. 197–205, 6 2021.

[194] M. Kulbak, D. Cahen, and G. Hodes, "How important is the organic part of lead halide perovskite photovoltaic cells? efficient cspbbr3 cells," *Journal of Physical Chemistry Letters*, vol. 6, pp. 2452–2456, 6 2015.

[195] J. Lei, F. Gao, H. Wang, J. Li, J. Jiang, X. Wu, R. Gao, Z. Yang, and S. F. Liu, "Efficient planar cspbbr3 perovskite solar cells by dual-source vacuum evaporation," *Solar Energy Materials and Solar Cells*, vol. 187, pp. 1–8, 12 2018.

[196] J. V. Patil, S. S. Mali, and C. K. Hong, "A-site rubidium cation-incorporated cspbi2br all-inorganic perovskite solar cells exceeding 17*Solar RRL*, vol. 4, pp. 1–9, 2020.

[197] Y. Guo, F. Zhao, J. Tao, J. Jiang, J. Zhang, J. Yang, Z. Hu, and J. Chu, "Efficient and hole-transporting-layer-free cspbi 2 br planar heterojunction perovskite solar cells through rubidium passivation," *ChemSusChem*, vol. 12, pp. 983–989, 2019.

[198] G. E. Eperon, V. M. Burlakov, P. Docampo, A. Goriely, and H. J. Snaith, "Morphological control for high performance, solution-processed planar heterojunction perovskite solar cells," *Advanced Functional Materials*, vol. 24, pp. 151–157, 1 2014.

[199] A. S. Tutantsev, N. N. Udalova, S. A. Fateev, A. A. Petrov, W. Chengyuan, E. G. Maksimov, E. A. Goodilin, and A. B. Tarasov, "New pigeonholing approach for selection of solvents relevant to lead halide perovskite processing," *J. Phys. Chem. C*, vol. 2020, pp. 11117–11123, 2020.

[200] J. Sun, F. Li, J. Yuan, W. Ma, J. Sun, F. Li, J. Yuan, and W. Ma, "Advances in metal halide perovskite film preparation: The role of anti-solvent treatment," *Small Methods*, vol. 5, p. 2100046, 5 2021.

[201] M. Jung, S. G. Ji, G. Kim, and S. I. Seok, "Perovskite precursor solution chemistry: from fundamentals to photovoltaic applications," *Chemical Society Reviews*, vol. 48, pp. 2011–2038, 4 2019.

[202] A. D. Taylor, Q. Sun, K. P. Goetz, Q. An, T. Schramm, Y. Hofstetter, M. Litterst, F. Paulus, and Y. Vaynzof, "A general approach to high-efficiency perovskite solar cells by any antisolvent," *Nature Communications 2021 12:1*, vol. 12, pp. 1–11, 3 2021.

[203] F. Zhang and K. Zhu, "Additive engineering for efficient and stable perovskite solar cells," *Advanced Energy Materials*, vol. 10, p. 1902579, 4 2020.

[204] L. Lanzetta, N. Aristidou, and S. A. Haque, "Stability of lead and tin halide perovskites: The link between defects and degradation," *Journal of Physical Chemistry Letters*, vol. 11, pp. 574–585, 1 2020.

[205] J. Kim, S. H. Lee, J. H. Lee, and K. H. Hong, "The role of intrinsic defects in methylammonium lead iodide perovskite," *Journal of Physical Chemistry Letters*, vol. 5, pp. 1312–1317, 4 2014.

[206] M. L. Agiorgousis, Y. Y. Sun, H. Zeng, and S. Zhang, "Strong covalency-induced recombination centers in perovskite solar cell material ch3nh3pbi3," *Journal of the American Chemical Society*, vol. 136, pp. 14570–14575, 10 2014.

[207] Y. Chen, H. Jing, F. Ling, W. Kang, T. Zhou, X. Liu, W. Zeng, Y. Zhang, L. Qi, L. Fang, and M. Zhou, "Tuning the electronic structures of all-inorganic lead halide perovskite cspbi3 via heterovalent doping: A first-principles investigation," *Chemical Physics Letters*, vol. 722, pp. 90–95, 2019.

[208] J. Euvrard, Y. Yan, and D. B. Mitzi, "Electrical doping in halide perovskites," *Nature Reviews Materials*, vol. 6, pp. 531–549, 2021.

[209] B. Dänekamp, C. Müller, M. Sendner, P. P. Boix, M. Sessolo, R. Lovrincic, and H. J. Bolink, "Perovskite-perovskite homojunctions via compositional doping," *Journal of Physical Chemistry Letters*, vol. 9, pp. 2770–2775, 2018.

[210] Z. Molenda, B. Politi, R. Clerc, M. Abbas, S. Chambon, D. M. Bassani, and L. Hirsch, "Redox-active ions unlock substitutional doping in halide perovskites," *Materials Horizons*, 2023.

[211] T. Shi, W. J. Yin, F. Hong, K. Zhu, and Y. Yan, "Unipolar self-doping behavior in perovskite ch3nh3pbbr3," *Applied Physics Letters*, vol. 106, 2015.

[212] D. Meggiolaro, D. Ricciarelli, A. A. Alasmari, F. A. Alasmary, and F. D. Angelis, "Tin versus lead redox chemistry modulates charge trapping and self-doping in tin/lead iodide perovskites," *Journal of Physical Chemistry Letters*, vol. 11, pp. 3546–3556, 2020.

[213] T. Shi, W. jian Yin, and Y. Yan, "Predictions for p-type ch 3 nh 3 pbi 3 perovskites," *The Journal of Physical Chemistry C*, vol. 118, pp. 25350–25354, 11 2014.

[214] W. Chen, H. Chen, G. Xu, R. Xue, S. Wang, Y. Li, and Y. Li, "Precise control of crystal growth for highly efficient cspbi2br perovskite solar cells," *Joule*, vol. 3, pp. 191–204, 2019.

[215] Q. Wang, Y. Shao, H. Xie, L. Lyu, X. Liu, Y. Gao, and J. Huang, "Qualifying composition dependent p and n self-doping in ch3nh3pbi3," *Applied Physics Letters*, vol. 105, 2014.

[216] A. Zohar, I. Levine, S. Gupta, O. Davidson, D. Azulay, O. Millo, I. Balberg, G. Hodes, and D. Cahen, "What is the mechanism of mapbi3 p-doping by i2? insights from optoelectronic properties," *ACS Energy Letters*, vol. 2, pp. 2408–2414, 2017.

[217] Z. Su, Y. Chen, X. Li, S. Wang, and Y. Xiao, "The modulation of optoelectronic properties of ch3nh3pbbr3 crystal," *Journal of Materials Science: Materials in Electronics*, vol. 28, pp. 11053–11058, 2017.

[218] D. Song, P. Cui, T. Wang, D. Wei, M. Li, F. Cao, X. Yue, P. Fu, Y. Li, Y. He, B. Jiang, and M. Trevor, "Managing carrier lifetime and doping property of lead halide perovskite by postannealing processes for highly efficient perovskite solar cells," *Journal of Physical Chemistry C*, vol. 119, pp. 22812–22819, 2015.

[219] Y. Yang, X. Zou, Y. Pei, X. Bai, W. Jin, and D. Chen, "Effect of doping of nai monovalent cation halide on the structural, morphological, optical and optoelectronic properties of mapbi3 perovskite," *Journal of Materials Science: Materials in Electronics*, vol. 29, pp. 205–210, 2018.

[220] X. Bai, X. Zou, J. Zhu, Y. Pei, Y. Yang, W. Jin, and D. Chen, "Effect of rb doping on modulating grain shape and semiconductor properties of mapbi3 perovskite layer," *Materials Letters*, vol. 211, pp. 328–330, 2018.

[221] L. Huang, S. Bu, D. Zhang, R. Peng, Q. Wei, Z. Ge, and J. Zhang, "Schottky/p-n cascade heterojunction constructed by intentional n-type doping perovskite toward efficient electron layer-free perovskite solar cells," *Solar RRL*, vol. 3, pp. 1–13, 2019.

[222] A. L. Abdelhady, M. I. Saidaminov, B. Murali, V. Adinolfi, O. Voznyy, K. Katsiev, E. Alarousu, R. Comin, I. Dursun, L. Sinatra, E. H. Sargent, O. F. Mohammed, and O. M. Bakr, "Heterovalent dopant incorporation for bandgap and type engineering of perovskite crystals," *Journal of Physical Chemistry Letters*, vol. 7, pp. 295–301, 2016.

[223] R. Meng, G. Wu, J. Zhou, H. Zhou, H. Fang, M. A. Loi, and Y. Zhang, "Understanding the impact of bismuth heterovalent doping on the structural and photophysical properties of ch 3 nh 3 pbbr 3 halide perovskite crystals with near-ir photoluminescence," *Chemistry - A European Journal*, vol. 25, pp. 5480–5488, 2019.

[224] Q. Chen, L. Chen, F. Ye, T. Zhao, F. Tang, A. Rajagopal, Z. Jiang, S. Jiang, A. K. Jen, Y. Xie, J. Cai, and L. Chen, "Ag-incorporated organic-inorganic perovskite films and planar heterojunction solar cells," *Nano Letters*, vol. 17, pp. 3231–3237, 2017.

[225] S. Zhou, Y. Ma, G. Zhou, X. Xu, M. Qin, Y. Li, Y. J. Hsu, H. Hu, G. Li, N. Zhao, J. Xu, and X. Lu, "Ag-doped halide perovskite nanocrystals for tunable band structure and efficient charge transport," *ACS Energy Letters*, vol. 4, pp. 534–541, 2019.

[226] Z. Fang, H. He, L. Gan, J. Li, and Z. Ye, "Understanding the role of lithium doping in reducing nonradiative loss in lead halide perovskites," *Advanced Science*, vol. 5, pp. 1–6, 2018.

[227] Q. Jiang, M. Chen, J. Li, M. Wang, X. Zeng, T. Besara, J. Lu, Y. Xin, X. Shan, B. Pan, C. Wang, S. Lin, T. Siegrist, Q. Xiao, and Z. Yu, "Electrochemical doping of halide perovskites with ion intercalation," *ACS Nano*, vol. 11, pp. 1073–1079, 2017.

[228] P. Schulz, L. L. Whittaker-Brooks, B. A. Macleod, D. C. Olson, Y. L. Loo, and A. Kahn, "Electronic level alignment in inverted organometal perovskite solar cells," *Advanced Materials Interfaces*, vol. 2, 2015.

[229] S. Olthof and K. Meerholz, "Substrate-dependent electronic structure and film formation of mapbi 3 perovskites," *Scientific Reports*, vol. 7, pp. 1–10, 2017.

[230] E. M. Miller, Y. Zhao, C. C. Mercado, S. K. Saha, J. M. Luther, K. Zhu, V. Stevanović, C. L. Perkins, and J. V. D. Lagemaat, "Substrate-controlled band positions in ch3nh3pbi3 perovskite films," *Physical Chemistry Chemical Physics*, vol. 16, pp. 22122–22130, 2014.

[231] A. Zohar, M. Kulbak, I. Levine, G. Hodes, A. Kahn, and D. Cahen, "What limits the open-circuit voltage of bromide perovskite-based solar cells?," *ACS Energy Letters*, vol. 4, pp. 1–7, 2019.

[232] P. Cui, D. Wei, J. Ji, H. Huang, E. Jia, S. Dou, T. Wang, W. Wang, and M. Li, "Planar p–n homojunction perovskite solar cells with efficiency exceeding 21.3%," *Nature Energy*, vol. 4, pp. 150–159, 2019.

[233] W. J. Yin, J. H. Yang, J. Kang, Y. Yan, and S. H. Wei, "Halide perovskite materials for solar cells: a theoretical review," *Journal of Materials Chemistry A*, vol. 3, pp. 8926–8942, 4 2015.

[234] H. Huang, M. I. Bodnarchuk, S. V. Kershaw, M. V. Kovalenko, and A. L. Rogach, "Lead halide perovskite nanocrystals in the research spotlight: Stability and defect tolerance," *ACS Energy Letters*, vol. 2, pp. 2071–2083, 9 2017.

[235] J. S. Park, S. Kim, Z. Xie, and A. Walsh, "Point defect engineering in thin-film solar cells," *Nature Reviews Materials*, vol. 3, pp. 194–210, 7 2018.

[236] L. K. Ono, S. Liu, and Y. Qi, "Reducing detrimental defects for high-performance metal halide perovskite solar cells," *Angewandte Chemie International Edition*, vol. 59, pp. 6676–6698, 4 2020.

[237] A. Stewart, A. Julien, D. Regaldo, P. Schulz, B. M. Soucase, D. Ceratti, and P. López-Varo, "Shedding light on electronically doped perovskites," *Materials Today Chemistry*, vol. 29, p. 101380, 4 2023.

[238] S. G. Motti, D. Meggiolaro, A. J. Barker, E. Mosconi, C. A. R. Perini, J. M. Ball, M. Gandini, M. Kim, F. D. Angelis, and A. Petrozza, "Controlling competing photochemical reactions stabilizes perovskite solar cells," *Nature Photonics*, vol. 13, pp. 532–539, 8 2019.

[239] D. Meggiolaro, S. G. Motti, E. Mosconi, A. J. Barker, J. Ball, C. A. R. Perini, F. Deschler, A. Petrozza, and F. D. Angelis, "Iodine chemistry determines the defect tolerance of lead-halide perovskites," *Energy and Environmental Science*, vol. 11, pp. 702–713, 3 2018.

[240] C. Eames, J. M. Frost, P. R. Barnes, B. C. O'Regan, A. Walsh, and M. S. Islam, "Ionic transport in hybrid lead iodide perovskite solar cells," *Nature Communications 2015 6:1*, vol. 6, pp. 1–8, 6 2015.

[241] B. Das, I. Aguilera, U. Rau, and T. Kirchartz, "Effect of doping, photodoping, and bandgap variation on the performance of perovskite solar cells," *Advanced Optical Materials*, vol. 2101947, 2022.

[242] F. Peña-Camargo, J. Thiesbrummel, H. Hempel, A. Musiienko, V. M. L. Corre, J. Diekmann, J. Warby, T. Unold, F. Lang, D. Neher, and M. Stolterfoht, "Revealing the doping density in perovskite solar cells and its impact on device performance," *Applied Physics Reviews*, vol. 9, 2022.

[243] R. Long, J. Liu, and O. V. Prezhdo, "Unravelling the effects of grain boundary and chemical doping on electron-hole recombination in ch3nh3pbi3 perovskite by time-domain atomistic simulation," *Journal of the American Chemical Society*, vol. 138, pp. 3884–3890, 3 2016.

[244] W. Hui, L. Chao, H. Lu, F. Xia, Q. Wei, Z. Su, T. Niu, L. Tao, B. Du, D. Li, Y. Wang, H. Dong, S. Zuo, B. Li, W. Shi, X. Ran, P. Li, H. Zhang, Z. Wu, C. Ran, L. Song, G. Xing, X. Gao, J. Zhang, Y. Xia, Y. Chen, and W. Huang, "Stabilizing black-phase formamidinium perovskite formation at room temperature and high humidity," *Science*, vol. 371, pp. 1359–1364, 3 2021.

[245] Q. Jiang, J. Tong, Y. Xian, R. A. Kerner, S. P. Dunfield, C. Xiao, R. A. Scheidt, D. Kuciauskas, X. Wang, M. P. Hautzinger, R. Tirawat, M. C. Beard, D. P. Fenning, J. J. Berry, B. W. Larson, Y. Yan, and K. Zhu, "Surface reaction for efficient and stable inverted perovskite solar cells," *Nature*, vol. 611, pp. 278–283, 2022.

[246] Universitat Politècnica de València, "Microscopio electrónico de barrido de emisión de campo con cañón de iones focalizados (fib)," *https://www.upv.es/entidades/SME/info/854396normalc.html*, 2023.

[247] L. Krückemeier, U. Rau, M. Stolterfoht, and T. Kirchartz, "How to report record open-circuit voltages in lead-halide perovskite solar cells," *Advanced Energy Materials*, vol. 10, p. 1902573, 1 2020.

[248] S. Zeiske, O. J. Sandberg, N. Zarrabi, C. M. Wolff, M. Raoufi, F. Peña-Camargo, E. Gutierrez-Partida, P. Meredith, M. Stolterfoht, and A. Armin, "Static disorder in lead halide perovskites," *Journal of Physical Chemistry Letters*, vol. 13, pp. 7280–7285, 8 2022.

[249] K. Datta, B. T. van Gorkom, Z. Chen, M. J. Dyson, T. P. van der Pol, S. C. Meskers, S. Tao, P. A. Bobbert, M. M. Wienk, and R. A. Janssen, "Effect of light-induced halide segregation on the performance of mixed-halide perovskite solar cells," *ACS Applied Energy Materials*, vol. 4, pp. 6650–6658, 7 2021.

[250] F. Babbe and C. M. Sutter-Fella, "Optical absorption-based in situ characterization of halide perovskites," *Advanced Energy Materials*, vol. 10, p. 1903587, 7 2020.

[251] A. McClelland and M. Mankin, *Optical Measurements for Scientists and Engineers: A Practical Guide.* Cambridge University Press, 4 2018.

[252] P. Y. Yu and M. Cardona, *Fundamentals of semiconductors : physics and materials properties.* Springer, 2010.

[253] P. Caprioglio, M. Stolterfoht, C. M. Wolff, T. Unold, B. Rech, S. Albrecht, and D. Neher, "On the relation between the open-circuit voltage and quasi-fermi level splitting in efficient perovskite solar cells," *Advanced Energy Materials*, vol. 9, p. 1901631, 9 2019.

[254] C. M. Sutter-Fella, Y. Li, M. Amani, J. W. Ager, F. M. Toma, E. Yablonovitch, I. D. Sharp, and A. Javey, "High photoluminescence quantum yield in band gap tunable bromide containing mixed halide perovskites," *Nano Letters*, vol. 16, pp. 800–806, 1 2016.

[255] HR Universal Systems Inc., "Setfos - simulation software for organic and perovskite solar cells and leds," 2023.

[256] Delft University of Technology, "Advanced semiconductor analysis software," 2023.

[257] SILVACO Inc., "Silvaco," 2023.

[258] N. E. Courtier, J. M. Cave, A. B. Walker, G. Richardson, and J. M. Foster, "Ionmonger: a free and fast planar perovskite solar cell simulator with coupled ion vacancy and charge carrier dynamics," *Journal of Computational Electronics*, vol. 18, pp. 1435–1449, 2019.

[259] M. Burgelman, P. Nollet, and S. Degrave, "Modelling polycrystalline semiconductor solar cells," *Thin Solid Films*, vol. 361, pp. 527–532, 2 2000.

[260] M. Burgelman, K. Decock, S. Khelifi, and A. Abass, "Advanced electrical simulation of thin film solar cells," *Thin Solid Films*, vol. 535, pp. 296–301, 2013.

[261] J. Diekmann, P. Caprioglio, M. H. Futscher, V. M. L. Corre, S. Reichert, F. Jaiser, M. Arvind, L. P. Toro, E. Gutierrez-Partida, F. Peña-Camargo, C. Deibel, B. Ehrler, T. Unold, T. Kirchartz, D. Neher, and M. Stolterfoht, "Pathways toward 30the role of mobile ions," *Solar RRL*, vol. 5, 2021.

[262] E. Raza, Z. Ahmad, F. Aziz, M. Asif, A. Ahmed, K. Riaz, J. Bhadra, and N. J. Al-Thani, "Numerical simulation analysis towards the effect of charge transport layers electrical properties on cesium based ternary cation perovskite solar cells performance," *Solar Energy*, vol. 225, pp. 842–850, 2021.

Chapter 2

Publications

2.1 Inorganic-Perovskites: Improved Film and Crystal Quality of CsPbIBr$_2$ when Doped with Rubidium

Inorganic perovskites improved film and crystal quality of CsPbIBr$_2$ when doped with rubidium

Alexander W. Stewart[1], Amal Bouich[1,2,*] , and Bernabé Marí[1]

[1] *Institut de Disseny i Fabricació, Universitat Politècnica de València, Camí de Vera, 46022 València, Spain*
[2] *Laboratory (LMEE), University of Ibn Tofail, Av. de L'Université, BP 242 Kenitra, Morocco*

ABSTRACT

In this work CsPbIBr$_2$ is doped with rubidium, where up to 12% of caesium atoms are replaced with those of rubidium. The obtained Cs$_{1-x}$Rb$_x$PbIBr$_2$, x= (0, 0.02, 0.04, 0.06, 0.08, 0.10, 0.12), films were characterized by X-ray diffraction (XRD), the scanning electron microscope (SEM), photoluminescence (PL) and UV–visible spectroscopy. The integration of Rb$^+$ ions into the lattice leads to a detectable change in optoelectronic and morphological structure. Substituting 6% of caesium atoms yields the best results, eliminating pinholes and elevating crystallite size and absorption coefficient by 116 and 125%, respectively. Other novel observations, of particular interest, include a slight increase in band-gap energy from 2.1 eV to 2.14 eV and a decrease in stability. Over a period of 15 days, where temperature and relative humidity kept at 23 °C and 20%, respectively, a larger amount of degradation was seen to take place as rubidium content was increased. Therefore, the doping of CsPbIBr$_2$ with rubidium is most useful in the case where specifically film and crystal quality are desired to be targeted.

1 Introduction

The rise of perovskite solar cells (PSCs) has been accompanied by an unprecedented increase in power conversion efficiency (PCE) from 3.8% to 25.5%, in just over a decade [1, 2]. Perovskites are crystal structures of the composition ABX$_3$. In many cases, they can be predicted using the Goldschmidt tolerance and the octahedral factor [3–5]. Furthermore, they tend to have a cubic, tetragonal, or orthorhombic structure corresponding to a high, intermediate and low temperature phase, respectively [6]. Methylammonium-based devices catapulted perovskites into the spotlight, having shown exceptional optoelectronic properties including high absorption coefficients, long-carrier lifetimes, favourable spin–orbit coupling, low exciton binding energy, high proportions of free carriers, high mobilities and large diffusion lengths [7–11]. The combination of these outstanding properties with perovskite's low cost and high scalability demonstrates why these materials have gained such notoriety in the photovoltaic community [12]. That said, there remains one

Address correspondence to E-mail: Bouich.amal@gmail.com

Inorganic-Perovskites: Improved Film and Crystal Quality of CsPbIBr$_2$ when Doped with Rubidium

Alexander W. Stewart[a], Amal Bouich[a,b], Bernabé Marí Soucase[a]

[a] Institut de Disseny i Fabricació, Universitat Politècnica de València,
Camí de Vera, València, Spain 46022
[b] Laboratory (LMEE), University of Ibn Tofail Av. de L'Université,
Kenitra, Morocco BP 242

Corresponding author email: Bouich.amal@gmail.com

Abstract:

In this work $CsPbIBr_2$ is doped with rubidium, where up to 12% of caesium atoms are replaced with those of rubidium. The obtained $Cs_{1-x}Rb_xPbIBr_2$, x= (0, 0.02, 0.04, 0.06, 0.08, 0.10, 0.12), films were characterized by X-ray diffraction (XRD), the scanning electron microscope (SEM), photoluminescence (PL) and UV-visible spectroscopy. The integration of Rb+ ions into the lattice leads to a detectable change in opto-electronic and morphological structure. Substituting 6% of caesium atoms yields the best results, eliminating pinholes, and elevating crystallite size and absorption coefficient by 116% and 125%, respectively. Other novel observations, of particular interest, include a slight increase in band-gap energy from 2.1eV to 2.14eV, and a decrease in stability. Over a period of 15 days, where temperature and relative humidity kept at 23°C and 20% respectively, a larger amount of degradation was seen to take place as rubidium content was increased. Therefore, the doping of $CsPbIBr_2$ with rubidium is most useful in the case where specifically film and crystal quality are desired to be targeted.

2.1.1 Introduction

The rise of perovskite solar cells (PSCs) has been accompanied by an unprecedented increase in power conversion efficiency (PCE), from 3.8% to 25.5%, in just over a decade [1, 2]. Perovskites are crystal structures of the composition ABX_3. In many cases, they can be predicted using the Goldschmidt tolerance and the octahedral-factor [3–5]. Furthermore, they tend to have a cubic, tetragonal, or orthorhombic structure corresponding to a high, intermediate, low temperature phase, respectively [6]. Methylammonium-based devices catapulted perovskites into the spotlight, having shown exceptional optoelectronic properties including high absorption coefficients, long-carrier lifetimes, favourable spin-orbit coupling, low exciton binding-energy, high proportions of free carriers, high mobilities and large diffusion lengths [7–11]. The combination of these outstanding properties with perovskite's low-cost and high scalability, demonstrates why these materials have gained such notoriety in the photovoltaic community [12]. That said, there remains one fundamental property which plagues methylammonium-devices, and that is their inherent instability. This is catalysed by moisture, radiation and temperature, factors which the PSC will unavoidably be exposed to during its working life [13–16].

Since methylammonium-based devices degrade irreversibly back into the precursor components, one of which is volatile, partial substitution with an inorganic cation such as caesium arose as a way to harness the aforementioned opto-electronic properties while increasing stability [16, 17]. Similarly, this idea was taken further, and completely inorganic devices were investigated. While $CsPbI_3$-based devices showed desirable band-gaps, they too demonstrated degradation, albeit via a reversible phase change [18]. On the other hand, $CsPbBr_3$ showed exceptional stability, however this came at the cost of increasing the band-gap. For these reasons, iodine-bromine alloys such as $CsPbI_2Br$ and $CsPbIBr_2$ became of interest. These alloys strike a compromise between band-gap and stability, the latter being the subject of this work [19, 20].

To date, the highest obtained PCE for a $CsPbIBr_2$ based device is 10.71%, which is just over half of the Shockley-Queisser limit, thus revealing research opportunities in the field [21, 22]. For tables on device PCEs and an overview of the field, see [22, 23]. While the relatively high band-gap of $CsPbIBr_2$ will limit its use in single-junction cells, its true potential may be harnessed as a top-cell in a multi-junction, as highlighted by Oxford-PV's recent breakthrough [24, 25]. Until now, devices have been prepared via one-step spin-coating, a gas-assisted method, spray-assisted deposition, dual-source thermal evaporation and two-step spin-coating [20, 22, 26–30]. As it stands, one of the biggest problems in the field is the consistent deposition of high-quality films, with many reporting a high number of pinholes and small grain sizes [20, 23, 26, 29]. Some of the methods investigated to improve

films include: the use of antisolvent to improve coverage and morphology, guanidinium iodide for surface passivation, adding a small amount of $PbCl_2$ to the precursor solution, light soaking, intermolecular exchange, precursor solution aging, band alignment via interface engineering and doping with Magnesium [22, 23, 26, 30]. The latter being related most closely to this work, where the effects of doping $CsPbIBr_2$ with rubidium is investigated. While doping with Rb+ ions has been shown to have a beneficial effect on the sister materials $CsPbIBr_2$ and $CsPbBr_3$, as of yet, there appears to be a lack of equivalent research carried out on $CsPbIBr_2$ [31–33].

2.1.2 Methodology

Materials

All chemicals were purchased from Tokyo Chemical Industry unless otherwise stated in parenthesis. The precursor solution consisted of caesium iodide (CsI), lead bromide ($PbBr_2$) and rubidium iodide (RbI, 99% from Alfa Aesar), dissolved in dimethyl sulfoxide (DMSO 99.9%).

Thin film preparation

The $Cs_{1-x}Rb_xPbIBr_2$ thin films were deposited on top of fluorine-doped tin oxide (FTO) substrates (TEC 15A) by one step spin coating technique, with an area of $2.5cm^2$, purchased from XOP Glass. Substrates were cleaned for 15 minutes in detergent, ethanol (LabKem), acetone (VWR Chemicals) and isopropanol (VWR Chemicals) in an ultrasonic bath before a further 15 minutes in the UV-Ozone, manufactured by Ossila. The $CsPbIBr_2$ precursor solution was prepared by allowing CsI and $PbBr_2$ to dissolve completely in DMSO (1 mL), at room temperature. To dope $CsPbIBr_2$ with RbI, 0.5M solutions with molar ratios of 100-x: x: 100 (CsI: RbI: $PbBr_2$) were prepared, where x is the rubidium doping percentage. after the solution was mixed at 85 temperature and Solutions were left to heat overnight in the glovebox. Samples were statically spin coated at 3500 RPM for 30 seconds, after which they were annealed for 5 minutes at 50°C and then 250°C. Samples were stored in inert N_2 atmosphere until used.

Characterisation techniques

Thin films of $Cs_{1-x}Rb_xPbIBr_2$, where x = 0%, 2%, 4%, 6%, 8%, 10% and 12%, were characterized by X-ray diffraction (XRD) using the RIGAKU Ultima IV with Cu kα radiation ($\lambda = 1.5418$ Å). Morphology images were taken using the scanning electron microscope (SEM) Quanta 200-FEI with an applied voltage of 1.5 kV. Optical properties were performed with an Ocean Optics HR4000 spectrophotometer and photoluminescence (PL) emission was driven by an He-Cd laser with a wavelength of $\lambda = 405$ nm.
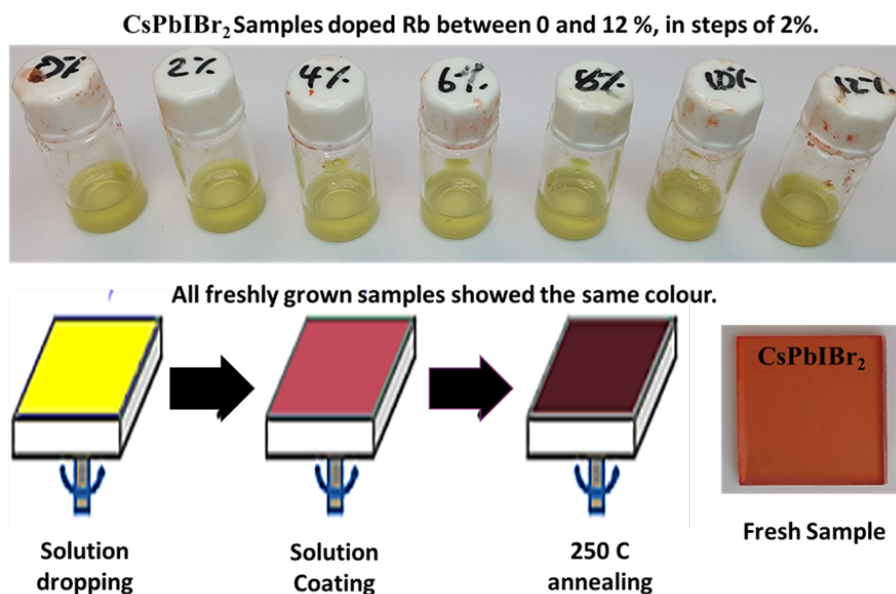
Figure 1: Schematic of the one-step spin-coating procedure for the mixed-halide perovskite $Cs_{1-x}Rb_xPbIBr_2$, where x = 0%, 2%, 4%, 6%, 8%, 10% and 12%.

2.1.3 Results and Discussion

To characterize the X-ray diffraction (XRD) peaks, a Rietveld Refinement was carried out. The refinement itself was found to be exceptionally precise, with Rwp = 5.94% and Rp = 4.30% (Figure 2 (b)). These values reflect the accordance between the predicted and measured spectra, with 0% corresponding to identical curves. The crystals were found to be strongly oriented in the (100) plane, with the bright peaks at 14.9° and 30.1°corresponding to the (100) and (200) indices. A small peak at 22° is believed to be attributed to the (110) plane. These results are in accordance with the literature22,26,33, except for one study that found an orthorhombic structure with the primary peak at 30° belonging to the (220) plane 29. The lattice was found to be tetragonal, and belonging to the Pm-3m space group, with a=b=5.93278 ±0.00030 and c=5.88519 ± 0.00842. These results are in accordance with those found elsewhere [23, 24] (see Fig.1 in supplementary materials).

Interestingly, it seems that the full width at half maximum (FWHM) of the main diffraction peaks reaches its narrowest when 6% of caesium atoms are substituted with rubidium (see Fig.2 in supplementary materials). Application of the Scherrer equation reveals that crystallite sizes take an approximately parabolic form, with a maximum at 6% [34]. This maximum corresponds to an increase in crystallite size of 117% and 116%,
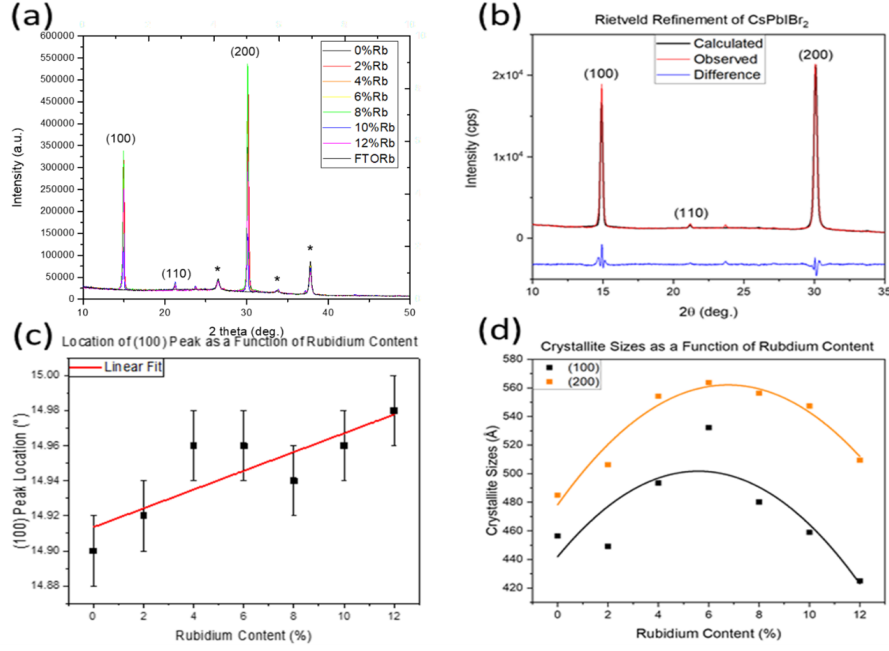
Figure 2: XRD results (a) XRD pattern perovskite $Cs_{1-x}Rb_xPbIBr_2$, where x = 0%, 2%, 4%, 6%, 8%, 10% and 12%. (b) Rietveld Refinement of reference sample ($CsPbIBr_2$ with no doping) (c) The location of the (100) peak as rubidium content is increased. The error bars correspond to the resolution of the equipment. Similar results are obtained for the (200) peak. (d) Crystallite sizes calculated from the FWHM of the major diffraction peaks corresponding to the (100) and (200) planes.

corresponding to the (100) and (200) peaks respectively, when compared to the non-doped sample. As the concentration of rubidium ions in the precursor solution was increased, all the peaks in the sample were systematically shifted. This can be seen for the (200) and (100) plane (Figure 2 (d)). This is likely attributable to the fact that Rb^+ (1.52A) has a smaller ionic radius than Cs^+ (1.67A), therefore a shift to higher angles correspond to a contraction of the unit cell [33]. Moreover, the contraction of the unit cell suggests that rubidium ions are substituting caesium rather than occupying interstitial sites.

To independently confirm the insertion of rubidium into the lattice, energy-dispersive X-ray spectroscopy (EDS) was performed (see Fig 2 in supplementary materials). Given that Rb^+ ions substitute Cs^+ ions as A site cations, it is possible to determine their population as

$$Rb^+_{population} = \frac{Rb^+(\%)}{Rb^+(\%) + Cs^+(\%)} \tag{2.1}$$

Table 2.1: The grain size, the full width at half maximum (FWHM) , dislocation density and lattice strain of XRD of $Cs_{1-x}Rb_xPbIBr_2$, where x = 0%, 6%, 8% and 12% thin films.

Sample	Grain size (nm)	FWHM (deg)	Dislocation density (cm^{-1})	Lattice strain (2ϵ)
Pure	480	0.1833	0.50 x10^{-5}	0.40
6% Rb	570	0.1572	0.39 x10^{-5}	0.65
12% Rb	420	0.1969	0.59 x10^{-5}	0.28

Where $Rb^+(\%)$ and $Cs^+(\%)$ are the atomic percentages measured. Plotting this against precursor concentration yields a linear relationship with $Rb_p^+ opulation \approx Rb_precursor^+$, suggesting that all the rubidium precursor is fully integrated into the structure (Figure 3(b)).
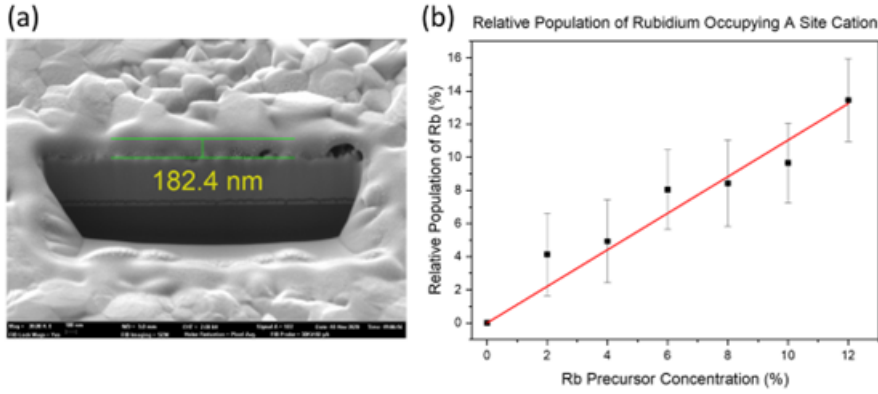

Figure 3: (a) SEM image taken during the measurement of the 6% sample's thickness (b) Measured dopant percentage as a function of dopant precursor percentage. Error bars show one standard deviation in the measurement.

Using the focused ion beam (FIB) it was possible to design a cut in the sample, allowing the thickness of the sample to be measured (Figure 3 (a)). Carrying out this process for all samples, an average thickness of 195nm was found, with a standard deviation of 13nm.

Observations carried out using the scanning electron microscope (SEM) revealed that the sample doped with 6% rubidium had the best quality overall, with no pinholes and uniform coverage (see Figure 4). The reference sample showed an abundance of pinholes, however increasing the rubidium content caused a decrease in the density of pinholes. Once the rubidium concentration was increased past 6%, the film quality decreased. This can be seen in the 8% sample (Figure 4 (d)) where small pinholes are beginning to form once more. It is believed that these pinholes form when pockets of

solvent remain within the material during the crystallization process [23]. Measuring the absorbance of the freshly prepared samples, it was possible to calculate their absorption spectrum using the thickness values (Figure 5 (a)). All samples have an absorption coefficient of around 2×10^4 cm^{-1} above 2.2eV and show the onset of the optical band edge around 2.07eV ($\approx$600nm), which agrees with values found elsewhere [20, 29]. Whilst most samples had a comparable absorption coefficient to the non-doped sample, the 6% sample increased by 125%. Intuitively, this makes sense, since the 6% sample showed no pinholes in SEM (Figure 4 (c)) and larger crystallite sizes (Figure 2(d)), suggesting it would be a more effective absorber. It should be noted, however, that the absorption coefficient scales inversely with layer thickness and as such the precision of these values are limited by the methods employed previously (Figure 3(a)) [20, 29]. Employing the Tauc plot to estimate the band-gap, band-gap values increased slightly, from 2.1 to 2.14eV, as rubidium content was increased. Similar parts of the spectra were taken for the linear fit, to minimize any random errors (Figure 5(b)).
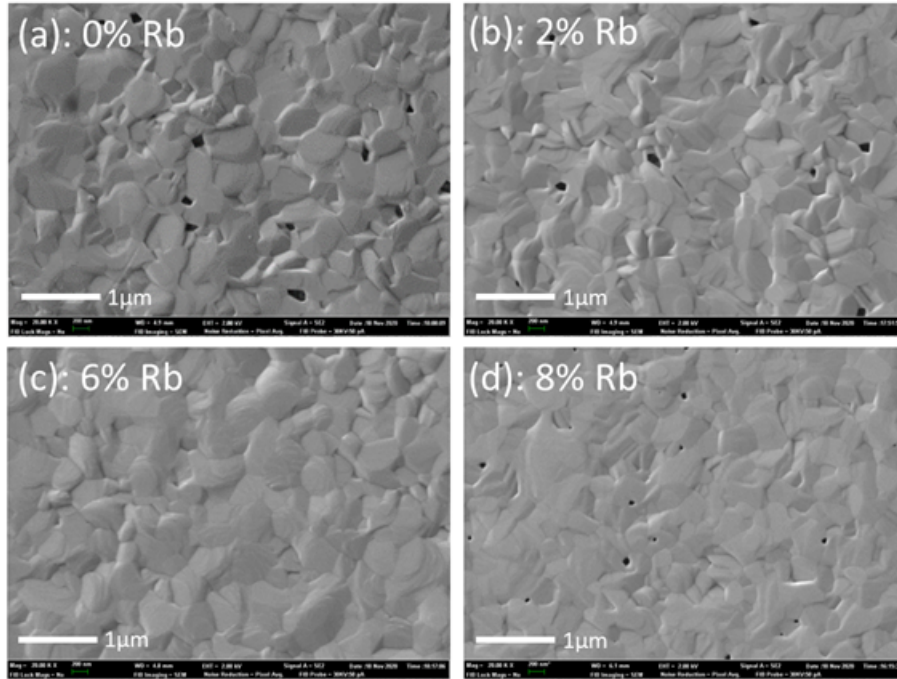

Figure 4: SEM images, at 20,000 times magnification, of CsPbIBr$_2$ doped with (a) no rubidium (reference sample), where large pinholes can be seen (b) 2% rubidium, where pinhole size and density are seen to decrease with respect to the reference sample (c) 6% rubidium, no pinholes (d) 8% rubidium, were small pinholes are formed.

To model the photoluminescence (PL) spectra taken, a predicted spec-

trum was constructed by summing two Gaussian functions of the form

$$y = y_0 + \frac{A}{\omega\sqrt{\pi/2}} e^{-\frac{2(x-x_c)^2}{\omega^2}} \tag{2.2}$$

Where y_0, A, x_c and ω are constants. Using this method, it was possible to discern a primary and secondary component of a given PL spectrum (Figure 5(c)). The R_2 value is a statistical measure of the similarity between curves, in the case that they are identical it is equal to 1. For these models, all R_2 values lay above 0.996, except for the 4% sample which had significantly more background noise. It is thought that the secondary components of the PL spectra arise, under illumination, due to the formation of iodine rich phases [28] (see Table 1 in supplementary materials).
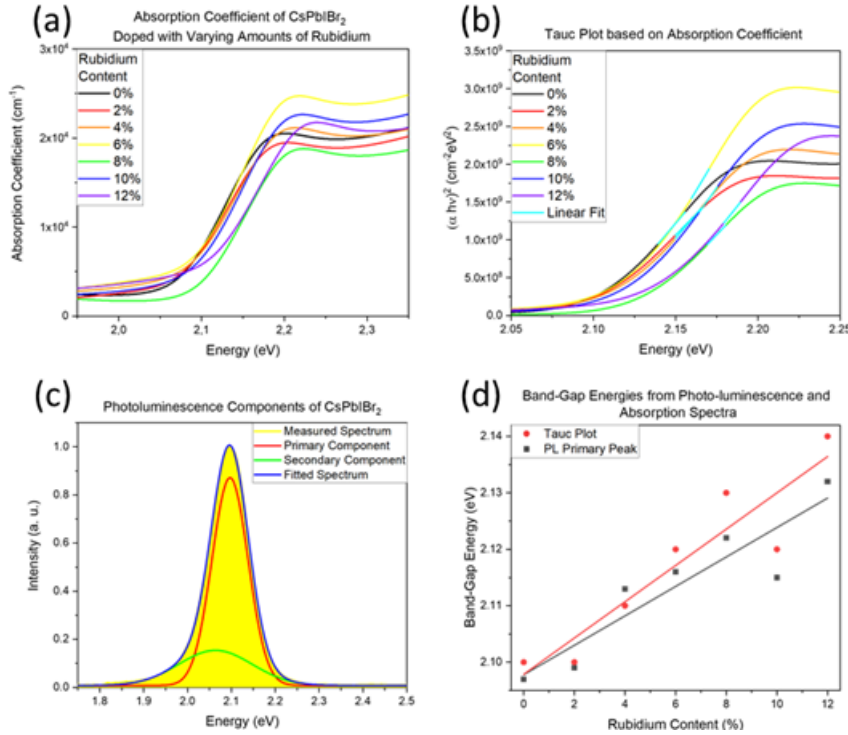

Figure 5: (a) Absorption coefficients of the freshly prepared samples (b) Bandgap estimation using the Tauc plot (c) Decomposition of the reference sample's PL spectrum into components (d) band-gap values calculated from PL and the Tauc plot.

Combining the results from PL measurements with those from the absorption coefficient, it can be said that an increase in band-gap is almost certainly taking place as elevated quantities of rubidium are incorporated into the lattice (Figure 5 (d)). Given the limitations of the Tauc plot, band-gap values are almost perfectly in accordance with those taken from

the primary PL component. Moreover, both techniques yield the desired band-gap value for the reference sample [20, 23, 26, 29]. To investigate the effect of rubidium incorporation on the stability $CsPbIBr_2$, the absorption coefficients were measured after the samples had been stored in ambient conditions (Figure 6 (a)). A batch of newly synthesized samples were kept in the laboratory for 15 days, during which temperature and relative humidity kept constant, at 23°C and 20% respectively.
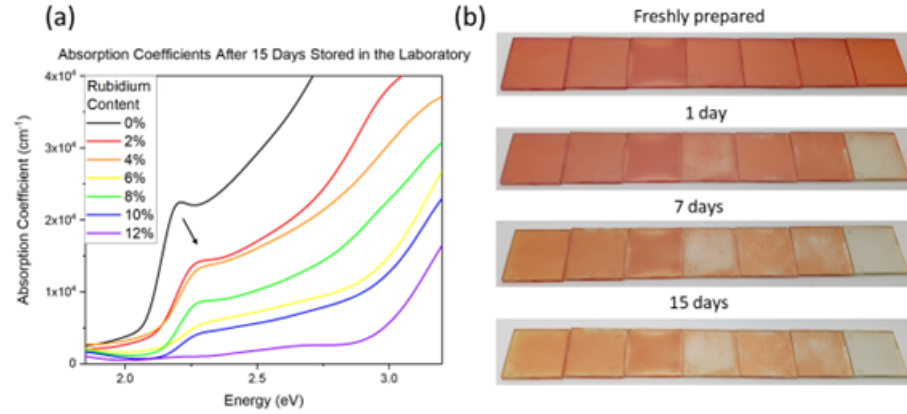

Figure 6: (a) Absorption coefficients of $CsPbIBr_2$ doped with varying amounts of rubidium (b) Photos where degradation can be seen to be taking place in the samples over the study.

In general, higher rubidium content is shown to correlate with accelerated degradation, demonstrated by films with larger quantities of Rb experiencing larger shifts in energy (Figure 6 (a)). Most likely, the absorption coefficient curves shifting to higher energies corresponds to a progressive change from the meta-stable high-temperature α-phase towards the intermediate-temperature δ-phase, which is stable at room temperature. The shift is especially pronounced for the 12% sample, which had changed phase within one day (Figure 6 (b)). It is possible that due to the decreased ionic radius of rubidium, the volumetric ratio between the PbX_6 octahedra and A-site cations decreases, aggravating its thermodynamic instability [18].

2.1.4 Conclusion

In this study, the effect of rubidium incorporation in the $CsPbIBr_2$ lattice is investigated via XRD, SEM, EDS and optical measurements. The correct incorporation of rubidium is independently confirmed from XRD peak shifts and EDS results. Grain size is shown to be a function of dopant content, taking its maximum value when 6% of caesium atoms are replaced with rubidium. SEM measurements reveal that the methodology yields layers with an average thickness of 195nm ($\sigma = 13$nm). In terms of morphology,

the incorporation of rubidium, up to 6%, seems to favourably affect film coverage by decreasing pinholes. Optical measurements reveal that samples have an absorption coefficient around 2×10^4 cm^{-1} above 2.2eV, with the 6% sample having a superior absorption coefficient. Absorption coefficient and PL measurements both suggest a slight increase in band-gap as rubidium content is increased. Overall, the sample with 6% rubidium showed the best results. Investigation into the stability of the prepared samples reveals that rubidium incorporation has an adverse effect on stability. While doping CsPbIBr$_2$ with rubidium seems to decrease stability, the technique brings a myriad of improvements to the crystal and film quality. As such it should be considered as a useful tool when developing high quality thin films.

2.1.5 Acknowledgments

Bibliography

[1] A. Kojima, K. Teshima, Y. Shirai, and T. Miyasaka, "Organometal halide perovskites as visible-light sensitizers for photovoltaic cells," *Journal of the American Chemical Society*, vol. 131, pp. 6050–6051, 2009. First perovskite solar cell.

[2] National Renewable Energy Laboratory, "Best research-cell efficiency chart — photovoltaic research," 2023.

[3] V. M. Goldschmidt, "Die gesetze der krystallochemie," *Die Naturwissenschaften*, vol. 14, pp. 477–485, 5 1926.

[4] C. J. Bartel, C. Sutton, B. R. Goldsmith, R. Ouyang, C. B. Musgrave, L. M. Ghiringhelli, and M. Scheffler, "New tolerance factor to predict the stability of perovskite oxides and halides," *Science Advances*, vol. 5, p. eaav0693, 2 2019.

[5] C. Li, X. Lu, W. Ding, L. Feng, Y. Gao, and Z. Guo, "Formability of abx 3 (x = f, cl, br, i) halide perovskites," *Acta Crystallographica Section B: Structural Science*, vol. 64, pp. 702–707, 2008.

[6] A. Miyata, A. Mitioglu, P. Plochocka, O. Portugall, J. T. W. Wang, S. D. Stranks, H. J. Snaith, and R. J. Nicholas, "Direct measurement of the exciton binding energy and effective masses for charge carriers in organic-inorganic tri-halide perovskites," *Nature Physics*, vol. 11, pp. 582–587, 2015.

[7] T. Wang, B. Daiber, J. M. Frost, S. A. Mann, E. C. Garnett, A. Walsh, and B. Ehrler, "Indirect to direct bandgap transition in methylammonium lead halide perovskite," *Energy and Environmental Science*, vol. 10, pp. 509–515, 2017.

[8] V. D'Innocenzo, G. Grancini, M. J. Alcocer, A. R. S. Kandada, S. D. Stranks, M. M. Lee, G. Lanzani, H. J. Snaith, and A. Petrozza, "Excitons versus free charges in organo-lead tri-halide perovskites," *Nature Communications*, vol. 5, 4 2014.

[9] L. M. Herz, "Charge-carrier mobilities in metal halide perovskites: Fundamental mechanisms and limits," *ACS Energy Letters*, vol. 2, pp. 1539–1548, 7 2017.

[10] M. J. P. Alcocer, T. Leijtens, L. M. Herz, A. Petrozza, and H. J. Snaith, "Electron-hole diffusion lengths exceeding trihalide perovskite absorber," *Science*, vol. 342, pp. 341–344, 2013.

[11] G. Xing, N. Mathews, S. S. Lim, N. Yantara, X. Liu, D. Sabba, M. Grätzel, S. Mhaisalkar, and T. C. Sum, "Low-temperature solution-processed wavelength-tunable perovskites for lasing," *Nature Materials 2014 13:5*, vol. 13, pp. 476–480, 3 2014.

[12] H. J. Snaith, "Perovskites: The emergence of a new era for low-cost, high-efficiency solar cells," *Journal of Physical Chemistry Letters*, vol. 4, pp. 3623–3630, 11 2013.

[13] Y. Han, S. Meyer, Y. Dkhissi, K. Weber, J. M. Pringle, U. Bach, L. Spiccia, and Y. B. Cheng, "Degradation observations of encapsulated planar ch3nh3pbi3 perovskite solar cells at high temperatures and humidity," *Journal of Materials Chemistry A*, vol. 3, pp. 8139–8147, 2015.

[14] G. Divitini, S. Cacovich, F. Matteocci, L. Cinà, A. D. Carlo, and C. Ducati, "In situ observation of heat-induced degradation of perovskite solar cells," *Nature Energy*, vol. 1, 2016.

[15] S. W. Lee, S. Kim, S. Bae, K. Cho, T. Chung, L. E. Mundt, S. Lee, S. Park, H. Park, M. C. Schubert, S. W. Glunz, Y. Ko, Y. Jun, Y. Kang, H. S. Lee, and D. Kim, "Uv degradation and recovery of perovskite solar cells," *Scientific Reports*, vol. 6, pp. 1–10, 2016.

[16] D. Wang, M. Wright, N. K. Elumalai, and A. Uddin, "Stability of perovskite solar cells," *Solar Energy Materials and Solar Cells*, vol. 147, pp. 255–275, 2016.

[17] M. Saliba, T. Matsui, J. Y. Seo, K. Domanski, J. P. Correa-Baena, M. K. Nazeeruddin, S. M. Zakeeruddin, W. Tress, A. Abate, A. Hagfeldt, and M. Grätzel, "Cesium-containing triple cation perovskite solar cells: Improved stability, reproducibility and high efficiency," *Energy and Environmental Science*, vol. 9, pp. 1989–1997, 2016.

[18] D. B. Straus, S. Guo, A. M. Abeykoon, and R. J. Cava, "Understanding the instability of the halide perovskite cspbi3 through temperature-dependent structural analysis," *Advanced Materials*, vol. 32, pp. 1–8, 2020.

[19] S. Mariotti, O. S. Hutter, L. J. Phillips, P. J. Yates, B. Kundu, and K. Durose, "Stability and performance of cspbi2br thin films and solar cell devices," *ACS Applied Materials and Interfaces*, vol. 10, pp. 3750–3760, 2018.

[20] Q. Ma, S. Huang, X. Wen, M. A. Green, and A. W. Ho-Baillie, "Hole transport layer free inorganic cspbibr2 perovskite solar cell by dual source thermal evaporation," *Advanced Energy Materials*, vol. 6, pp. 2–6, 2016.

[21] W. Shockley and H. J. Queisser, "Detailed balance limit of efficiency of p-n junction solar cells," *Journal of Applied Physics*, vol. 32, pp. 510–519, 3 1961.

[22] W. Zhu, Z. Zhang, W. Chai, Q. Zhang, D. Chen, Z. Lin, J. Chang, J. Zhang, C. Zhang, and Y. Hao, "Band alignment engineering towards high efficiency carbon-based inorganic planar cspbibr2 perovskite solar cells," *ChemSusChem*, vol. 12, pp. 2318–2325, 2019.

[23] Y. Guo, X. Yin, J. Liu, S. Wen, Y. Wu, and W. Que, "Inorganic cspbibr2-based perovskite solar cells: Fabrication technique modification and efficiency improvement," *Solar RRL*, vol. 3, pp. 1–13, 2019.

[24] M. Jošt, L. Kegelmann, L. Korte, and S. Albrecht, "Monolithic perovskite tandem solar cells: A review of the present status and advanced characterization methods toward 30% efficiency," *Advanced Energy Materials*, vol. 10, 2020.

[25] PV Magazine, "Oxford pv retakes tandem cell efficiency record," 2020.

[26] B. Zhang, W. Bi, Y. Wu, C. Chen, H. Li, Z. Song, Q. Dai, L. Xu, and H. Song, "High-performance cspbibr2 perovskite solar cells: Effectively promoted crystal growth by antisolvent and organic ion strategies," *ACS Applied Materials and Interfaces*, vol. 11, pp. 33868–33878, 2019.

[27] W. Zhang, Z. Zhang, Q. Jiang, Z. Wei, Y. Zhang, and H. You, "Charge-transporting-layer-free, all-inorganic cspbibr 2 perovskite solar cells via dipoles-adjusted interface," *Nanomaterials*, 2020.

[28] W. Li, M. U. Rothmann, A. Liu, Z. Wang, Y. Zhang, A. R. Pascoe, J. Lu, L. Jiang, Y. Chen, F. Huang, Y. Peng, Q. Bao, J. Etheridge, U. Bach, and Y. B. Cheng, "Phase segregation enhanced ion movement in efficient inorganic cspbibr2 solar cells," *Advanced Energy Materials*, vol. 7, pp. 1–8, 2017.

[29] C. F. J. Lau, X. Deng, Q. Ma, J. Zheng, J. S. Yun, M. A. Green, S. Huang, and A. W. Ho-Baillie, "Cspbibr2 perovskite solar cell by spray-assisted deposition," *ACS Energy Letters*, vol. 1, pp. 573–577, 9 2016.

[30] J. Liang, Z. Liu, L. Qiu, Z. Hawash, L. Meng, Z. Wu, Y. Jiang, L. K. Ono, and Y. Qi, "Enhancing optical, electronic, crystalline, and morphological properties of cesium lead halide by mn substitution for high-stability all-inorganic perovskite solar cells with carbon electrodes," *Advanced Energy Materials*, vol. 8, pp. 1–7, 2018.

[31] J. V. Patil, S. S. Mali, and C. K. Hong, "A-site rubidium cation-incorporated cspbi2br all-inorganic perovskite solar cells exceeding 17*Solar RRL*, vol. 4, pp. 1–9, 2020.

[32] Y. Guo, F. Zhao, J. Tao, J. Jiang, J. Zhang, J. Yang, Z. Hu, and J. Chu, "Efficient and hole-transporting-layer-free cspbi 2 br planar heterojunction perovskite solar cells through rubidium passivation," *ChemSusChem*, vol. 12, pp. 983–989, 2019.

[33] Y. Li, J. Duan, H. Yuan, Y. Zhao, B. He, and Q. Tang, "Lattice modulation of alkali metal cations doped $cs_{1-x}r_x$pbbr3 halides for inorganic perovskite solar cells," *Solar RRL*, vol. 2, pp. 1–8, 2018.

[34] G. E. Eperon, G. M. Paternò, R. J. Sutton, A. Zampetti, A. A. Haghighirad, F. Cacialli, and H. J. Snaith, "Inorganic caesium lead iodide perovskite solar cells," *Journal of Materials Chemistry A*, vol. 3, pp. 19688–19695, 2015.

2.1.7 Supplementary Materials

Inorganic-Perovskites: Improved Film and Crystal Quality of CsPbIBr$_2$ when Doped with Rubidium

Alexander W. Stewart[a], Amal Bouich[a,b], Bernabé Marí Soucase[a]

[a] Institut de Disseny i Fabricació, Universitat Politècnica de València,
Camí de Vera, València, Spain 46022
[b] Laboratory (LMEE), University of Ibn Tofail Av. de L'Université,
Kenitra, Morocco BP 242

Corresponding author email: Bouich.amal@gmail.com

Table 1. Equations and Expressions used for figure 2 and 5 in manuscript.

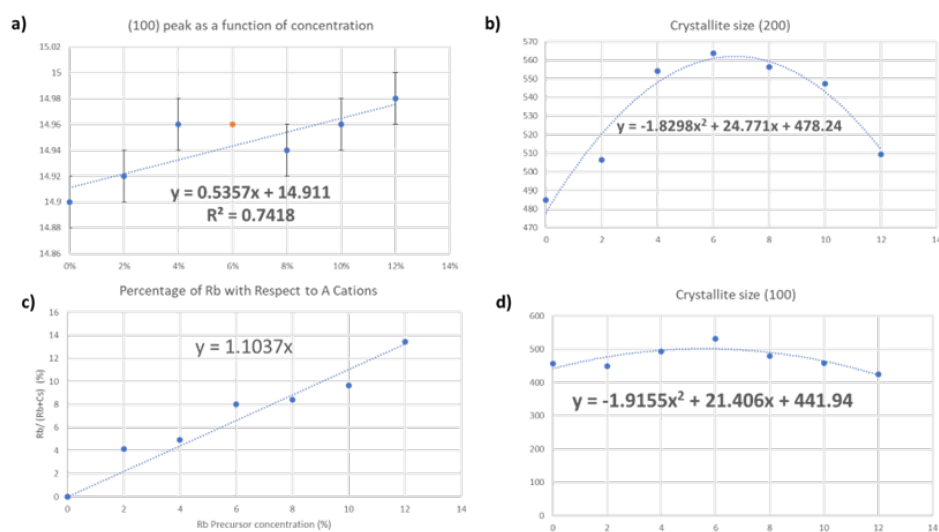| Equation	$y = a + b \cdot x$	
Plot	PL Primary Pe	Tauc Plot
Weight	No Weighting	
Intercept	2.09779 ± 0.0	2.09786 ± 0.0
Slope	0.00261 ± 5.0	0.00321 ± 5.7
Residual Sum of	1.44429E-4	1.85714E-4
Pearson's r	0.91681	0.92828
R-Square (COD	0.84054	0.8617
Adj. R-Square	0.80864	0.83404

Figure S1: (a) (100) peak as a function of concentration with fitting equation (b) Crystallite size (200) with fitting equation (c) Percentage of Rubidium with respect to Cesium (d) Crystallite size (100) with fitting equation.
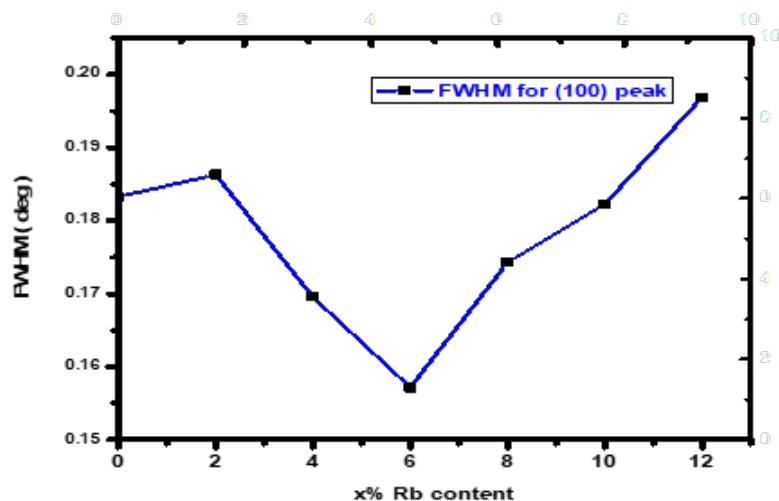
Figure S2: FWHM of the characteristic peak (100) for $Cs_{1-x}Rb_xPbIBr_2$, where x = 0%, 2%, 4%, 6%, 8%, 10% and 12% thin film.
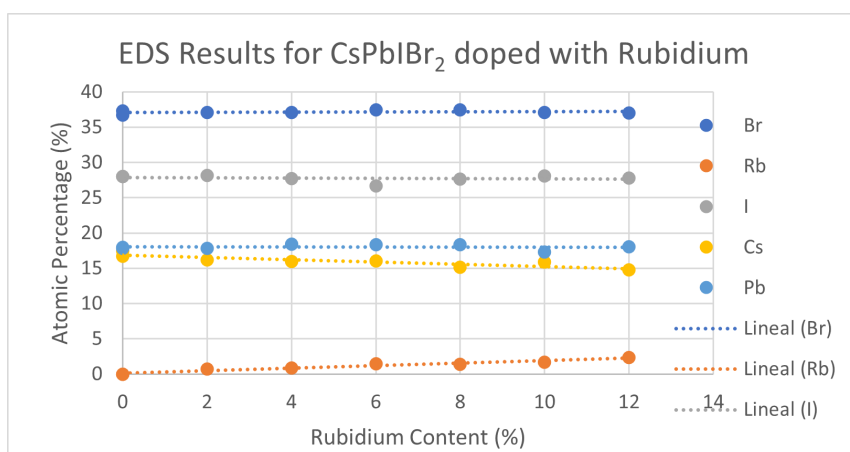

Figure S3: EDS Results for $CsPbIBr_2$ pure and doped with x% Rubidium where x = 0%, 2%, 4%, 6%, 8%, 10% and 12% thin film.

77

2.2 Enhancing the stability and crystallinity of CsPbIBr$_2$ through antisolvent engineering

Enhancing the stability and crystallinity of CsPbIBr$_2$ through antisolvent engineering

Alexander W. Stewart[1,*] , Amal Bouich[1], and Bernabé Marí Soucase[1]

[1] Institut de Disseny I Fabricació, Universitat Politècnica de València, Camí de Vera, 46022 València, Spain

ABSTRACT

All inorganic lead-based perovskites containing bromine-iodine alloys, such as CsPbIBr$_2$, have arisen as one of the most attractive candidates for absorber layers in solar cells. That said, there remains a large gap when it comes to film and crystal quality between the inorganic and hybrid perovskites. In this work, antisolvent engineering is employed as a simple and reproducible method for improving CsPbIBr$_2$ thin films. We found that both the antisolvent used and the conditions under which it was applied have a measurable impact on both the quality and stability of the final product. We arrived at this conclusion by characterising the samples using scanning electron microscopy, X-ray diffraction, UV–visible and photoluminescence measurements, as well as employing a novel system to quantify stability. Our findings, and the application of our novel method for quantifying stability, demonstrate the ability to significantly enhance CsPbIBr$_2$ samples, produced via a static one-step spin coating method, by applying isopropanol 10 s after commencing the spin programme. The antisolvent quenched CsPbIBr$_2$ films demonstrate both improved crystallinity and an extended lifespan.

Introduction

The Paris Agreement identified the development of solar power as a key to tackling climate change. Perovskites have emerged as a prime candidate for solar cells due to their low cost [1], impressive rise in power conversion efficiency (PCE) [2], and excellent optoelectronic properties [3–8]. Perovskites are crystal structures with the composition ABX$_3$, where A and B are cations and X is an anion. The A-site can be occupied by organic molecules, such as MA [9], FA [10], and GA [11], or inorganic ones, such as caesium, giving rise to hybrid- and all-inorganic perovskites, respectively. The B-site cation is the most often occupied by lead, however, due to its toxic nature, tin-based perovskites have also been explored [12]. The anion site is occupied by a halide such as iodine, bromine, or chlorine. Since several different elements or molecules can occupy a given cation [10, 11, 13] or

Springer

Enhancing the stability and crystallinity of CsPbIBr$_2$ through antisolvent engineering

Alexander W. Stewart, Amal Bouich Bernabé Marí Soucase

Institut de Disseny i Fabricació, Universitat Politècnica de València, Camí de Vera, València, Spain 46022

Corresponding author email: alste5@doctor.upv.es

Abstract:

All inorganic lead-based perovskites containing bromine-iodine alloys, such as $CsPbIBr_2$, have arisen as one of the most attractive candidates for absorber layers in solar cells. That said, there remains a large gap when it comes to film and crystal quality between the inorganic and hybrid perovskites. In this work, antisolvent engineering is employed as a simple and reproducible method for improving $CsPbIBr_2$ thin films. We found that both the antisolvent used and the conditions under which it was applied have a measurable impact on both the quality and stability of the final product. We arrived at this conclusion by characterising the samples using scanning electron microscopy, x-ray diffraction, UV-visible and photo-luminescence measurements, as well as employing a novel system to quantify stability. Carrying out a simulation using the measured experimental values, we obtained a power conversion efficiency of 13.7% for a single junction $CsPbIBr_2$-based solar cell. Our findings, and the application of our novel method for quantifying stability, demonstrates the ability to significantly enhance $CsPbIBr_2$ samples, produced via a static one-step spin coating method, by applying isopropanol 10 seconds after commencing the spin programme. The antisolvent quenched $CsPbIBr_2$ films demonstrate both improved crystallinity and an extended life-span.

Keywords: $CsPbIBr_2$, Antisolvent, stability, thin-films, solar cells

2.2.1 Introduction

The Paris Agreement identified the development of solar power as key to tackling climate change. Perovskites have emerged as a prime candidate for solar cells due to their low cost [1], impressive rise in power conversion efficiency (PCE) [2], and excellent optoelectronic properties [3–8]. Perovskites are crystal structures with the composition ABX_3, where A and B are cations and X is an anion. The A site can be occupied by organic molecules, such as MA [9], FA [10], and GA [11], or inorganic ones, such as caesium, giving rise to hybrid- and all inorganic perovskites, respectively. The B site cation is most often occupied by lead, however due to its toxic nature tin based perovskites have also been explored [12]. The anion site is occupied by a halide such as iodine, bromine or chlorine. Since several different elements or molecules can occupy a given cation [10, 11, 13] or halide site [14, 15], many combinations are known to exist. Perovskites have low stability when compared to silicon, notably in the presence of humidity [9], but other factors have been shown to cause or catalyse degradation [16–20]. While inorganic perovskites have shown superior levels of stability [15, 21–24], there is still a need to extend their lifespans if they are to compete with silicon-based solar cells.

Of the inorganic mixed halide perovskites, $CsPbIBr_2$ offers the optimum trade-off between stability and bandgap since bromine content is proportional to both. $CsPbIBr_2$ is especially well suited for use in tandem or multilayer devices due to it relatively wide bandgap of 2.05eV [25, 26]. One of the limitations of $CsPbIBr_2$-based devices is that their maximum PCE is just over 11% [27], which is around half of the materials Shockley-Quessier limit, and at a more fundamental level, some of the best $CsPbIBr_2$ films reported in the literature have a high number of pin-holes [22, 23, 25, 28, 29]. These limitations highlight the existence of a research gap. To date, the solutions explored include: surface passivation [30], Cl^- doping [31], antisolvent-quenching [30], light soaking [28], intermolecular exchange [23], precursor solution ageing [32], bandgap alignment [31], and doping with Rb^+ and Mn^{2+} [21, 33]. Moreover, $CsPbIBr_2$ films have been deposited via: one-step spin-coating [30, 32, 34], a gas-assisted method [35], a spray-assisted method [25], a two-step spin coating method [21] and by dual-source thermal evaporation [15]. While antisolvent-quenching has been shown to significantly improve a range of perovskite materials [36–39], we were surprised to note a lack of literature reporting its use with $CsPbIBr_2$, with Liu et al. reporting its use in a vapour-assisted deposition [40] and only Zhang et al. reporting the use of antisolvents with a one-step spin coating procedure. In their paper, they applied six different antisolvents 20 seconds after commencing the spin-programme, finding diethyl ether to give the best results. Therefore, it is essential not only to confirm the results of Zhang et al.'s study and to expand upon them, but also to establish antisolvent quenching

as a trusted and simple method for improving CsPbIBr$_2$.

Here, an antisolvent quenching method is reported which improves both crystal quality and extends the lifespan of CsPbIBr$_2$ thin films. An antisolvent is a solvent which cannot dissolve the components of a solution, in our case, the perovskite. The application of the antisolvent creates local regions of supersaturation, leading to accelerated heterogeneous nucleation [38]. It is by optimizing the rate of nucleation and crystal growth that a higher quality film is obtained. In general, when antisolvents are used, the concentration is kept within the "seeding zone" which is above the solubility curve but below the metastable limit. Concentrations in these ranges lead to the growth of already existent nuclei, or "seeds", but do not cause the creation of new ones.

During our review of the literature, we found ourselves asking: could there be more factors that contribute to the quality of anti-solvent quenched CsPbIBr$_2$? If so, to what extent do different factors affect the measurable properties of CsPbIBr$_2$? We identified two variables that likely affect the antisolvent quenching method: the antisolvent used and the time at which the antisolvent is applied during the programme (sometimes called dripping time). Following this, we formed the hypothesis that both antisolvent selection and application conditions would have an impact on the final sample. To test this, an experiment was designed where both antisolvent and dripping time were varied, and then the impact that it had on the properties and stability of CsPbIBr$_2$ was measured. We expected, due to Zhang et al.'s paper, that we would find diethyl ether to be the best antisolvent, however this turned out not to be the case. Moreover, we found the optimization of the dripping time to be a necessary step to maximize the effectiveness of the method.

2.2.2 Methodology

Materials

The precursor chemicals, namely caesium iodide (CsI) and lead bromide (PbBr$_2$), were purchased from Tokyo Chemical Industry. The solvents dimethyl sulfoxide (DMSO 99.9%), isopropanol (IPA), diethyl ether (DEE), toluene (Tl) and chlorobenzene (ClBn) were all purchased from Sigma Aldrich and were used as received. Film synthesis

First, fluorine-doped tin oxide (FTO) glass substrates were cleaned for 15 minutes in detergent, ethanol, acetone, and isopropanol, before being dried in a stream of compressed air. The substrates were treated by UV-Ozone for 15 minutes to remove any further impurities and to improve the surface wetness. The substrates were then transported into an inert argon-atmosphere, where the samples were prepared and stored until use. A 1M solution of CsPbIBr$_2$ was prepared by dissolving equimolar ratios of CsI and PbBr$_2$ in

DMSO at 85°C for 90 minutes. Once the solution was ready, 50µL of yellow perovskite solution was statically spin-coated at 4000RPM for 50 seconds. 100µL of antisolvent was applied after a given time had elapsed from the initiation of the spin programme (referred to as the dripping time). Samples were annealed for 5 minutes at 50°C, during the course of which they changed to an orange-red. This initial colour change, signalling the formation of the perovskite structure occurring, happens because relatively little energy is required for caesium to begin intercalating between the $PbBr_2$, due to its small ionic radius of 1.81 Å [41]. Samples are then heated slowly, avoiding thermal shocks, to 250°C and held at this temperature for 5 minutes, removing any remaining solvent. During this stage of the annealing the samples take on a dark-red appearance, confirming the complete formation of the desired perovskite phase. Fig. 1 shows the procedure for synthesizing the $CsPbIBr_2$ films.
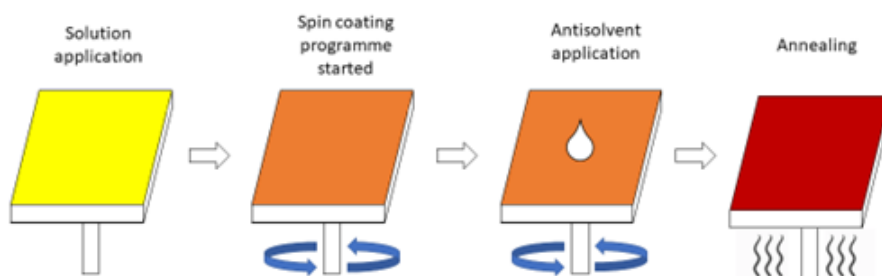

Figure 1: The $CsPbIBr_2$ solution that is applied to the substrate is yellow to begin with. The solution is spin-coated whilst the antisolvent is applied. The samples are then annealed during which a significant colour change takes place as the solution dries and the perovskite structure is formed.

Characterization techniques

Thin films of $CsPbIBr_2$ were characterized by X-ray diffraction (XRD) using the RIGAKU Ultima IV with Cu kα radiation ($\lambda = 1.5418$ Å). Surface morphology was studied using the field emission scanning electron microscope (FESEM) within the Zeiss Auriga Compact with an applied voltage of 1.5 kV. The FESEM was equipped with a focused ion beam (FIB) which was used to make an incision in the surface and measure the film thickness. The Zeiss Auriga Compact was also equipped with the apparatus necessary to carry out electron dispersive spectroscopy (EDS), allowing the atomic proportions of the films to be determined. Optical properties were analysed with an Ocean Optics HR4000 spectrophotometer and photoluminescence

(PL) emission was driven by a semiconductor laser with a wavelength of λ = 405 nm.

Experiment structure

A reference sample with no antisolvent was made along with four other samples where Tl, IPA, DEE and ClBn was used. The dripping time for all samples was 8 seconds. These samples were characterized by XRD, UV-vis, PL, FESEM and EDS. In the second stage of the experiment, the dripping time of the best sample, IPA, was changed to 5, 10, 15 and 20 seconds, respectively. The samples were then characterised by XRD, UV-vis, PL, and FESEM. In the final stage of the experiment, stability was quantified in terms of XRD and UV-vis spectra when the samples were 5 weeks old. For this degradation study, all the samples used in the antisolvent selection and dripping time investigation were stored in the laboratory, at 23°C and with a relative humidity of 20%, for 5 weeks. These conditions were measured daily and only small fluctuations in temperature ±2°C were seen to take place. The relative humidity remained constant throughout the experiment except for a few days when it increased to 40% due to heavy precipitation outside. All samples where exposed to the same conditions allowing for a fair comparison between them.

2.2.3 Results

The results section is broken down into four parts: the antisolvent selection, the effect of dripping time, the impact on stability, and then several solar cells are simulated using the parameters of the optimized $CsPbIBr_2$ film.

Antisolvent selection

To determine the effect of antisolvent selection on samples of $CsPbIBr_2$, four different antisolvents were applied under identical conditions, as described in the previous section. These samples were compared with a reference sample that had no antisolvent applied.

Once the XRD spectra of the fresh samples had been collected, a Rietveld refinement was carried out to determine the crystal structure. We found the same parameters as other authors, namely a cubic structure, pertaining to the PM-3M space group, with a lattice constant of 5.93423 ± 0.00034 Å [42, 43]4. All samples showed two major diffraction peaks, corresponding to the (100) and (200) planes, at 15° and 30° respectively. Smaller peaks found at 21°, 26° and 37° correspond to the (110), (111) and (211) planes. The calculated Miller indices can be found below in Table 2. These results are based upon an analysis of the reference sample, in which the fit obtained with the refinement was highly precise with the RWP and RP values being 7.1% and 4.72%, respectively. Rietveld refinements were not carried out

for all the samples since their spectra were highly similar, differing only in intensity, meaning that they were unlikely to generate different results.

Table 2.2: Reported experimental values for PSCs with TiO$_2$/perovskite/spiro-OMeTAD architectures. The PCE of cells in this work correspond to those where the optimal doping level was implemented in the perovskite.

h	k	l	2θ	Intensity(%)
1	0	0	14.9108	47.834
1	1	0	21.1475	2.226
1	1	1	25.9754	0.026
2	0	0	30.0819	100
2	1	0	33.7327	0.135
2	1	1	37.0638	3.907
2	2	0	43.0617	3.223

When comparing the diffraction intensity, the sample in which IPA was used showed an almost two-fold increase when compared to the reference sample, shown in Fig. 2 (a) and (b), implying a major increase in the diffraction planes associated with the perovskite structure. The area under the diffraction peaks, which corresponds roughly to the quantity of perovskite material present, gave similar results. The rest of the samples showed a decrease in peak intensity, implying a worsening of the crystal structure as a result of the antisolvent application.

The broadening of diffraction peaks is known to be related to the size of the diffraction regions in crystals. Employing the Scherrer equation, it is possible to calculate the crystallite size based on the full-width at half-maximum (FWHM). It should be noted that although the terms "crystallite" and "grain" are often used interchangeably, there are several definitions for the term crystallite. In our case, we define a crystallite as a region in which all the material is orientated in a particular diffractive direction. This is important because it means that a grain can be composed of several crystallites. For this reason, the grains observed using the FESEM may not always coincide with the crystallite sizes calculated from XRD measurements.

In Fig. 2 (c) it is possible to see that the application of IPA leads to a significant increase in crystallite sizes from around 45nm in the reference sample to around 55nm which could be due to an increased period within the metastable zone and in turn a prolonged period of crystal growth. This increase in crystallite size is important because crystallite and grain boundaries can contribute to charge recombinations. Since an increase in size
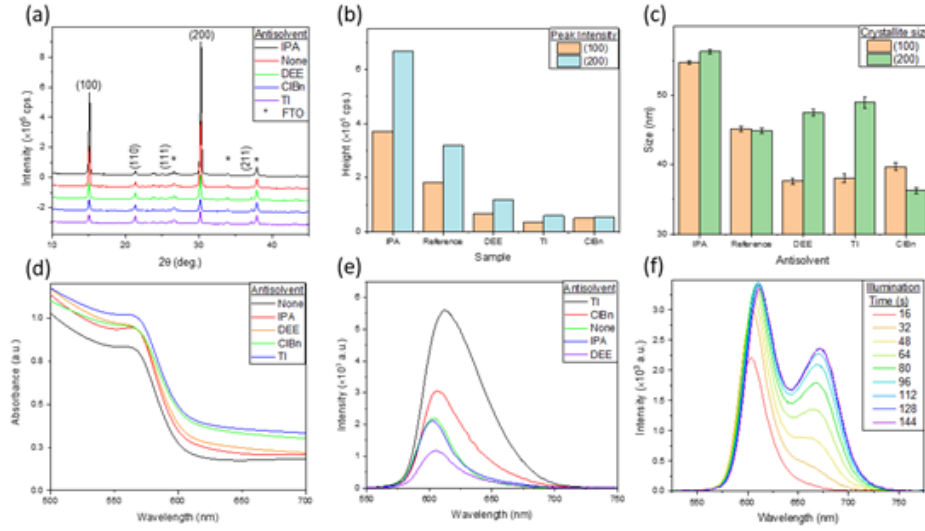
Figure 2: A summary of the results collected for the antisolvent selection. The antisolvents used were IPA, DEE, Tl and ClBn. These results are compared with a reference sample with no antisolvent. (a) XRD spectra of the samples (b) peak intensity corresponding to the two main diffraction planes (c) crystallite size (d) absorbance spectra (e) photoluminescence spectra with an integration time of 16 seconds (f) time evolution of the PL spectra of the reference sample.

implies a reduction in the number of these boundaries, this film should yield a higher PCE. Interestingly, while the IPA, the reference, and the ClBn samples had comparable crystallite sizes for both the (100) and (200) diffraction peaks, the other samples showed a divergence, meaning that crystallite sizes in the material were non-uniform.

To characterise the optical properties of the samples, measurements of absorbance and photoluminescence were made. The absorption onset of the samples took place around 600nm, which agrees with the accepted bandgap value [15, 25, 31, 43]. All samples showed a higher absorbance than the reference sample, with the IPA and DEE samples giving similar results. While ClBn and Tl seems to have increased the absorbance of the samples, they also demonstrate a shallower climb in absorbance, potentially signalling the existence of interband defects. While absorbance measurements are a key tool for understanding the band structure and crystal quality, it should also be noted that the absorption coefficient gives more information, since it is also a function of thickness and reflectivity. Any deviations in thickness will create an associated error in the absorbance measurement. This limits our ability to identify the superior sample based solely on its absorbance spectrum. On the other hand, all samples show an increase in absorbance

at the accepted wavelength value for the $CsPbIBr_2$ bandgap signalling that the material has been correctly formed.

As can be seen in Fig. 2 (f), measurement of the PL spectra revealed that all samples showed a time dependent spectrum when under illumination, leading to the apparition of a lower energy peak. Moreover, a given spectrum would "reset" if the sample were stored in dark conditions. These observations are consistent with observations made by other authors and with the so called "Hoke Effect" [44–46]. While more detailed explanations can be found in the paper by Hoke et al., the evolution of a PL spectra in a mixed halide perovskite under illumination can be explained by the segregation of different halide phases causing iodine rich regions to be formed, which in turn are responsible for the lower energy emission.

PL measurements carried out when the sample is initially illuminated, shown in Fig. 2 (e), give a peak in emission at around 610nm, which agrees with the established bandgap value of $CsPbIBr_2$ [15, 25, 31, 43]. All samples show a low energy tail, probably the initial signs of the Hoke Effect. The sample in which Tl was applied gave the highest emission, which is the same result as was found by Zhang et al. The IPA and the reference sample gave very similar PL spectra, suggesting that the antisolvent had a small effect on the band structure.

Fig. 3 shows the FESEM images that were taken of the surface. Both the ClBn and Tl samples were non-uniform and had large-scale defects compared with the DEE, IPA and reference samples which showed smooth and uniform surfaces. When magnified 20,000 times, all samples showed pin-hole free regions, demonstrating that film coverage at higher magnifications can be misleading. In general, the DEE, IPA and reference samples were difficult to distinguish, however the reference sample had slightly fewer defined grains. From the FESEM images alone, it was difficult to distinguish the best sample however ClBn and Tl clearly had a negative effect on surface homogeneity.
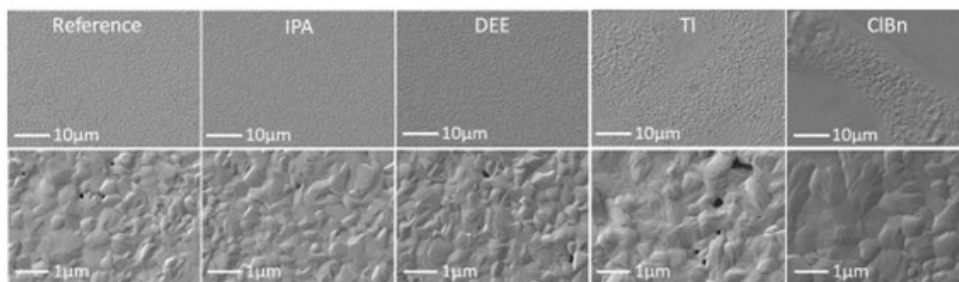

Figure 3: FESEM images taken of $CsPbIBr_2$, with different antisolvents applied, at magnifications of 2,000- and 20,000-times with an accelerating potential of 1.5keV. Each sample has a large-scale image (above) and a magnified image (below) to see the grain structure.

EDS was carried out in the FESEM by increasing the accelerating potential to 15keV. Table 1 summarises the results. All the EDS spectra gave the correct atomic percentages for the composition $CsPbIBr_2$. The samples showed a slight surplus of iodine and a deficit of bromine; this is beneficial since a higher iodine content will lower the bandgap and lead to an increased Shockley-Quessier limit. Using the FIB inside the FESEM chamber, an incision was made in the surface of the samples and their thickness was measured. The mean value for thickness was 296nm with a standard deviation of 28nm.

Table 2.3: The atomic percentages of the freshly deposited $CsPbIBr_2$ samples using no antisolvent, IPA, DEE, ClBn and Tl.

Element at. (%)	Reference	IPA	DEE	ClBn	Tl
Br	37.7	37.6	38.5	37.4	37.5
I	24.1	22.8	23.8	25.4	23.1
Cs	19.5	20.2	18.5	18.6	20.5
Pb	18.7	19.4	19.2	18.6	18.9

Dripping time

To ascertain the effect, if any, that the dripping time would have on the finished sample, four samples of $CsPbIBr_2$ were treated with IPA as an antisolvent. IPA was chosen out of the antisolvents as it gave the best results all-round, especially in terms of XRD. The dripping time was increased in steps of five seconds due to the difficulty in carrying out precise time-wise application of antisolvents by hand.

The FESEM revealed that $CsPbIBr_2$ samples treated with IPA over a range of different dripping times, from 5s to 20s, were difficult to distinguish at magnifications of around 2,000 times. However, at very low magnifications of around 24 times, the 5 and 20 second samples showed nonuniformity. Specifically, the 5 second sample showed a patchy structure which could be due to the solution not having enough time to spread out before the antisolvent application. On the other hand, the 20 seconds sample showed large agglomerations of perovskite material sitting on top of the surface. In Fig. 4 it is possible to see that although the 5 second sample was nonuniform, it had regions with good grain formation at higher magnifications. This shows that often several images are needed to characterise the nature of the surface. The other samples showed increased film coverage, with the 10 second sample having the best-defined grains and the fewest pinholes.
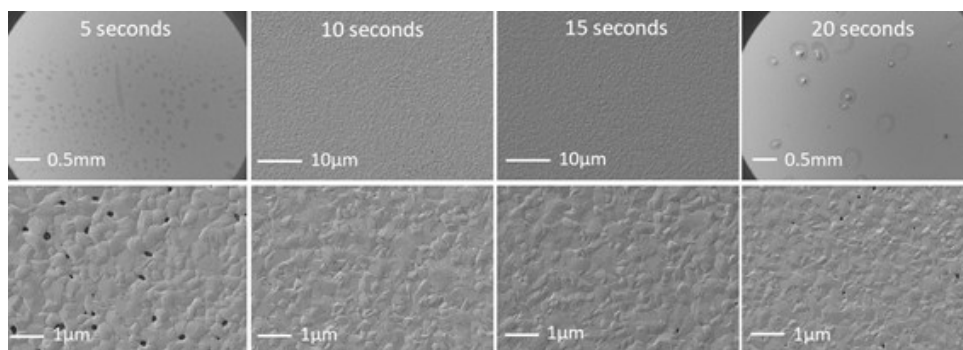
Figure 4: FESEM images of CsPbIBr$_2$ thin films treated with IPA over a range of different dripping times, taken at magnifications of 2,000- and 20,000-times with an accelerating potential of 1.5keV. Each sample has a large-scale image (above) and a magnified image (below) to see the grain structure.

In contrast to the FESEM analysis, the XRD results revealed the 10 seconds sample to the be the best one, since it had an intensity far superior to any other. In fact, in Fig. 5 (b) we can see that there seems to be a parabolic relationship between the dripping time and the peak intensity. This parabola takes a maximum, for both the (100) and (200) planes, at around 11 seconds. Also shown in this graph is the intensity given by the reference sample. The fact that all samples where IPA was used showed greater intensity than the reference samples supports the claim that the method is both reproducible and effective.

In terms of optical properties, the absorbance spectra were all similar, with the reference sample having an absorbance centred between the most and the least absorbent samples. The sample with IPA applied after 8 seconds showed the highest absorbance followed by the 10 second sample. The samples where antisolvent was applied after 15 and 20 seconds showed the lowest absorbance. As mentioned in the previous section, the error associated with the sample thickness should be considered when analysing the absorbance measurements since thicker layers will have a higher absorbance. On the other hand, the absorption onset is independent of thickness and agrees with those found in the literature [15, 25, 31, 43].

The PL spectra once again showed sign of the Hoke Effect taking place, as in Fig. 2 (f), meaning that there was a generic shift to lower energies and the apparition of a new PL peak. The effect could also explain the low energy tail seen in Fig. 5 (d). The fact that there may be two variables at play, the Hoke Effect and drip time, makes it difficult to confirm the observed small displacements in the peak maxima. However, a clear trend
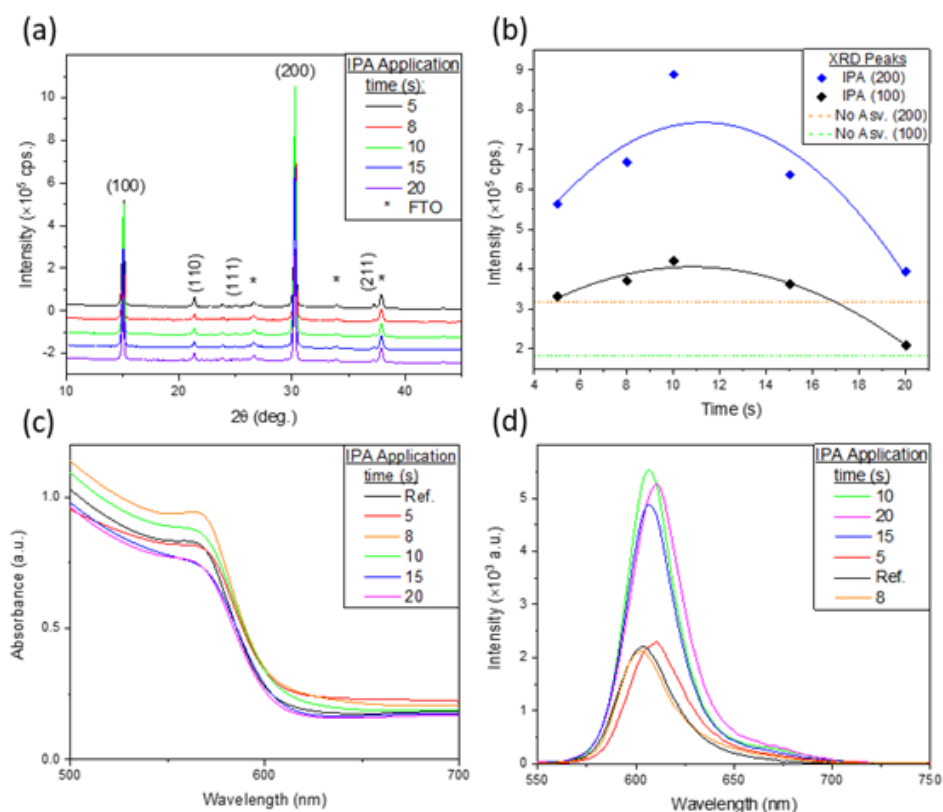
Figure 5: A summary of the results collected from varying the dripping time of IPA. (a) XRD spectra of the freshly prepared samples (b) intensity of the (100) and (200) peaks compared with the reference sample (c) absorbance spectra (d) PL spectra with an integration time of 16 seconds.

can be seen where samples that had a dripping time higher than 8 seconds exhibit more than a two-fold increase in emission. This could be a result of improved crystal structure, and an associated reduction of non-radiative defects.

Stability study

To quantify the stability of the samples, an XRD analysis was carried out on all the samples used in the previous sections after they were stored for 5 weeks in the laboratory in low-light conditions, at a temperature of 23°C and relative humidity of 20%.

Since there is no generally accepted procedure for measuring the stability of perovskites, a simple method was devised to quantify it. Since XRD
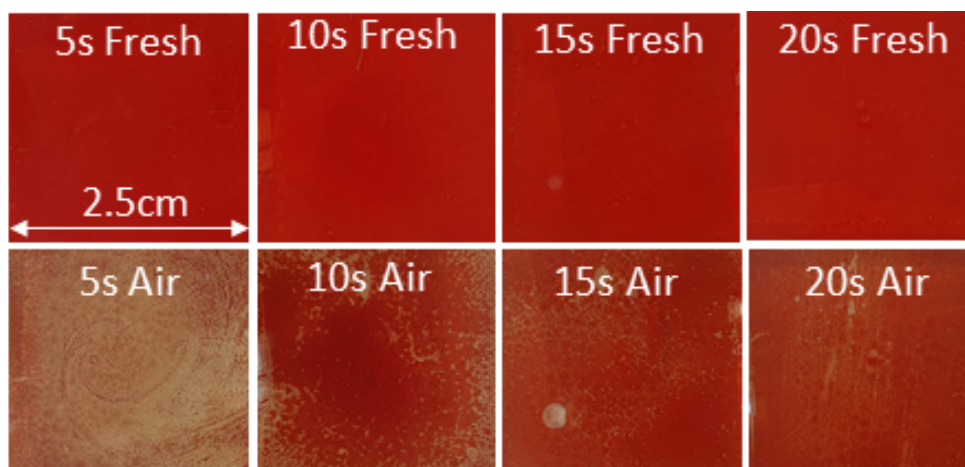
Figure 6: Photographs taken of the freshly prepared samples and the 5-week-old samples after they had been stored in the laboratory.

spectra generate some of the most easily quantifiable results, a method was developed which compared values of intensity. That said, values derived from area could also be used. Assuming significant changes do not occur in the aged spectra compared with their corresponding fresh spectra, such as the apparition of new peaks, it should be possible to correlate a percentage decrease in intensity with stability, since the number of perovskite diffractive planes is proportional to total intensity. This is because any new peaks not found in Table 1 correspond to new phases and demonstrate the partial degradation of the $CsPbIBr_2$ alloy.

By exploiting the correlation between XRD intensity and stability, we can quantify the stability of a sample by calculating the percentage decrease in its diffraction maxima. The 10 and 15 second samples showed greatly increased stability, up to 65% for the IPA samples in comparison with the 20% that the reference sample gave. Remarkably, the intensity of the aged 10 and 15 second samples are higher than the freshly prepared reference $CsPbIBr_2$ samples. These results suggest that IPA not only improves crystal quality but also stability. Contrastingly, the worst performing sample in terms of percentage decrease was the one where IPA was applied after 5 seconds. Many new diffraction peaks can also be seen to arise in Fig. 7 (b). It is likely that the solution did not have enough time to spread out before the antisolvent was applied, leading to inhomogeneous film thickness and crystal nucleation. Moreover, this would explain the patchy structure observed in Fig. 4 and the spiral structure seen in Fig. 6.

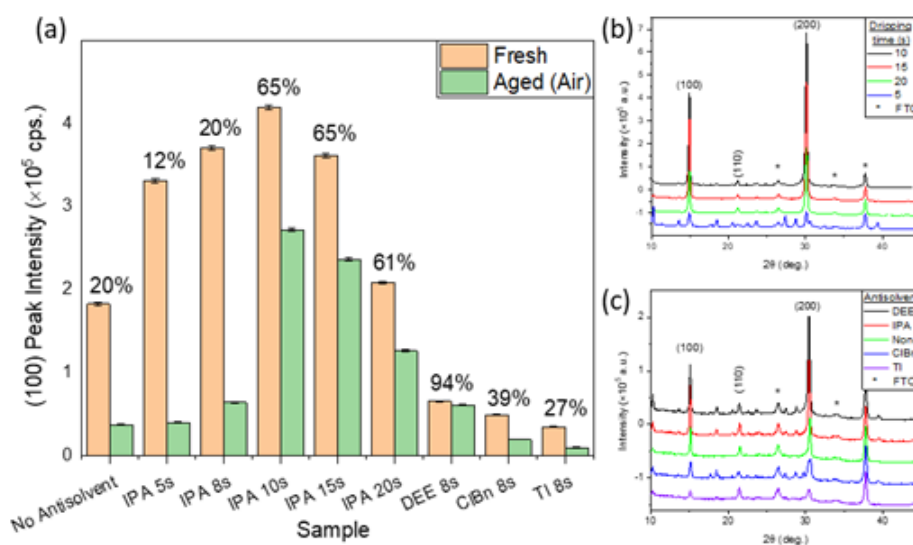Applying this method to measure the stability of the samples treated

Figure 7: Stability measurement based on XRD spectra taken when the samples were freshly prepared and after they were aged in the laboratory. (a) peak intensity for all the samples mentioned in this work before and after they were aged. The percentage decrease corresponds to the difference between the freshly prepared samples (orange) and the aged samples (green). (b) XRD spectra of aged samples from the dripping time investigation (c) XRD spectra of the aged samples from the antisolvent selection.

with different antisolvents, the CsPbIBr$_2$ sample treated with DEE stands out as having extraordinarily high stability in terms of percentage decrease. However, this is misleading, since one can see the apparition of many new peaks in the spectrum in Fig. 7 (c) showing that parts of the structure had degraded into new phases. Similarly, ClBn and Tl would seem to have increased the stability of the samples, however closer inspection in Fig. 7 (c) reveals that the only sample to have not given rise to new peaks is the reference sample. Seen in this way, not only does the application of these antisolvents seem to adversely affect their properties when fresh, but it also accelerates their degradation into new phases.

The sample where IPA was applied after 8 seconds showed a 20% decrease in intensity and the apparition of new peaks. Due to this phase change occurring, which did not take place in the reference sample, it is possible that 8 seconds is not a long enough amount of time for the solvent to spread out, which is why all the samples carried out at with this time show accelerated degradation.

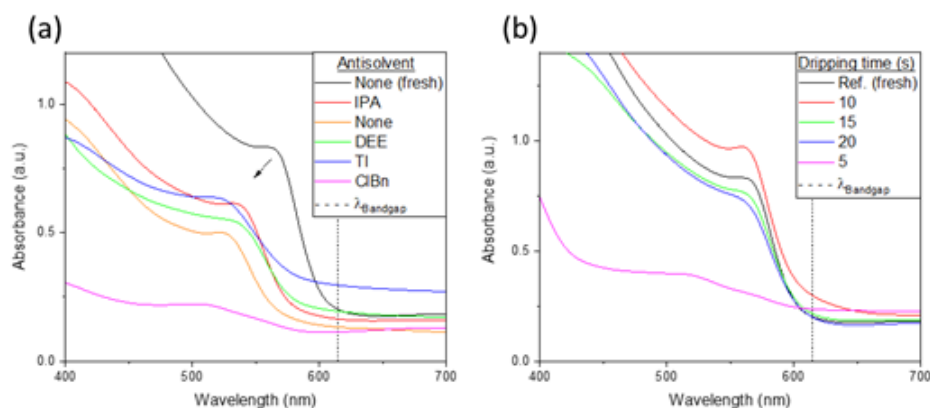In terms of absorbance (Fig. 8) all samples show a generic shift to lower

Figure 8: Absorbance spectra of the fresh and 5-week-old CsPbIBr$_2$ samples stored in the laboratory at 23°C and RH=20% under low-light conditions (a) Absorbance spectra of aged samples shown in Fig. 2 (b) absorbance spectra of aged samples shown in Fig. 5. The dotted lines show the bandgap value of the desired phase [25, 31, 34].

wavelengths, caused by the transformation of the desired phase, which is metastable at room temperature, into the stable one which has a larger bandgap value. The temperature at which this phase transition occurs in inorganic caesium-based perovskites depends on bromine-iodine content. For CsPbI$_3$ and CsPbBr$_3$ the phase transition occurs at 310°C [47] and 130°C [48] respectively, it follows that for CsPbIBr$_2$ it would fall somewhere between the two.

Comparing the absorbance spectra of the samples where antisolvent was applied after 8 seconds, in Fig. 8 (a), the IPA sample appears to hold up best. If the energy barrier to the phase change has been increased, it could be because of an increase in bond strength resulting from a decrease in defect density, explaining their superior stability. Of all the samples, the worst results were obtained from the sample where ClBn was applied, where a significant decrease in absorbance is seen to take place at wavelengths below the bandgap. This suggests that most of the film had already changed phase.

Fig. 8 (b) shows the absorbance spectra of the aged samples that were used in the dripping time investigation. The sample in which IPA was applied after 10 seconds showed the best stability, since it had the highest absorbance out of any of the aged samples. It even showed superior absorbance to the freshly prepared CsPbIBr$_2$ sample which had no antisolvent treatment. This supports the analysis based on the XRD spectra. The samples where IPA was applied after 15 and 20 seconds showed remarkably similar absorbance spectra, which was only slightly lower than the freshly prepared sample with no antisolvent applied.

The analysis carried out in this section supports the claim that the application of IPA with a dripping time of 10 seconds, or higher, will yield significant improvements in stability. This is indicated by the percentage decrease in intensity going from 20%, with the reference sample, to over 60% in Fig. 7 (a) and the superior absorbance spectra in Fig. 8 (b). The results suggest that to obtain the maximum stability, IPA should be applied with a dripping time of 10 seconds, however any period between 10-15 seconds will also enhance the films properties. This is consistent with the parabolic behaviour found in Fig. 5 (b) which suggests that the ideal application time is 11 seconds.

CsPbIBr$_2$-based solar cells

Using the measured material properties, namely thickness and bandgap, a one-dimensional solar cell capacitance simulator (SCAPS) [49] was used to predict the short circuit currect (J$_{SC}$), the open circuit voltage (V$_{OC}$), the filling fraction (FF) and the device PCE. The parameters used in the simulation which could not be determined experimentally were taken from the literature or in some cases a reasonable estimation was made. All the parameters used in the simulation can be found in the supplementary information in Table 1.

To study the effect that the electron transport layer (ETL) and the hole transport layer (HTL) had on device performance four different cells were simulated. All cells had a layer of FTO as the back contact and used CsPbIBr$_2$ as the absorber layer. In two of the cells, zinc oxide (ZnO) was used as an ETL and in the remaining two titanium dioxide (TiO$_2$) was used. For a given ETL, a simulation was made with and without the commonly used 2,2',7,7'-Tetrakis [N,N-di(4-methoxyphenyl)amino]-9,9'-spirobifluorene (spiro-OMeTAD). The resulting J-V curves and cell properties are shown in Fig. 9 and Table 3 respectively.

The J-V results revealed that the use of the HTL, spiro-OMeTAD, had a major impact on the performance of the solar cell, shown by the increase in FF from 50% to over 80%. On the other hand, Jsc remained largely unchanged since the bandgap of spiro-OMeTAD, 3.17eV, is comparable to that of the ETLs, 3.2 and 3.3eV, and larger than that of CsPbIBr$_2$ 2.05eV. For this reason, a similar number of photons were absorbed with or without the HTL. Interestingly, the V$_{OC}$ increased in the cell where TiO$_2$ was used when the HTL was added but the opposite took place in the cell where ZnO was used. It is possible that this occurs because of the differences in dopant density and therefore carrier concentration. This finding suggests that when selecting the ETL, one should consider whether an HTL is to be included in the device and how they will perform together. In terms of PCE, the cells in which spiro-OMeTAD was used showed significant increases. The champion cell, where TiO$_2$ was used as an ETL, gave a PCE of 13.7%, which is higher

than the record experimental value of 11.53% 44. To date, much focus has been made on HTL-free CsPbIBr$_2$-based devices [15, 21, 31, 34] and our findings suggest that many of the experimentally tested devices could be significantly enhanced by the addition of an appropriate HTL.
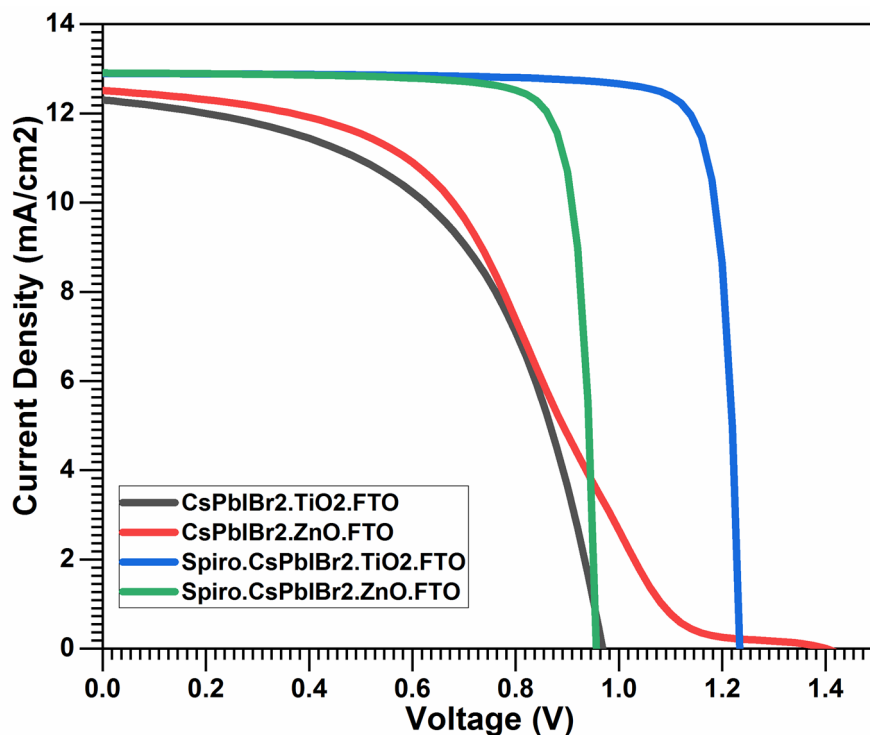
Figure 9: J-V curves corresponding to the different CsPbIBr$_2$-based solar cells with different hole- and electron-transport layers.

2.2.4   Discussion

Our findings support the hypothesis that both antisolvent selection and application conditions have a measurable impact on the final sample. Our results have helped clarify and quantify the effects that different factors have on the quality of antisolvent quenched CsPbIBr$_2$. We have shown that the antisolvent used and the dripping time both play a major role on the processed samples.

It is reasonable to suppose that antisolvent selection must be important since different solvent-antisolvent combinations will behave differently together, due to their varying properties. However, more surprisingly, we

Table 2.4: The atomic percentages of the freshly deposited $CsPbIBr_2$ samples using no antisolvent, IPA, DEE, ClBn and Tl.

Solar cell structure	V_{OC} (V)	J_{SC} (mA cm^{-2})	FF (%)	PCE (%)
$CsPbIBr_2$/ZnO/FTO	1.273	12.569	48.61	7.78
Spiro/$CsPbIBr_2$/ZnO/FTO	1.057	12.905	84.82	11.57
$CsPbIBr_2$/TiO$_2$/FTO	1.230	12.302	53.36	6.36
Spiro/$CsPbIBr_2$/TiO$_2$/FTO	1.235	12.894	86.05	13.70

discovered that the dripping time, an often-ignored factor, seems to have a large effect on the final sample and therefore should not be overlooked when integrating antisolvent quenching into the film synthesis procedure. It seems important that enough time be given for the solution to spread out, however when the dripping time is too long properties of the film decrease due to the other processes taking place during crystallisation. Although the time needed for the solution to spread out is probably a function of viscosity, surface wetness and surface tension of the solution, in our case, we believe it to be somewhere between 8-10 seconds.

While our results support the claim that antisolvent quenching can improve the quality of $CsPbIBr_2$ samples, a possible explanation for why antisolvent quenching is not commonplace with $CsPbIBr_2$ is because when other researchers have tried the method, they obtained results like ours for DEE, ClBn and Tl. Namely, that the processed samples decreased in quality (Fig. 2). It might be that DMSO is not extracted as well as dimethylformamide (DMF) by these antisolvents, so antisolvent methodologies used in hybrid perovskites, such as methylammonium lead iodide, may not extend to inorganic perovskites.

The difficulty in successfully optimizing the antisolvent quenching method may also explain the deviation of our results from the only published method presented by Zhang et al. A possible explanation for our different results is that the antisolvent quenching method is sensitive to small changes in methodology. While on paper our experiments are very similar, there may be subtle differences in the way in which our work was carried out. These differences may include uncontrolled variables in ambient conditions, solution components or the deposition conditions. In Zhang et al.'s paper, they used the same antisolvents we did, namely ClBn, IPA, Tl and DEE, however they found DEE to be the best antisolvent, which contradicts our findings significantly. During their experimental work, Zhang et al. employed a dripping time of 20 seconds, which they did not vary, leaving open the possibility that their method may be further optimized. We optimized this parameter for the best antisolvent, IPA, by varying the dripping time and studying the quality and stability of the synthesized samples as described

in the methodology section.

Several studies into antisolvent quenching methods for the sister materials $CsPbI_2Br$ and $CsPbBr_3$ [39, 50], found, like us, that IPA was the best antisolvent. Liu et al. reported using ClBn to carry out their antisolvent quenching method [40], however they used DMF as a solvent, which is unusual in $CsPbX_3$ films containing bromine due to the difficulty it causes in dissolving the bromine-containing precursors. Based on these papers, IPA appears to be an antisolvent that lends itself well to approaches where only DMSO is used as a solvent, however as soon as DMF is added to the solvent, other antisolvents perform better. Since initial literature reviews of researchers working on $CsPbIBr_2$ may not include sister materials, and the vast majority of $CsPbIBr_2$ films are made with DMSO [31, 34, 43, 51], our findings should be taken into account by other researchers, since they may not be aware that there is an alternative antisolvent quenching method available to the one presented by Zhang et al.

In our experience, DEE was found to be impractical to work with because of its tendency to drop out of the pipette very quickly. It is likely that the low-boiling point of this antisolvent significantly increases the evaporation taking place within the pipette tip, lowering the pressure, resulting in the DEE being ejected from the pipette. We overcame this dripping effect by taking up some air at the end of the pipette and we also tried an alternative method which involved saturating the interior of the pipette tip with DEE vapour beforehand and this also seemed to work. The use of these techniques, however, is clearly a limitation if volumetric errors need to be minimized. Furthermore, DEE is not miscible with DMSO [38], which could cause a nonuniform distribution of DMSO and DEE when quenched. This would lead to a nonuniform deposition of perovskite material as well as their different boiling points leading to inhomogeneous drying and crystal nucleation.

Although our results allow us to claim with a high degree of certainty that IPA quenching $CsPbIBr_2$ will result in a more stable film, we acknowledge that the method could be improved by including other diffraction peaks or complementing it with another easily quantifiable piece of data such as band gap value or absorption coefficient. We have established that FESEM analysis is problematic because it is difficult to quantify and depending on film uniformity, a single image may not be enough to fully capture the nature of the surface.

Our work has established some of the foundations for future studies, where we will extend our investigation of dripping time dependence to the other antisolvents. While considering the dripping time on sample quality and stability, an improved understanding of the effect of the volumetric ratio between the perovskite and antisolvent was identified as necessary to understanding the results. This will be addressed in a forthcoming paper. This is necessary because, although in our methodology we state a volumetric

ratio of 2:1 between the antisolvent and the precursor solution, as the spin programme runs solution is thrown off, therefore changing this volumetric ratio. The lack of information about this variable makes it difficult to explain the observed parabolic behaviour of the intensity in Fig. 5 (b). While the increase in intensity can be attributed to the settling of the solution, the decrease that happens after around 11 seconds is likely due to the processes taking place when the crystal precipitates. Our hypothesis is that once the volumetric ratio goes above a certain level, the metastable limit is passed for an extended period, causing rapid nucleation and crystal growth, leading to many defects at the interfaces where these zones meet. To confirm this, more information about the metastable zone width is needed.

2.2.5 Conclusion

Improving the quality of $CsPbIBr_2$ samples is vital to enable further its use in solar cells. We believe that the results presented here make an important contribution in understanding how to improve crystallinity and stability of $CsPbIBr_2$ samples. We have conducted a preliminary analysis to discover which variables and conditions appear to have the greatest impact. In the absence of generally accepted tests for stability, we have developed our own method using XRD spectra. In our method, the percentage decrease in the intensity of diffraction peaks is compared between the samples as they evolve allowing us to quantify the THEIR stability. Our results show that application of the antisolvent IPA with a dripping time of 10 seconds, is a simple and reproducible way to substantially improve sample quality.

We report $CsPbIBr_2$ films, whose composition was confirmed via EDS, with a mean thickness of 296nm (s.d. 28nm). While carrying out testing to determine the best antisolvent, FESEM analysis revealed that the Tl and ClBn samples showed large-scale defects. Rietveld refinement of the XRD spectra revealed the formation of a cubic structure, pertaining to the PM-3M space group, with a lattice constant of 5.93423$\pm$0.00034 Å. The samples were highly oriented in the (100) direction, with two major diffraction peaks occurring at 15° and 30°, corresponding to the (100) and (200) planes respectively. From the FWHM, the samples applied with IPA showed an increased crystallite size of 55nm. This should reduce the number of boundaries at which charge recombination can occur in solar cells, thereby increasing PCE. All samples with antisolvents applied showed an increased absorbance, and PL spectra showed signs of the Hoke Effect taking place.

While investigating the effects of dripping time on IPA quenched samples, FESEM images revealed that dripping times of 5 and 20 seconds led to large-scale defects. XRD spectra differed only in the intensities of the (100) and (200) peaks. These peak intensities took a parabolic form as a function of dripping time, with a maximum at 11 seconds. All XRD spectra of IPA quenched $CsPbIBr_2$ showed superior intensities when compared to

the reference sample, which had no antisolvent applied. Absorbance spectra of the IPA quenched samples was similar to that of the reference sample, however PL intensity showed a two-fold increase when dripping time was 10 seconds or higher.

To quantify the stability of the samples we developed and employed a novel system based on XRD spectra and complemented this with an analysis of the absorbance spectra. This was prompted by the lack of established stability tests in the literature, and the need for a quantitative rather than qualitative method for measuring sample stability, since qualitative information can be more easily misinterpreted. Our method showed that the samples with IPA applied after 10 and 15 seconds exhibited an important increase in stability, with only a 65% reduction in the intensity of their XRD spectra after 5 weeks stored in ambient conditions, compared to a 20% reduction in the reference sample. These samples gave superior XRD spectra readings than the freshly prepared reference sample, even after they were aged for 5 weeks in air. The sample where IPA was applied after 20 seconds also showed a moderate increase in stability. On the other hand, the sample where IPA was applied after 5 seconds gave poor results across the board, leadings us to conclude that a minimum and specified amount of time is necessary for optimum dispersal of the solution. According to XRD data, the samples where other antisolvents were used showed accelerated degradation, along with the appearance of new phases. The absorbance spectra corresponding to the fresh and aged samples showed results that supported all of the findings made with the aforementioned method. Namely that the sample in which IPA was applied with a dripping time of 10 seconds showed better results than the freshly prepared reference sample even after it had been stored in air for 5 weeks. This increase in stability also takes place in the samples where dripping time was higher, but to a lesser degree.

To probe the properties of devices made with the optimized $CsPbIBr_2$ films, four different devices were simulated using the programme SCAPs. The devices were made with either ZnO or TiO_2, both with and without spiro-OMeTAD. The addition of spiro-OMeTAD was shown to make an important increase in device performance supporting its use as a simple way to significantly enhance device performance. The champion device was the one which employed both spiro-OMeTAD and TiO_2. This solar cell gave a PCE of 13.7%, which is higher than the best reported single junction device found in the literature. Moreover, it gave very competitive values for V_{OC}, Jsc and FF which were 1.235V, 12.894 mAcm^{-2} and 86.05%, respectively.

We have established that the application of IPA with a dripping time of 10 seconds is a simple and reproducible method for significantly improving sample quality. We anticipate that our method should greatly enhance $CsPbIBr_2$ sample production and contribute to the development of solar panels as a source of renewable energy. The development of solar panels is of utmost importance in the face of the impending climate crisis and will be

vital in achieving the goal of transitioning to net-zero carbon emissions by 2050 as set out in the Paris Agreements.

2.2.6 Acknowledgments

Bibliography

[1] H. J. Snaith, "Perovskites: The emergence of a new era for low-cost, high-efficiency solar cells," *Journal of Physical Chemistry Letters*, vol. 4, pp. 3623–3630, 11 2013.

[2] National Renewable Energy Laboratory, "Best research-cell efficiency chart — photovoltaic research," 2023.

[3] T. Wang, B. Daiber, J. M. Frost, S. A. Mann, E. C. Garnett, A. Walsh, and B. Ehrler, "Indirect to direct bandgap transition in methylammonium lead halide perovskite," *Energy and Environmental Science*, vol. 10, pp. 509–515, 2017.

[4] A. Miyata, A. Mitioglu, P. Plochocka, O. Portugall, J. T. W. Wang, S. D. Stranks, H. J. Snaith, and R. J. Nicholas, "Direct measurement of the exciton binding energy and effective masses for charge carriers in organic-inorganic tri-halide perovskites," *Nature Physics*, vol. 11, pp. 582–587, 2015.

[5] V. D'Innocenzo, G. Grancini, M. J. Alcocer, A. R. S. Kandada, S. D. Stranks, M. M. Lee, G. Lanzani, H. J. Snaith, and A. Petrozza, "Excitons versus free charges in organo-lead tri-halide perovskites," *Nature Communications*, vol. 5, 4 2014.

[6] L. M. Herz, "Charge-carrier mobilities in metal halide perovskites: Fundamental mechanisms and limits," *ACS Energy Letters*, vol. 2, pp. 1539–1548, 7 2017.

[7] M. J. P. Alcocer, T. Leijtens, L. M. Herz, A. Petrozza, and H. J. Snaith, "Electron-hole diffusion lengths exceeding trihalide perovskite absorber," *Science*, vol. 342, pp. 341–344, 2013.

[8] G. Xing, N. Mathews, S. S. Lim, N. Yantara, X. Liu, D. Sabba, M. Grätzel, S. Mhaisalkar, and T. C. Sum, "Low-temperature solution-processed wavelength-tunable perovskites for lasing," *Nature Materials 2014 13:5*, vol. 13, pp. 476–480, 3 2014.

[9] A. Leguy, Y. Hu, M. Campoy-quiles, M. I. Alonso, O. J. Weber, P. Azarhoosh, M. V. Schilfgaarde, M. T. Weller, T. Bein, J. Nelson, P. Docampo, and P. R. F. Barnes, "The reversible hydration of ch nh pbi in films , single crystals and solar cells the reversible hydration of ch 3 nh 3 pbi 3 in films , single crystals and solar cells," *Chemistry of Materials*, vol. 27, p. 3397–3407, 2015.

[10] C. Yi, J. Luo, S. Meloni, A. Boziki, N. Ashari-Astani, C. Grätzel, S. M. Zakeeruddin, U. Röthlisberger, and M. Grätzel, "Entropic stabi-

lization of mixed a-cation abx3 metal halide perovskites for high performance perovskite solar cells," *Energy and Environmental Science*, vol. 9, pp. 656–662, 2016.

[11] A. D. Jodlowski, C. Roldán-Carmona, G. Grancini, M. Salado, M. Ralaiarisoa, S. Ahmad, N. Koch, L. Camacho, G. D. Miguel, and M. K. Nazeeruddin, "Large guanidinium cation mixed with methylammonium in lead iodide perovskites for 19% efficient solar cells," *Nature Energy*, vol. 2, pp. 972–979, 2017.

[12] C. C. Stoumpos, C. D. Malliakas, and M. G. Kanatzidis, "Semiconducting tin and lead iodide perovskites with organic cations: Phase transitions, high mobilities, and near-infrared photoluminescent properties," *Inorganic Chemistry*, vol. 52, pp. 9019–9038, 2013.

[13] M. Saliba, T. Matsui, J. Y. Seo, K. Domanski, J. P. Correa-Baena, M. K. Nazeeruddin, S. M. Zakeeruddin, W. Tress, A. Abate, A. Hagfeldt, and M. Grätzel, "Cesium-containing triple cation perovskite solar cells: Improved stability, reproducibility and high efficiency," *Energy and Environmental Science*, vol. 9, pp. 1989–1997, 2016.

[14] C. Liu, W. Li, C. Zhang, Y. Ma, J. Fan, and Y. Mai, "All-inorganic cspbi2br perovskite solar cells with high efficiency exceeding 13%," *Journal of the American Chemical Society*, vol. 140, pp. 3825–3828, 3 2018.

[15] Q. Ma, S. Huang, X. Wen, M. A. Green, and A. W. Ho-Baillie, "Hole transport layer free inorganic cspbibr2 perovskite solar cell by dual source thermal evaporation," *Advanced Energy Materials*, vol. 6, pp. 2–6, 2016.

[16] Y. Han, S. Meyer, Y. Dkhissi, K. Weber, J. M. Pringle, U. Bach, L. Spiccia, and Y. B. Cheng, "Degradation observations of encapsulated planar ch3nh3pbi3 perovskite solar cells at high temperatures and humidity," *Journal of Materials Chemistry A*, vol. 3, pp. 8139–8147, 2015.

[17] G. Divitini, S. Cacovich, F. Matteocci, L. Cinà, A. D. Carlo, and C. Ducati, "In situ observation of heat-induced degradation of perovskite solar cells," *Nature Energy*, vol. 1, 2016.

[18] S. W. Lee, S. Kim, S. Bae, K. Cho, T. Chung, L. E. Mundt, S. Lee, S. Park, H. Park, M. C. Schubert, S. W. Glunz, Y. Ko, Y. Jun, Y. Kang, H. S. Lee, and D. Kim, "Uv degradation and recovery of perovskite solar cells," *Scientific Reports*, vol. 6, pp. 1–10, 2016.

[19] D. Wang, M. Wright, N. K. Elumalai, and A. Uddin, "Stability of perovskite solar cells," *Solar Energy Materials and Solar Cells*, vol. 147, pp. 255–275, 2016.

[20] D. B. Straus, S. Guo, A. M. Abeykoon, and R. J. Cava, "Understanding the instability of the halide perovskite cspbi3 through temperature-dependent structural analysis," *Advanced Materials*, vol. 32, pp. 1–8, 2020.

[21] J. Liang, Z. Liu, L. Qiu, Z. Hawash, L. Meng, Z. Wu, Y. Jiang, L. K. Ono, and Y. Qi, "Enhancing optical, electronic, crystalline, and morphological properties of cesium lead halide by mn substitution for high-stability all-inorganic perovskite solar cells with carbon electrodes," *Advanced Energy Materials*, vol. 8, pp. 1–7, 2018.

[22] Y. Guo, F. Zhao, J. Tao, J. Jiang, J. Zhang, J. Yang, Z. Hu, and J. Chu, "Efficient and hole-transporting-layer-free cspbi 2 br planar heterojunction perovskite solar cells through rubidium passivation," *ChemSusChem*, vol. 12, pp. 983–989, 2019.

[23] W. Zhu, Q. Zhang, D. Chen, Z. Zhang, Z. Lin, J. Chang, J. Zhang, C. Zhang, and Y. Hao, "Intermolecular exchange boosts efficiency of air-stable, carbon-based all-inorganic planar cspbibr2 perovskite solar cells to over 9%," *Advanced Energy Materials*, vol. 8, pp. 1–11, 2018.

[24] S. Mariotti, O. S. Hutter, L. J. Phillips, P. J. Yates, B. Kundu, and K. Durose, "Stability and performance of cspbi2br thin films and solar cell devices," *ACS Applied Materials and Interfaces*, vol. 10, pp. 3750–3760, 2018.

[25] C. F. J. Lau, X. Deng, Q. Ma, J. Zheng, J. S. Yun, M. A. Green, S. Huang, and A. W. Ho-Baillie, "Cspbibr2 perovskite solar cell by spray-assisted deposition," *ACS Energy Letters*, vol. 1, pp. 573–577, 9 2016.

[26] M. Jošt, L. Kegelmann, L. Korte, and S. Albrecht, "Monolithic perovskite tandem solar cells: A review of the present status and advanced characterization methods toward 30% efficiency," *Advanced Energy Materials*, vol. 10, 2020.

[27] H. Wang, H. Li, S. Cao, M. Wang, J. Chen, and Z. Zang, "Interface modulator of ultrathin magnesium oxide for low-temperature-processed inorganic cspbibr2 perovskite solar cells with efficiency over 11%," *Solar RRL*, vol. 4, pp. 1–11, 2020.

[28] Q. Zhang, W. Zhu, D. Chen, Z. Zhang, Z. Lin, J. Chang, J. Zhang, C. Zhang, and Y. Hao, "Light processing enables efficient carbon-based,

all-inorganic planar cspbibr 2 solar cells with high photovoltages," *ACS Applied Materials and Interfaces*, vol. 11, pp. 2997–3005, 2019.

[29] J. Pan, X. Zhang, Y. Zheng, and W. Xiang, "Morphology control of perovskite film for efficient cspbibr2 based inorganic perovskite solar cells," *Solar Energy Materials and Solar Cells*, vol. 221, p. 110878, 2021.

[30] B. Zhang, W. Bi, Y. Wu, C. Chen, H. Li, Z. Song, Q. Dai, L. Xu, and H. Song, "High-performance cspbibr2 perovskite solar cells: Effectively promoted crystal growth by antisolvent and organic ion strategies," *ACS Applied Materials and Interfaces*, vol. 11, pp. 33868–33878, 2019.

[31] W. Zhu, Z. Zhang, W. Chai, Q. Zhang, D. Chen, Z. Lin, J. Chang, J. Zhang, C. Zhang, and Y. Hao, "Band alignment engineering towards high efficiency carbon-based inorganic planar cspbibr2 perovskite solar cells," *ChemSusChem*, vol. 12, pp. 2318–2325, 2019.

[32] W. Zhu, Q. Zhang, C. Zhang, Z. Zhang, D. Chen, Z. Lin, J. Chang, J. Zhang, and Y. Hao, "Aged precursor solution toward low-temperature fabrication of efficient carbon-based all-inorganic planar cspbibr2 perovskite solar cells," *ACS Applied Energy Materials*, vol. 1, pp. 4991–4997, 2018.

[33] A. W. Stewart, A. Bouich, and B. Marí, "Inorganic perovskites improved film and crystal quality of cspbibr2 when doped with rubidium," *Journal of Materials Science: Materials in Electronics*, pp. 1–9, 9 2021.

[34] W. Zhang, Z. Zhang, Q. Jiang, Z. Wei, Y. Zhang, and H. You, "Charge-transporting-layer-free, all-inorganic cspbibr 2 perovskite solar cells via dipoles-adjusted interface," *Nanomaterials*, 2020.

[35] W. Li, M. U. Rothmann, A. Liu, Z. Wang, Y. Zhang, A. R. Pascoe, J. Lu, L. Jiang, Y. Chen, F. Huang, Y. Peng, Q. Bao, J. Etheridge, U. Bach, and Y. B. Cheng, "Phase segregation enhanced ion movement in efficient inorganic cspbibr2 solar cells," *Advanced Energy Materials*, vol. 7, pp. 1–8, 2017.

[36] M. Xiao, F. Huang, W. Huang, Y. Dkhissi, Y. Zhu, J. Etheridge, A. Gray-Weale, U. Bach, Y.-B. Cheng, and L. Spiccia, "A fast deposition-crystallization procedure for highly efficient lead iodide perovskite thin-film solar cells," *Angewandte Chemie*, vol. 126, pp. 10056–10061, 2014.

[37] D. Shi, V. Adinolfi, R. Comin, M. Yuan, E. Alarousu, A. Buin, Y. Chen, S. Hoogland, A. Rothenberger, K. Katsiev, Y. Losovyj, X. Zhang, P. A. Dowben, O. F. Mohammed, E. H. Sargent, and O. M. Bakr, "Low

trap-state density and long carrier diffusion in organolead trihalide perovskite single crystals," *Science*, vol. 347, pp. 519–522, 2015.

[38] S. Paek, P. Schouwink, E. N. Athanasopoulou, K. T. Cho, G. Grancini, Y. Lee, Y. Zhang, F. Stellacci, M. K. Nazeeruddin, and P. Gao, "From nano- to micrometer scale: The role of antisolvent treatment on high performance perovskite solar cells," *Chemistry of Materials*, vol. 29, pp. 3490–3498, 2017.

[39] W. Chen, H. Chen, G. Xu, R. Xue, S. Wang, Y. Li, and Y. Li, "Precise control of crystal growth for highly efficient cspbi2br perovskite solar cells," *Joule*, vol. 3, pp. 191–204, 2019.

[40] X. Liu, J. Li, Z. Liu, X. Tan, B. Sun, S. Xi, T. Shi, Z. Tang, and G. Liao, "Vapor-assisted deposition of cspbibr2 films for highly efficient and stable carbon-based planar perovskite solar cells with superior voc," *Electrochimica Acta*, vol. 330, p. 135266, 2020.

[41] C. Liu, W. Li, J. Chen, J. Fan, Y. Mai, and R. E. Schropp, "Ultra-thin moox as cathode buffer layer for the improvement of all-inorganic cspbibr2 perovskite solar cells," *Nano Energy*, vol. 41, pp. 75–83, 11 2017.

[42] G. E. Eperon, G. M. Paternò, R. J. Sutton, A. Zampetti, A. A. Haghighirad, F. Cacialli, and H. J. Snaith, "Inorganic caesium lead iodide perovskite solar cells," *Journal of Materials Chemistry A*, vol. 3, pp. 19688–19695, 2015.

[43] Y. Guo, X. Yin, J. Liu, S. Wen, Y. Wu, and W. Que, "Inorganic cspbibr2-based perovskite solar cells: Fabrication technique modification and efficiency improvement," *Solar RRL*, vol. 3, pp. 1–13, 2019.

[44] E. T. Hoke, D. J. Slotcavage, E. R. Dohner, A. R. Bowring, H. I. Karunadasa, and M. D. McGehee, "Reversible photo-induced trap formation in mixed-halide hybrid perovskites for photovoltaics," *Chemical Science*, vol. 6, pp. 613–617, 1 2015.

[45] K. A. Bush, K. Frohna, R. Prasanna, R. E. Beal, T. Leijtens, S. A. Swifter, and M. D. McGehee, "Compositional engineering for efficient wide band gap perovskites with improved stability to photoinduced phase segregation," *ACS Energy Letters*, vol. 3, pp. 428–435, 2018.

[46] Z. Chen and P. A. Bobbert, "Unified theory for light-induced halide segregation in mixed halide perovskites," *Nature Communications*, pp. 1–10.

[47] R. E. Beal, D. J. Slotcavage, T. Leijtens, A. R. Bowring, R. A. Belisle, W. H. Nguyen, G. F. Burkhard, E. T. Hoke, and M. D. McGehee, "Cesium lead halide perovskites with improved stability for tandem solar cells," *Journal of Physical Chemistry Letters*, vol. 7, pp. 746–751, 2016.

[48] R. J. Sutton, G. E. Eperon, L. Miranda, E. S. Parrott, B. A. Kamino, J. B. Patel, M. T. Hörantner, M. B. Johnston, A. A. Haghighirad, D. T. Moore, and H. J. Snaith, "Bandgap-tunable cesium lead halide perovskites with high thermal stability for efficient solar cells," *Advanced Energy Materials*, vol. 6, pp. 1–6, 2016.

[49] M. Burgelman, P. Nollet, and S. Degrave, "Modelling polycrystalline semiconductor solar cells," *Thin Solid Films*, vol. 361, pp. 527–532, 2 2000.

[50] B. W. Kim, J. H. Heo, J. K. Park, D. S. Lee, H. Park, S. Y. Kim, J. H. Kim, and S. H. Im, "Morphology controlled nanocrystalline cspbbr3 thin-film for metal halide perovskite light emitting diodes," *Journal of Industrial and Engineering Chemistry*, vol. 97, pp. 417–425, 2021.

[51] Y. Li, J. Duan, H. Yuan, Y. Zhao, B. He, and Q. Tang, "Lattice modulation of alkali metal cations doped $cs_{1-x}r_x$pbbr3 halides for inorganic perovskite solar cells," *Solar RRL*, vol. 2, pp. 1–8, 2018.

2.2.8   Supplementary Materials

Enhancing the stability and crystallinity of CsPbIBr₂ through antisolvent engineering

Alexander W. Stewart, Amal Bouich Bernabé Marí Soucase

Institut de Disseny i Fabricació, Universitat Politècnica de València, Camí de Vera, València, Spain 46022

Corresponding author email: alste5@doctor.upv.es

Table 1: The parameters of the materials used for the simulation.

Parameters	Spiro	CsPbIBr$_2$	TiO$_2$	ZnO	FTO
Thickness (um)	0.20	2.00	0.05	0.05	0.5*
Bandgap (eV)	3.17	2.05[1,2]	3.2[3–5]	3.3[4,6,7]	3.5[3,5,8]
Electron affinity (eV)	2.05[3,9]	3.49[10]	3.9[3,5]	4.4[7]	4.0[3,5,6,8]
Dielectric Permittivity	3.00[3–5]	20.0	9.0[3,5]	9.0[4,6,7]	9.0[3–5,8]
CB Effective Density of States (1/cm³)	2.2E+17	1.0E+19	2.0E+17[11]	2.2E+18[6, 7]	2.2E+18[3, 4]
VB Effective Density of States (1/cm³)	1.8E+17	1.0E+19	6.0E+17[11]	1.8E+19[4, 6,7]	1.8E+19[3, 4]
Electron Thermal Velocity (cm/s)	1.0E+8	1.0E+7	1.0E+7 [3]	1.0E+7	1.0E+7[3]
Hole Thermal Velocity (cm/s)	1.0E+7[3]	1.0E+7	1.0E+7 [3]	1.0E+7	1.0E+7[3]
Electron Mobility (cm²/Vs)	2.0E-4[5]	2.30E+3[12]	1.00E+2 [11]	1.00E+2[4, 6,7]	2.00E+1[3, 5,13]
Hole Mobility (cm²/Vs)	2.0E-4[3,5,14]	3.20E+2[12]	2.50E+1[11]	2.50E+1[6, 7]	1.00E+1[3, 4,13]
Donor Density ND (1/cm³)	0.0E+0	1.0E+9	1.0E+17 [11]	2.0E+18	1.0E+17[4]
Acceptor Density NA (1/cm³)	2.0E+19	1.0E+9	0.0E+0	0.0E+0	0.0E+0

* Manufacturers specifications, XOP Glass

Bibliography

[1] C. F. J. Lau, X. Deng, Q. Ma, J. Zheng, J. S. Yun, M. A. Green, S. Huang, and A. W. Ho-Baillie, "Cspbibr2 perovskite solar cell by spray-assisted deposition," *ACS Energy Letters*, vol. 1, pp. 573–577, 9 2016.

[2] Q. Ma, S. Huang, X. Wen, M. A. Green, and A. W. Ho-Baillie, "Hole transport layer free inorganic cspbibr2 perovskite solar cell by dual source thermal evaporation," *Advanced Energy Materials*, vol. 6, pp. 2–6, 2016.

[3] E. Karimi and S. M. Ghorashi, "Investigation of the influence of different hole-transporting materials on the performance of perovskite solar cells," *Optik*, vol. 130, pp. 650–658, 2017.

[4] Y. Raoui, H. Ez-Zahraouy, N. Tahiri, O. E. Bounagui, S. Ahmad, and S. Kazim, "Performance analysis of mapbi3 based perovskite solar cells employing diverse charge selective contacts: Simulation study," *Solar Energy*, vol. 193, pp. 948–955, 2019.

[5] T. Minemoto and M. Murata, "Device modeling of perovskite solar cells based on structural similarity with thin film inorganic semiconductor solar cells," *Journal of Applied Physics*, vol. 116, 2014.

[6] P. Chelvanathan, M. I. Hossain, and N. Amin, "Performance analysis of copper-indium-gallium-diselenide (cigs) solar cells with various buffer layers by scaps," *Current Applied Physics*, vol. 10, pp. 387–391, 2010.

[7] O. K. Simya, A. Mahaboobbatcha, and K. Balachander, "A comparative study on the performance of kesterite based thin film solar cells using scaps simulation program," *Superlattices and Microstructures*, vol. 82, pp. 248–261, 2015.

[8] U. Mandadapu, "Simulation and analysis of lead based perovskite solar cell using scaps-1d," *Indian Journal of Science and Technology*, vol. 10, pp. 1–8, 2017.

[9] T. Leijtens, I. K. Ding, T. Giovenzana, J. T. Bloking, M. D. McGehee, and A. Sellinger, "Hole transport materials with low glass transition temperatures and high solubility for application in solid-state dye-sensitized solar cells," *ACS Nano*, vol. 6, pp. 1455–1462, 2 2012.

[10] W. Zhu, Z. Zhang, W. Chai, Q. Zhang, D. Chen, Z. Lin, J. Chang, J. Zhang, C. Zhang, and Y. Hao, "Band alignment engineering towards high efficiency carbon-based inorganic planar cspbibr2 perovskite solar cells," *ChemSusChem*, vol. 12, pp. 2318–2325, 2019.

[11] G. Xosrovashvili and N. E. Gorji, "Numerical analysis of tio2/cu2znsns4 nanostructured pv using scaps-1d," *Journal of Modern Optics*, vol. 60, pp. 936–940, 2013.

[12] C. C. Stoumpos, C. D. Malliakas, and M. G. Kanatzidis, "Semiconducting tin and lead iodide perovskites with organic cations: Phase transitions, high mobilities, and near-infrared photoluminescent properties," *Inorganic Chemistry*, vol. 52, pp. 9019–9038, 2013.

[13] U. Mandadapu, S. Vedanayakam, K. Thyagarajan, M. Reddy, and B. Jagadeeshbabu, "Design and simulation of high efficiency tin halide perovskite solar cell," *International Journal of Renewable Energy Research*, 2017.

[14] L. Schmidt-Mende and M. Grätzel, "Tio2 pore-filling and its effect on the efficiency of solid-state dye-sensitized solar cells," *Thin Solid Films*, vol. 500, pp. 296–301, 4 2006.

2.3 Shedding light on electronically doped perovskites

Shedding light on electronically doped perovskites

A.W. Stewart [a, b, *], A. Julien [b], D. Regaldo [b], P. Schulz [c], B. Marí Soucase [a], D.R. Ceratti [c, **], P. López-Varo [b, ***]

[a] Universitat Politècnica de València, Camí de Vera, S/n, 46022, Valencia, Spain
[b] Insitute Photovoltaïque D'Ile de France, 18 Bd Thomas Gobert, 91120 Palaiseau, France
[c] CNRS, UMR 9006, IPVF, Institut Photovoltaïque D'Ile-de-France, 18 Boulevard Thomas Gobert, 91120 Palaiseau, France

ARTICLE INFO

ABSTRACT

Halide perovskites solar cells (PSCs) are making true on past promises, having reached power conversion efficiencies (PCEs) of 25.7% and long lifespans (>3000 h). Although stability has become the focus of research efforts, a significant number of researchers are still dedicated to further increasing cell efficiency. To push PCE any higher however, every element of the solar cell must be controlled and optimized. In the context of the recent advancements in halide perovskite doping, we analyse how and why doping can modify the PCE of PSCs. We find that optimal doping levels are highly dependent on carrier mobilities and device architecture, namely whether the hole- or electron-transport layer are on the front-side (illumination-side) of the device. More precisely, there are four regimes defined by carrier mobilities in which different physical processes are more, or less, important causing a change to the optimal doping level. When electron and hole mobilities are comparable, and diffusion lengths are not at least an order of magnitude larger than the perovskite film thickness, devices with the electron-transport layer on the front side (n-i-p) perform better with a p-doped perovskite, whereas devices with the hole-transport layer on the front side (p-i-n) perform better with an n-doped perovskite. The existence of these four regimes is especially pronounced for PSCs due to the very high absorption coefficients and rather low carrier mobilities in halide perovskites. We model the solar cell by employing a drift-diffusion simulation in SCAPS (a Solar Cell Capacitance Simulator) to provide a full rationale for the phenomenon and analyse the conditions under which this effect is significant. The findings presented here are based on the perovskite properties measured by multiple groups and are directed predominantly towards experimentalists working with devices.

1. Introduction

Since their inception, perovskite solar cells (PSCs) have experienced a meteoric growth in terms of power conversion efficiency (PCE), which now sits at a record 25.7% [1,2]. Research efforts have been driven by the attractive properties of tin- and lead-based halide perovskites, including their low cost [3], ability to self-heal [4–7], direct bandgap, high absorption coefficient, low binding energies [8,9], low defect densities [10], as well as large charge carrier diffusion lengths [11,12] and high charge carrier mobilities

[13] for semiconductors made using solution-based deposition methods. Although research into PSCs has been booming over the past decade, halide perovskites also show great potential for other applications including LEDs, photodetectors, gamma-ray-detectors, and sensors. Their unique opto-electronic properties, which can be finely tuned using compositional engineering, make them a promising material for a wide range of applications.

Despite their elusive nature, electronically doped halide perovskites should be possible [14–20] and evidence of them grows daily [21–43]. While experimentally produced halide perovskites are usually considered intrinsic [30,44–46], it is likely that many are not, which is why we seek to better understand them in this paper. Indeed, a recent breakthrough in terms of PSC PCE was directly attributed to electronic doping of the perovskite [47]. Here we report the results of our investigations into the effect of doping halide perovskites, including identification of the conditions under

* Corresponding author.
** Corresponding author.
*** Corresponding author.
E-mail addresses: alste5@doctor.upv.es (A.W. Stewart), davide.ceratti@cnrs.fr (D.R. Ceratti), pilar.lopez-varo@ipvf.fr (P. López-Varo).

Shedding light on electronically doped perovskites

Alexander W. Stewart[*1,2], Arthur Julien[2], Davide Regaldo[2], Philip Schulz[3], Bernabé Marí Soucase[1], Davide R. Ceratti[*3], Pilar Lopez Varo[*2]

[1] Universitat Politècnica de València, Camí de Vera, s/n, 46022 Valencia, Spain
[2] Insitute Photovoltaïque d'Ile de France, 18 Bd Thomas Gobert, 91120 Palaiseau, France
[3] CNRS, UMR 9006, IPVF, Institut Photovoltaïque d'Ile-de-France, 18 Boulevard Thomas Gobert, 91120 Palaiseau, France

[*] Alste5@doctor.upv.es [*] davide.ceratti@cnrs.fr [*] pilar.lopez-varo@ipvf.fr

Abstract:

Halide perovskites solar cells (PSCs) are making true on past promises, having reached power conversion efficiencies (PCEs) of 25.7% and long lifespans (¿3000h). Although stability has become the focus of research efforts, a significant number of researchers are still dedicated to further increasing cell efficiency. To push PCE any higher however, every element of the solar cell must be controlled and optimized. In the context of the recent advancements in halide perovskite doping, we analyse how and why doping can modify the PCE of PSCs. We find that optimal doping levels are highly dependent on carrier mobilities and device architecture, namely whether the hole- or electron-transport layer are on the front-side (illumination-side) of the device. More precisely, there are four regimes defined by carrier mobilities in which different physical processes are more, or less, important causing a change to the optimal doping level. When electron and hole mobilities are comparable, and diffusion lengths are not at least an order of magnitude larger than the perovskite film thickness, devices with the electron-transport layer on the front side (n-i-p) perform better with a p-doped perovskite, whereas devices with the hole-transport layer on the front side (p-i-n) perform better with an n-doped perovskite. The existence of these four regimes is especially pronounced for PSCs due to the very high absorption coefficients and rather low carrier mobilities in halide perovskites. We model the solar cell by employing a drift-diffusion simulation in SCAPS (a Solar Cell Capacitance Simulator) to provide a full rationale for the phenomenon and analyse the conditions under which this effect is significant. The findings presented here are based on the perovskite properties measured by multiple groups and are directed predominantly towards experimentalists working with devices.

Keywords: perovskite, electronic doping, high efficiency, solar cells

2.3.1 Introduction

Since their inception, perovskite solar cells (PSCs) have experienced a meteoric growth in terms of power conversion efficiency (PCE), which now sits at a record 25.7% [1, 2]. Research efforts have been driven by the attractive properties of tin- and lead-based halide perovskites, including their low cost [3], ability to self-heal [4–7], direct bandgap, high absorption coefficient, low binding energies [8, 9], low defect densities [10], as well as large charge carrier diffusion lengths [11, 12] and high charge carrier mobilities [13] for semiconductors made using solution-based deposition methods. Although research into PSCs has been booming over the past decade, halide perovskites also show great potential for other applications including LEDs, photodetectors, gamma-ray-detectors, and sensors. Their unique opto-electronic properties, which can be finely tuned using compositional engineering, make them a promising material for a wide range of applications.

Despite their elusive nature, electronically doped halide perovskites should be possible [14–20] and evidence of them grows daily [21–43]. While experimentally produced halide perovskites are usually considered intrinsic [38, 44–46], it is likely that many are not, which is why we seek to better understand them in this paper. Indeed, a recent breakthrough in terms of PSC PCE was directly attributed to electronic doping of the perovskite [47]. Here we report the results of our investigations into the effect of doping halide perovskites, including identification of the conditions under which a p-type or n-type perovskite layer is desirable, or not, in PSCs. Factors influencing the optimal doping level are also identified. We show that, under conditions of fixed illumination through the substrate, typical PSCs exhibit an optimal doping level depending on the device structure used. This effect occurs due to the asymmetric charge generation profile throughout the bulk of the perovskite absorber. Specifically, we find that n-i-p and p-i-n devices perform better with a p-type or n-type perovskite absorber, respectively. This behaviour has been observed in recent experiments [47] and this paper sets out to propose the underlying theory. Fundamentally, the effect is a consequence of the charge carrier diffusion lengths being on the order of the absorber layer thickness, leading to potential charge extraction difficulties. Moreover, there are reports of diffusion lengths being shortened further by doping [48], which may provoke further charge recombination. Fabricating devices with optimised doping levels is especially important in the case of PSCs due to the high absorption coefficient of the perovskite layer, which highly localises photogenerated carriers. Adding to the complexity, the optimal doping level can be influenced by other perovskite properties, including charge carrier mobilities, defect densities, or layer thicknesses. By exploring the theoretical rationale for these effects, this work endeavours to establish guiding principles for the construction of superior PSCs.

Assuming it is possible to precisely control doping in perovskites, which despite difficulties appears to be the case, our intention is to determine why optimal doping levels arise, and how PCE can be maximised for common PSC architectures. To do so, the drift-diffusion modelling program SCAPS (a Solar Cell Capacitance Simulator) [49, 50] was employed due to its proven track record of closely replicating experimental results [45, 51, 52]. In order to make simulations as physically realistic as possible, the input parameters used were carefully selected, by using a combination of literature values [53–63], in-house measurements and physical intuition (see table S1). To the best of our knowledge, there is little work on understanding electronically doped PSCs. Das et al. studied the effect of doping, photodoping and lateral bandgap variations on device relevant metrics using the Advanced Semiconductor Analysis (ASA) software [48]. Other studies have used simulations to optimise dopant concentration, however they were limited to a small range of values and conditions and tend not to explain the observed behaviour. For example, Raza et al. found that PCE was monotonically increasing as a function of acceptor concentration in p-i-n triple-cation-based PSCs [52]. Conversely, Patel et al. found that increasing the acceptor concentration in $CH_3NH_3SnI_3$-based PSCs led to a monotonical decrease in PCE of n-i-p devices [64]. Peña-Camargo et al. used SCAPS for one of the figures in their paper, and they found that PCE decreases as either acceptor or donor concentrations are increased [45]. Here we analyse a large set of dopant concentrations and properties, demonstrating how doping the perovskite layer can improve, or worsen, device performance depending on cell structure and perovskite film properties. Our results should be of significant interest to researchers working on PSCs because they establish simple guidelines for the improvement of devices. Following these can result in increases in PCE that could be highly impactful for already highly efficient devices. Finally, we provide an overview of the field, highlighting potential techniques for the implementation of these principles as well as future avenues of research.

2.3.2 Results

To investigate PSCs with electronically doped perovskite absorbers, different parts of devices where systematically studied. To begin, the response of PCE to electronic doping of the perovskite absorber in realistic devices is made. In the second section, the impact of charge transport layers is explored. The third section is devoted to the influence of perovskite properties on optimal doping level. This includes the impact of absorption coefficient and device architecture, bulk and interfacial recombination rate, and carrier mobilities on the optimal electronic doping level in the perovskite layer.

Optimal doping levels in realistic devices

To model the electronic doping behaviour of standard lab-made devices we simulated the common n-i-p PSC structure, shown in Figure 1a. Furthermore, we employed widely used electron-transport layer (ETL) and hole-transport layer (HTL) materials, namely TiO2 and spiro-OMeTAD respectively. The material parameters used in the drift-diffusion simulations were carefully selected and can be found in Table S1. Throughout the study the thicknesses of the perovskite and charge transport layers were fixed at 400 nm and 50 nm respectively, which are comparable to the values found in the literature and in the high-performance devices made in our laboratory. Furthermore, to make sure our results were applicable to a range of halide perovskites, we used both the prototypical halide perovskite, $MAPbI_3$, and a triple-cation mixed-halide perovskite, $(MA_{0.17}FA_{0.83})_{0.95}Cs_{0.05}PbBr_{0.51}I_{2.49}$, which is often used in modern high-performance devices. To check the validity of our simulated parameters we compared them with reported experimental values of n-i-p devices using TiO_2 and spiro-OMeTAD, shown in Table 1, however without knowing the electronic doping level of the perovskite layer in the reported cells it is not possible to make a precise comparison. That said, the range with which PCE varies as a function of doping level should be applicable for a device with similar thickness and defect densities. Experimentally produced $MAPbI_3$-based devices appear to perform a few percentage points worse than those in our simulations. This could be explained by several factors including the experimentally produced films being slightly n-type and/or further loss channels in real devices such as defect-induced recombination, geometrical factors, and layer imperfections. On the other hand, experimentally produced triple-cation devices perform slightly better than predicted by our results which we attribute to the fact that we used the same bulk and interface defect densities for both halide perovskites, however there is evidence to suggest that the formamidinium cation promotes rapid defect self-healing [5] and cation mixing can suppress defect formation [15]. Another important point to make is that the values obtained in our simulations are lower than record-breaking PSCs which have PCEs of up to 25.7%2. This is due to the fact that they all used interfacial engineering to reduce non-radiative recombination and they employed slightly different perovskite compositions, making a direct comparison more difficult to be made [65–67]. Nevertheless, our results are applicable to these record PSC too as tuning the values of said parameters in our simulations still results in asymmetrical response of PCE to n-type or p-type doping (see figure S14).

Figures 1b and 1c show PCE as a function of doping level in the perovskite for $MAPbI_3$-based and triple-cation-based devices. The stars show carrier densities reported for these films, in some cases an arrow is used to signal a change in the measured electronic doping level before and after a

Table 2.5: Reported experimental values for PSCs with TiO$_2$/perovskite/spiro-OMeTAD architectures. The PCE of cells in this work correspond to those where the optimal doping level was implemented in the perovskite.

Perovskite composition	PCE	Reference
(MA$_{0.17}$FA$_{0.83}$)$_{0.95}$Cs$_{0.05}$PbBr$_{0.51}$I$_{2.49}$	20.7%	This work
(MA$_{0.17}$FA$_{0.83}$)$_{0.95}$Cs$_{0.05}$PbBr$_{0.51}$I$_{2.49}$	21.1%	Saliba et al. [68]
MA$_{0.15}$FA$_{0.85}$PbBr$_{0.45}$I$_{2.519}$	20.5%	Li et al. [69]
(MA$_{0.15}$FA$_{0.85}$)$_{0.95}$Cs$_{0.05}$PbBr$_{0.43}$I$_{2.57}$	19.76%	Zhao et al. [70]
MAPI$_3$	23.9%	This work
MAPI$_3$	20.2%	Zhang et al. [71]
MAPI$_3$	19.7%	Ahn et al. [72]
MAPI$_3$	19.0%	Noel et al. [73]

technique changing the doping level was used [31, 32]. However, these studies used different device structures meaning that a direct comparison of PCE cannot be made with our results. In Figure 1b and 1c both devices show an asymmetrical response to p-type and n-type doping and perform best when the perovskite layer is p-doped with an acceptor density of $N_A=10^{16}$ cm^{-3}. On the other hand, n-type doping appears to severely hamper performance. Although this behaviour was conserved across a range of absorber layer thicknesses, as thickness decreases the beneficial effect of doping becomes less pronounced since the diffusion length becomes larger with respect to the absorber thickness (see Figure S1). For devices based on both perovskites, there is approximately a 6% difference in PCE between a heavily p-doped and heavily n-doped absorber layer. Since it is not clear whether such high doping levels are physically obtainable, this value should be taken as an upper limit. Figures 1b and 1c also show differences in doping sensitivity, which is how quickly PCE changes as the layer is doped. For both materials, an increase in PCE can be expected with p-doping, however in the case of the triple cation the maximum value of PCE is reached at a lower doping level.

These results raise several questions concerning the cause of this asymmetric doping behaviour, and whether it can be avoided. Our data suggests that the combination of high absorption coefficient and low carrier mobility creates a unique situation in halide perovskites where charge carriers are highly localised, and their diffusion lengths are comparable to the thickness of the perovskite films. This leads to hindered charge extraction which can be improved by electronic doping.
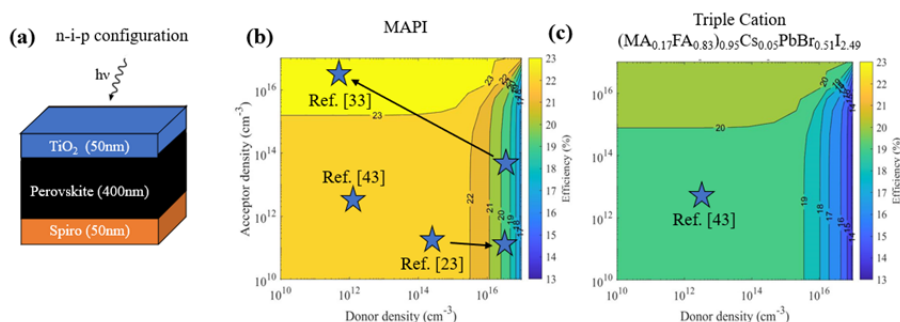
Figure 1: (a) Simulated layer stack representing the structure of the n-i-p solar cell, with Spiro-OMeTAD as HTL and TiO2 as ETL. Contour mappings of PCE as a function of donor and acceptor density in the (b) MAPbI3 and (c) $(MA_{0.17}FA_{0.83})_{0.95}Cs_{0.05}PbBr_{0.51}I_{2.49}$ perovskite layer. The parameters used in these simulations can be found in Table S1. Stars show experimentally measured carrier densities in $MAPbI_3$ and triple-cation mixed-halide perovskites. In some cases an arrow is used to represent the measured carrier densities before and after an electronic doping technique was used.

The impact of transport layers

To determine whether the optimal doping levels in Figure 1 stem from properties of the charge transport layers, non-physical symmetric charge transport layers (see Table S2) were simulated. Both charge transport layers have the same density of states, doping levels and carrier mobilities. Furthermore, the same band offset is considered at the conduction and valence band at the ETL and HTL interfaces respectively. Under these conditions, key parameters of the charge transport layers were systematically varied in the n-i-p configuration to determine the effect on PCE doping response. Even in the case where the charge transport layers properties were symmetric an asymmetric doping level map, such as those in Figure 1, arose. Moreover, this asymmetric behaviour was conserved for a range of doping concentrations, density of states, mobilities, and band offsets (see Figure S2). A more comprehensive analysis of the effect of changing the charge transport layers parameters on PCE can be found in the supporting information (see figure S2-S4). These findings suggest that the optimal doping level is dependent on the nature of the perovskite layer. For this reason, and in order to simplify the interpretation of results, symmetric charge transport layers (see Table S2) were used in the rest of the study.

The impact of bulk perovskite properties

Absorption and photogenerated carrier profile In contrast to the properties of the charge transport layers we found that the profile of pho-

togenerated carriers in the bulk perovskite, which depends on device architecture and optical properties, plays a critical role in identifying an optimal doping level. Figures 2a and 2b show how an optimal p-type or n-type doping can arise by illuminating the same device from the ETL (n-i-p) or HTL (p-i-n) side respectively. This is in agreement with what has been observed experimentally [47]. This asymmetric response to doping is driven mostly by changes in fill factor (see Figure S13). Furthermore, Figure 2c shows how this behaviour disappears when a non-realistic constant generation profile is directly implemented. In this case, the generation profile is non-physical and cannot be straightforwardly related to an incident spectrum and power. For this reason, the total number of photogenerated carriers across the layer was adjusted to be the same as the value obtained by combining a Beer-Lambert Law with the AM1.5 spectrum. This allows for the estimation of PCE by dividing the total power output by a 1 sun intensity. Generation profiles are represented in Figure S5.
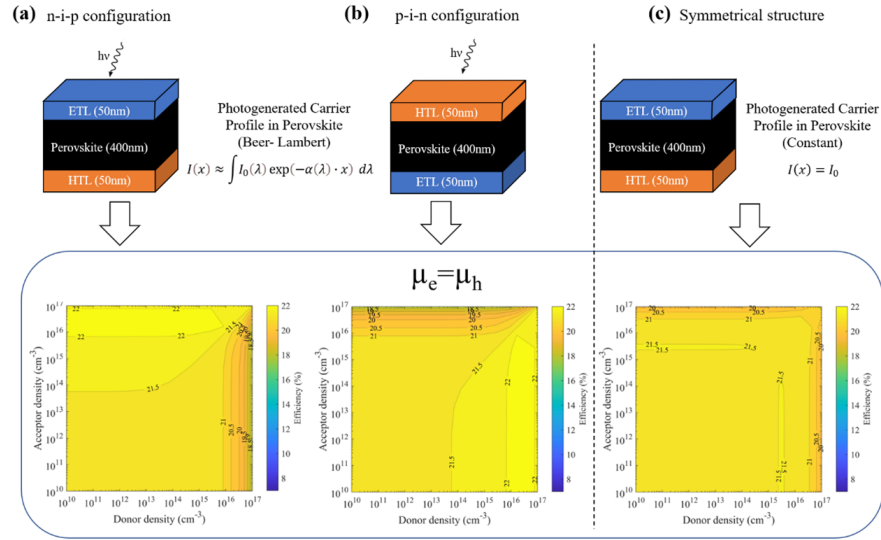

Figure 2: PCE of PSCs using physically realistic parameters and symmetric charge transport layers that have the same band offset, carrier mobilities and doping level. (a) n-i-p structure (photogeneration from illumination on ETL side), (b) p-i-n structure (photogeneration from illumination on HTL side), (c) symmetrical structure (non-physical constant generation rate throughout the perovskite layer).

To further probe the impact of different absorption profiles on optimal doping levels, a range of generation functions were used to simulate photogenerated carriers being created at different depths. These square functions,

seen in Figure 3a, while non-physical when considered independently, can model physically realistic absorption profiles when linear combinations of these functions are used. Figure 3b shows diagrammatically how a Beer-Lambert absorption can be modelled in the perovskite layer by adding a weighting factor to each function. In the limit where the width of the square functions go to zero, any incident spectra can be modelled exactly.

Figure 3c shows the difference in PCE of highly n-doped, with ND=10^{17} cm^{-3}, and highly p-doped, with NA=10^{17} cm^{-3}, devices. Doping level maps for each square function can be found in Figure S8. Intuitively, if charges are generated near an interface, it is easier for them to reach it. If photogenerated carriers are created near the HTL (at 0nm) they will reach it more efficiently than the ETL (at 400nm) since the layer thickness is of the same order as the diffusion length of the charges. In addition, band bending, and the associated electric field, can also promote the separation of charges and their transportation. Doping the perovskite layer localises the band bending at one extremity of the layer and flattens it at the other (see Figure S6), meaning that electric field is also localised (see Figure S7). Since both electric field and photogenerated charge carriers are localised, their respective locations are key for optimising charge carrier extraction. Hence by altering the position of the photogenerated carriers from the HTL-side (as it would be in a p-i-n configuration) to the ETL side (as it would be in an n-i-p configuration), the preference for n-doping turns into a preference for p-doping.

Furthermore, in p-doped materials, the minority carriers (governing charge transport) are electrons while in n-doped materials they are holes. Considering a p-i-n configuration, if the intrinsic material becomes p-doped, the minority carriers, which are electrons, must travel through the entire perovskite layer to reach the ETL while if the material is n-doped, the minority carriers, which are the holes, can easily reach the HTL on the front. This phenomenon, coupled with the localized electric field, explains why PCE is higher when charges are generated near the HTL if the material is n-doped than when it is p-doped as we can see in the left-most point of Figure 3c. Interestingly these effects remain true even when introducing traps in the layer, increasing interface or bulk defects, or lowering carrier mobility (details are provided in Table S3).

As carriers are generated closer to the centre of the layer, the effect diminishes, until it vanishes completely at the centre (at 200 nm), and no doping type is preferred. Moving further to the right, the reasoning can be inverted and it becomes more favourable to be p-doped since the electrons, which are the minority carriers, reach the ETL (at 400nm) more easily.

To probe the non-linear recombination effects that depend on charge concentrations, we simulated solar cells with different exponential decay generation profiles, which correspond physically to absorption coefficients for a given wavelength (i.e. monochromatic light) when illuminated from

125

either the ETL or HTL side. Here again the synthetic generation profiles were weighted to the total generation rate obtained from a Beer-Lambert Law combined with the AM1.5 spectrum. Figure 3d shows the difference in PCE between a heavily n-doped and p-doped device as a function of the absorption coefficient. The higher the absorption coefficient, the more photogeneration is localised near the front interface. This results in an increasingly desirable p-doping when illuminated via the ETL (blue in Figure 3d) or n-doping when illuminated via the HTL (orange in Figure 3d). When the absorption coefficient tends to zero, no effect can be seen since charges are generated equally throughout the perovskite layer.

These results demonstrate why the distance between the photogenerated carriers and the space-charge region is important in PSCs, an effect that has been observed previously by other authors [69]. Moreover, these results show that doping is key for achieving high efficiencies when materials with high absorption coefficients are used, assuming that the charge's diffusion lengths are not at least an order of magnitude larger than the film themselves (as is the case in Si and GaAs).
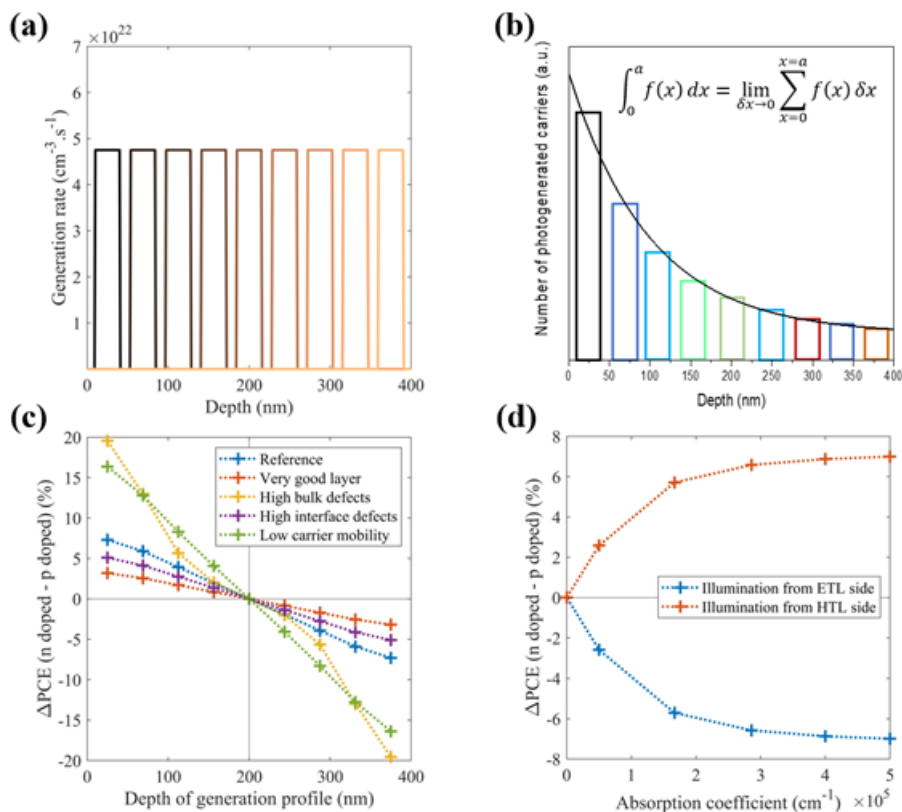
Figure 3: (a) Square (30nm wide) photogenerated carrier distributions used for the simulations. Depth scale starts from HTL interface (0nm) to the ETL interface (400nm) (b) Diagrammatic explanation for how physically realistic carrier distributions can be modelled with square functions. (c) Resulting power difference between p-type perovskite ($Na=10^{17}$ cm^{-3}) and n-type perovskite ($Nd=10^{17}$ cm^{-3}) when using the square functions in (a) as the photogenerated carrier profiles. HTL is at the front (left) and ETL is at the back (right). Several configurations of defects and mobilities are simulated. (d) Power difference between p-type perovskite ($NA=10^{17}$ cm^{-3}) and n-type perovskite ($ND=10^{17}$ cm^{-3}) as a function of absorption coefficient for both n-i-p and p-i-n configurations. Associated data is in supporting information Tables S2 and S3, Figures S8 and S9.

Bulk and interface recombination In the previous section we showed how an optimal doping level can arise due to non-uniform photogeneration, with most carriers being created near the front side of the perovskite layer. Moreover, electron-hole pair separation can also be hindered if the doping localises the band bending at the back interface (see Figures S6 and S7).

In this context, charge carrier transport and recombination play key roles. To study this further, we investigated the effect of changing defect densities which correspond to neutral recombination centres inside the bulk of the perovskite layer and at the interfaces with the charge transport layers (details can be found in Table S3, Figures S10 to S14).

Figure 3c shows that the configuration with the best transport properties (low bulk and interface defects, red) not only has the lowest PCE difference between heavily n-doped and p-doped cells, but also the lowest dependence on generation depth. Conversely, having a high defect density of 10^{17} cm^{-3} in the perovskite layer (yellow) leads to large variations, which are more sensitive to generation location, in optimal doping level. For instance, if the generation is on the HTL side (low depth values) and the doping is p-type, the separation of carriers relies almost exclusively on diffusion, meaning that electrons must diffuse across the width of the absorber to reach the ETL. Naturally, a perovskite layer with high defect density is highly detrimental in this case. Similarly, when lower mobilities are considered (both electron and hole mobility lowered to 0.1 cm^{2}V^{-1}s^{-1}), a similarly strong dependence on doping and generation profile is observed.

To probe the impact of bulk perovskite defects on optimal doping level, we simulated the cells in Figure 2 with both low (10^{10} cm^{-3}) and high (10^{17} cm^{-3}) defect densities. Independent of defect density, devices illuminated from the ETL side had an optimal p-doping level and those illuminated from the HTL side an optimal n-doping level. Furthermore, an intrinsic layer was preferred when generation rate was constant irrespective of the defect density. Across all three cases, increasing the bulk defect density reinforced the benefits of doping because it increased the probability of recombination, negatively impacting transport properties and the effective diffusion length of photogenerated carriers. This exacerbates the difficulty in extracting the minority carriers. Doping level maps of JSC, VOC, and FF can be found in Figures S11 to S13.

We also investigated the role that interface defects between the perovskite and the charge transport layers played in determining the optimal doping level. We found that the optimal doping level was conserved irrespective of the interfacial recombination rate (see Figure S14), although there was a slight decrease in PCE at high dopant densities due to the increased recombination.

The impact of asymmetrical carrier mobilities   Until now, equal electron and hole mobilities have been considered in the perovskite layer, however in real devices hole mobilities tend to be lower than their electron counterparts. Moreover, we found that the value of charge carrier mobilities was critical in determining the optimum doping level. In two cases, when the ratio of the charge carrier mobilities is very small or large, the optimal

doping level dependence on photogenerated carrier profile can disappear completely. To investigate the effect of having asymmetric electron-hole mobilities, simulations were carried out using a constant electron mobility of 1 cm^{2}V^{-1}s^{-1}, while hole mobility was varied an order of magnitude from 1 to 0.1 cm^{2}V^{-1}s^{-1}.

Figure 4a, similarly to Figure 3d, shows that the more carriers that are generated close to the edge of the absorber layer, the more it becomes advantageous to be doped. This trend is persistent throughout all mobility conditions. However, as hole mobility is decreased, the PCE difference between n- and p-doped devices are downshifted. This leads to a limiting case where for a given absorption coefficient and low enough hole mobility it is always preferable for the perovskite to be p-doped since this makes the holes the majority carriers and therefore improves their transport.

Another interesting finding is that for each set of mobilities there exists an absorption coefficient where there is no optimal doping level. The perovskite layer thickness, which is constant in this study, is also likely to play a role in this effect. For example, when the hole mobility is 0.1 cm^{2}V^{-1}s^{-1} no doping type is preferred when absorption coefficient is approximately 1.2×10^5 cm^{-1}. This demonstrates an inner balance occurring between carrier mobility and photogeneration profile which can lead to several physical regimes depending on whether carrier mobilities are comparable or not.

Figure 4b identifies the separate physical regimes determined by carrier mobilities. This figure was obtained by combining several doping maps with different device structures and bulk defect densities (see Figure S15). We find that when there is a very strong mobility asymmetry there are regions where it is always better to have a certain doping type. On the other hand, in the central area where both mobilities are comparable, the optimal doping level depends on the profile of the photogenerated carriers. Figure 4b also shows two different bulk defect densities in the perovskite layer. As reported in the previous section, bulk defect densities increase the sensitivity of PCE to doping. This manifests itself in Figure 4c as an expansion of the area where doping level is dependent on photogenerated carrier profile, meaning that higher asymmetries in mobilities must be reached before doping level is insensitive to device configuration.
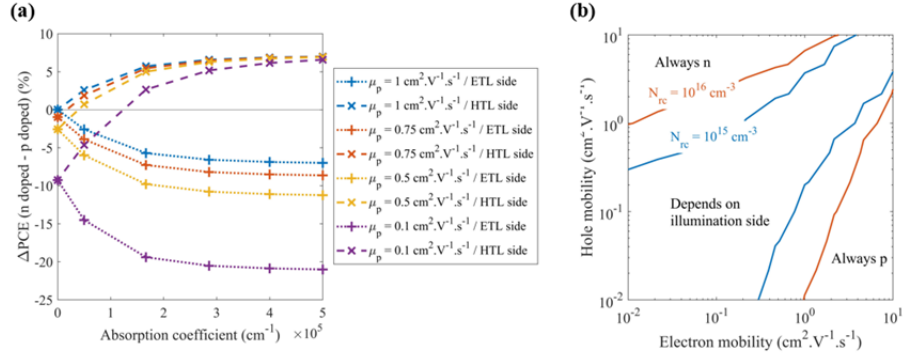
Figure 4: (a) Difference in PCE between simulated cells with a p-type perovskite (Na=10^{17} cm^{-3}) and n-type perovskite (Nd=10^{17} cm^{-3}) as a function of perovskite absorption coefficient. n-i-p configuration corresponds to the doted lines and plus signs, wheras p-i-n configuration corresponds to dashed lines and x signs. (b) The three limiting cases defined by carrier mobilities when diffusion lengths are not at least an order of magnitude larger than the perovskite layer. Associated data in supporting information Figure S15. When there is a large difference between carrier mobilities, it is best for the carrier with the reduced mobility to be made the majority carrier. This is independent of the device architecture used. However, when mobilities are comparable, whether p-doping or n-doping should be used depends on device architecture and illumination conditions. Increasing bulk defect density in the perovskite layer from 10^{15} cm^{-3} to 10^{16} cm^{-3} results in a broadening of this region.

2.3.3 Methods and insights for electronically doping PSCs:

In order to exploit the results presented so far, this section explores the available experimental techniques for doping halide perovskites. Here we review different approaches for electronically doping perovskites, in order to obtain elevated numbers of free charges in the material. These include the intrinsic (i.e. non-stochiometric films) and extrinsic (i.e. via impurities) doping of halide perovskites as well as remote doping through charge transfer from adjacent layers.

Intrinsic doping of perovskites has been explored from a theoretical point of view [14–17] and reported experimentally [21–27]. Density functional theory (DFT) calculations indicate the possibility of making a range of compositions more or less p- or n-type by controlling growth conditions. Such compositions include MAPbI$_3$ [14], FAPbI$_3$ [15], MAPbBr$_3$ [16] and MASnI$_3$ [17]. In the case of FAPbI$_3$ and MAPbI$_3$ it should be possible to produce either n- or p-type films by growing them in Pb-rich or Pb-poor conditions respectively [14, 15], however MAPbBr$_3$ and MASnI$_3$ films tend

towards being p-type [16, 17].

In terms of the experimental evidence, several studies report p-type behaviour in tin-based perovskites which is attributed to the propensity of tin to oxidise [21, 22, 27]. Many studies have also shown a p-type to n-type phase transition by changing the stoichiometry of the precursor and several perovskite homojunctions have been fabricated using this property [42, 43]. Wang et al. found that changing the MAI to PbI_2 ratio in the $MAPbI_3$ precursor solution from 0.3 to 1.7 resulted in p-type or n-type films with carrier concentrations of up to 4×10^{16} cm^{-3} holes and 3.5×10^{18} cm^{-3} electrons respectively [23]. Su et al. reported similar findings for $MAPbBr_3$ [25]. There is also evidence that suggests there exists the possibility of intrinsically doping films after their synthesis. Zohar et al. carried out a post-processing treatment of $MAPbI_3$ using I2 vapour [24]. They found that the post-processing method increased conductivity by an order of magnitude, altered the diffusion lengths of the carriers and led to a 150mV increase in the work function which they attribute to the film becoming p-type. Furthermore, Song et al. exploited the volatile nature of MA in order to prepare more or less n-type films by controlling the annealing temperature [26].

Similarly to intrinsic doping, extrinsic doping has been explored from both theoretical [16, 18–20] and experimental [28–37] points of view. First-principles calculations suggest that $MAPbI_3$ can be made p-type or n-type depending on the group that the dopant belongs to and the position it occupies in the lattice [18]. That said, while the production of p-type $MAPbI_3$ via doping with group IA, IB and VIA elements under I-rich/Pb-poor growth should be straight forward, n-type doping requires non-equilibrium growth conditions [18]. It is noteworthy that $MAPbBr_3$ is much more difficult to dope extrinsically since intrinsic defects such as Pb and Br vacancies that compensate extrinsic doping are very stable [16]. In terms of inorganic perovskites, some DFT calculations support the claim that p- or n-type $CsPbI_3$ can be achieved through group IIIA and VA doping [19], however intrinsic defects were not considered in this study and they may play an important role [74].

In a number of experiments a range of elements have been claimed to act as dopants or acceptors in perovskites [74]. This may not be so straightforward as appears and care should be taken when adding extrinsic dopants into the precursor solution because it is possible to inadvertently change the crystallization kinetics, surface chemistry, and/or the AX/PbX_2 ratio which directly impacts the growth conditions of intrinsic defects. Senocrate et al. reported on the p-type behaviour of halide perovskites when interacting with oxygen which they attributed to the O_2 substituting I$^-$ or sitting on interstitial sites [28]. Ag has also been proposed as an acceptor dopant with p-type $MAPbI_3$ [34] and $CsPbBr_3$ [35] being reported. Several results also suggest that the hole density in p-type $MAPbI_3$ can be controlled through the inclusion of NaI and RbI in the precursor solution [29, 30]. With reference

to n-type doping, Huang et al. varied the electron density in MAPbI$_3$ from 7.2×10^{14} cm^{-3} up to 8.3×10^{16} cm^{-3} by substituting Pb^{2+} with Sb^{3+} [31]. In an alternative approach Abdelhady et al. and Meng et al. increased carrier density up to 2×10^{16} cm^{-3} by doping with MAPbBr$_3$ with Bi^{3+} [32, 33]. Li has also shown potential, with n-type MAPbI$_3$ [36] and CsPbBr$_3$ [37] being reported. In fact, it is plausible that many reported PSCs have unknowingly been doped with Li since it is often used to dope the spiro-OMeTAD layer and it may be able to diffuse into the perovskite from the HTL [75].

Several groups have reported an apparent substrate-dependent shift in the Fermi level position in the perovskite film which could be associated with charge transfer or remote doping [38–41]. The fact that changing the doping of a substrate can alter the Fermi level position deep in the bulk of MAPbI$_3$ films, which are grown on top, suggests a low intrinsic carrier density in the perovskite film [44, 76]. Similar effects were observed for triple-cation lead bromide films on a range of substrates, for which the work function of the halide perovskite was monotonically decreasing as a function of the substrate's work function [41]. Noel et al. took a different approach, pre-treating the substrate with a fluorinated ionic liquid to make the perovskite n-type [77]. These results highlight the potential for using substrates as a means of controlling the band alignment in PSCs.

Molecular doping, i.e. the transfer of charge between an organic molecular species and an adjacent semiconductor, has also developed into a significant field of study for the doping of perovskites [78–84]. For molecular doping to work, the lowest unoccupied molecular orbital (LUMO) or highest occupied molecular orbital (HOMO) of the dopant must be above the conduction band or below the valence band of the perovskite for n- or p-doping respectively [74].

An important factor to consider when implementing these techniques is the effect that electronical doping can have on device stability. In some cases, improving the doping level of the perovskite can improve lifespan of the device [47] however this is not always the case [85]. To our best knowledge, there is no clear consensus on the relationship between large families of electronic doping techniques and device stability. However, this knowledge, in combination with the findings presented here, could be invaluable to some device makers. For this reason, we highlight this as an area which merits further investigation.

2.3.4 Conclusion:

In this work we analyse the processes driving an optimal doping level in PSCs and provide tools for improving devices. Optimal doping levels are shown to originate in the properties of the perovskite layer itself, due to the relatively low carrier mobilities and high absorption coefficients of halide perovskites. Varying the type of doping modifies the nature of the space charge region

created at the charge transport layer/perovskite junction, which can hinder or promote the extraction of charge. The high absorption coefficients of halide perovskites lead to a strong localisation of photogenerated carriers on the front side of the absorber layer, which is why the choice of an n-i-p or p-i-n structure generally dictates whether p-type or n-type doping is optimal. This effect has been overlooked in PSCs because in other semiconductors commonly used in photovoltaic applications, such as Si and GaAs, charge mobilities are normally large enough that diffusion lengths are orders of magnitude longer than the absorber thickness. This is not the case for halide perovskites, and it leads to a lower charge extraction efficiency.

We find that the relationship between electron and hole carrier mobilities has a critical impact on the optimal doping level. Specifically, we find that there are four regimes depending on values of electron and hole mobilities. Firstly, when they are both high enough, so that charge carrier diffusion lengths are much larger than the absorber thickness, optimal doping level is insensitive to device structure. However, the remaining three cases, which are more pronounced in PSCs due to the lower mobilities, occur when electron mobility is either much larger, equal to, or much smaller than hole mobility. In the cases where mobilities are very different, devices will perform best when the majority carriers are the ones with lower mobilities. However, in the case where mobilities are comparable, the optimal doping level is a function of device architecture, namely whether the ETL and HTL are on the front- and back-side or vice versa. Having established the profile of photogenerated carriers as the source of the optimal doping level, we investigate the impact of perovskite properties on said effect. Bulk defects in the perovskite are shown to be important in exaggerating the effect since they impede charge transport. Absorber thickness is also important because the optimal doping levels originate from the fact that diffusion lengths are on the order of the film thickness. Lastly, any increases in absorption coefficient will also exacerbate the impact of doping since it will increase the localisation of photogenerated carriers.

For these reasons, device makers should be aware that PCE may be fundamentally limited for a given device configuration depending on the deposition conditions and perovskite composition used. For example, this should be considered when using non-stoichiometric growth conditions or perovskites with a tendency to self-dope, such as tin-based ones [21, 22, 27]. The results presented here contribute to the development of a better understanding of electronic doping in PSCs as well as provide avenues of research for the development of future high-performance devices.

2.3.5 Acknowledgments:

Bibliography

[1] A. Kojima, K. Teshima, Y. Shirai, and T. Miyasaka, "Organometal halide perovskites as visible-light sensitizers for photovoltaic cells," *Journal of the American Chemical Society*, vol. 131, pp. 6050–6051, 2009. First perovskite solar cell.

[2] National Renewable Energy Laboratory, "Best research-cell efficiency chart — photovoltaic research," 2023.

[3] H. J. Snaith, "Perovskites: The emergence of a new era for low-cost, high-efficiency solar cells," *Journal of Physical Chemistry Letters*, vol. 4, pp. 3623–3630, 11 2013.

[4] D. R. Ceratti, Y. Rakita, L. Cremonesi, R. Tenne, V. Kalchenko, M. Elbaum, D. Oron, M. A. C. Potenza, G. Hodes, and D. Cahen, "Self-healing inside apbbr3 halide perovskite crystals," *Advanced Materials*, vol. 30, p. 1706273, 3 2018.

[5] D. R. Ceratti, A. V. Cohen, R. Tenne, Y. Rakita, L. Snarski, N. P. Jasti, L. Cremonesi, R. Cohen, M. Weitman, I. Rosenhek-Goldian, I. Kaplan-Ashiri, T. Bendikov, V. Kalchenko, M. Elbaum, M. A. Potenza, L. Kronik, G. Hodes, and D. Cahen, "The pursuit of stability in halide perovskites: The monovalent cation and the key for surface and bulk self-healing," *Materials Horizons*, vol. 8, pp. 1570–1586, 2021.

[6] D. R. Ceratti, R. Tenne, A. Bartezzaghi, L. Cremonesi, L. Segev, V. Kalchenko, D. Oron, M. A. C. Potenza, G. Hodes, and D. Cahen, "Self-healing and light-soaking in mapbi 3 : the effect of h 2 o," *Advanced Materials*, 6 2022.

[7] S. Aharon, D. R. Ceratti, N. P. Jasti, L. Cremonesi, Y. Feldman, M. A. C. Potenza, G. Hodes, and D. Cahen, "2d pb-halide perovskites can self-heal photodamage better than 3d ones," *Advanced Functional Materials*, vol. 32, 2022.

[8] A. Miyata, A. Mitioglu, P. Plochocka, O. Portugall, J. T. W. Wang, S. D. Stranks, H. J. Snaith, and R. J. Nicholas, "Direct measurement of the exciton binding energy and effective masses for charge carriers in organic-inorganic tri-halide perovskites," *Nature Physics*, vol. 11, pp. 582–587, 2015.

[9] V. D'Innocenzo, G. Grancini, M. J. Alcocer, A. R. S. Kandada, S. D. Stranks, M. M. Lee, G. Lanzani, H. J. Snaith, and A. Petrozza, "Excitons versus free charges in organo-lead tri-halide perovskites," *Nature Communications*, vol. 5, 4 2014.

[10] A. Musiienko, D. R. Ceratti, J. Pipek, M. Brynza, H. Elhadidy, E. Belas, M. Betušiak, G. Delport, and P. Praus, "Defects in hybrid perovskites: The secret of efficient charge transport," *Advanced Functional Materials*, vol. 31, 2021.

[11] M. J. P. Alcocer, T. Leijtens, L. M. Herz, A. Petrozza, and H. J. Snaith, "Electron-hole diffusion lengths exceeding trihalide perovskite absorber," *Science*, vol. 342, pp. 341–344, 2013.

[12] G. Xing, N. Mathews, S. Sun, S. S. Lim, Y. M. Lam, M. Gratzel, S. Mhaisalkar, and T. C. Sum, "Long-range balanced electron-and hole-transport lengths in organic-inorganic ch3nh3pbi3," *Science*, vol. 342, pp. 344–347, 10 2013.

[13] L. M. Herz, "Charge-carrier mobilities in metal halide perovskites: Fundamental mechanisms and limits," *ACS Energy Letters*, vol. 2, pp. 1539–1548, 7 2017.

[14] W. J. Yin, T. Shi, and Y. Yan, "Unusual defect physics in ch3nh3pbi3 perovskite solar cell absorber," *Applied Physics Letters*, vol. 104, p. 63903, 10 2014.

[15] N. Liu and C. Y. Yam, "First-principles study of intrinsic defects in formamidinium lead triiodide perovskite solar cell absorbers," *Physical Chemistry Chemical Physics*, vol. 20, pp. 6800–6804, 2018.

[16] T. Shi, W. J. Yin, F. Hong, K. Zhu, and Y. Yan, "Unipolar self-doping behavior in perovskite ch3nh3pbbr3," *Applied Physics Letters*, vol. 106, 2015.

[17] D. Meggiolaro, D. Ricciarelli, A. A. Alasmari, F. A. Alasmary, and F. D. Angelis, "Tin versus lead redox chemistry modulates charge trapping and self-doping in tin/lead iodide perovskites," *Journal of Physical Chemistry Letters*, vol. 11, pp. 3546–3556, 2020.

[18] T. Shi, W. jian Yin, and Y. Yan, "Predictions for p-type ch 3 nh 3 pbi 3 perovskites," *The Journal of Physical Chemistry C*, vol. 118, pp. 25350–25354, 11 2014.

[19] Y. Chen, H. Jing, F. Ling, W. Kang, T. Zhou, X. Liu, W. Zeng, Y. Zhang, L. Qi, L. Fang, and M. Zhou, "Tuning the electronic structures of all-inorganic lead halide perovskite cspbi3 via heterovalent doping: A first-principles investigation," *Chemical Physics Letters*, vol. 722, pp. 90–95, 2019.

[20] W. Chen, H. Chen, G. Xu, R. Xue, S. Wang, Y. Li, and Y. Li, "Precise control of crystal growth for highly efficient cspbi2br perovskite solar cells," *Joule*, vol. 3, pp. 191–204, 2019.

[21] Y. Takahashi, H. Hasegawa, Y. Takahashi, and T. Inabe, "Hall mobility in tin iodide perovskite ch3nh3sni 3: Evidence for a doped semiconductor," *Journal of Solid State Chemistry*, vol. 205, pp. 39–43, 2013.

[22] M. A. Haque, J. Troughton, and D. Baran, "Processing-performance evolution of perovskite solar cells: From large grain polycrystalline films to single crystals," *Advanced Energy Materials*, vol. 10, p. 1902762, 4 2020.

[23] Q. Wang, Y. Shao, H. Xie, L. Lyu, X. Liu, Y. Gao, and J. Huang, "Qualifying composition dependent p and n self-doping in ch3nh3pbi3," *Applied Physics Letters*, vol. 105, 2014.

[24] A. Zohar, I. Levine, S. Gupta, O. Davidson, D. Azulay, O. Millo, I. Balberg, G. Hodes, and D. Cahen, "What is the mechanism of mapbi3 p-doping by i2? insights from optoelectronic properties," *ACS Energy Letters*, vol. 2, pp. 2408–2414, 2017.

[25] Z. Su, Y. Chen, X. Li, S. Wang, and Y. Xiao, "The modulation of opto-electronic properties of ch3nh3pbbr3 crystal," *Journal of Materials Science: Materials in Electronics*, vol. 28, pp. 11053–11058, 2017.

[26] D. Song, P. Cui, T. Wang, D. Wei, M. Li, F. Cao, X. Yue, P. Fu, Y. Li, Y. He, B. Jiang, and M. Trevor, "Managing carrier lifetime and doping property of lead halide perovskite by postannealing processes for highly efficient perovskite solar cells," *Journal of Physical Chemistry C*, vol. 119, pp. 22812–22819, 2015.

[27] T. Liu, X. Zhao, J. Li, Z. Liu, F. Liscio, S. Milita, B. C. Schroeder, and O. Fenwick, "Enhanced control of self-doping in halide perovskites for improved thermoelectric performance," *Nature Communications*, vol. 10, pp. 1–9, 2019.

[28] A. Senocrate, T. Acartürk, G. Y. Kim, R. Merkle, U. Starke, M. Grätzel, and J. Maier, "Interaction of oxygen with halide perovskites," *Journal of Materials Chemistry A*, vol. 6, pp. 10847–10855, 2018.

[29] Y. Yang, X. Zou, Y. Pei, X. Bai, W. Jin, and D. Chen, "Effect of doping of nai monovalent cation halide on the structural, morphological, optical and optoelectronic properties of mapbi3 perovskite," *Journal of Materials Science: Materials in Electronics*, vol. 29, pp. 205–210, 2018.

[30] X. Bai, X. Zou, J. Zhu, Y. Pei, Y. Yang, W. Jin, and D. Chen, "Effect of rb doping on modulating grain shape and semiconductor properties of mapbi3 perovskite layer," *Materials Letters*, vol. 211, pp. 328–330, 2018.

[31] L. Huang, S. Bu, D. Zhang, R. Peng, Q. Wei, Z. Ge, and J. Zhang, "Schottky/p-n cascade heterojunction constructed by intentional n-type doping perovskite toward efficient electron layer-free perovskite solar cells," *Solar RRL*, vol. 3, pp. 1–13, 2019.

[32] A. L. Abdelhady, M. I. Saidaminov, B. Murali, V. Adinolfi, O. Voznyy, K. Katsiev, E. Alarousu, R. Comin, I. Dursun, L. Sinatra, E. H. Sargent, O. F. Mohammed, and O. M. Bakr, "Heterovalent dopant incorporation for bandgap and type engineering of perovskite crystals," *Journal of Physical Chemistry Letters*, vol. 7, pp. 295–301, 2016.

[33] R. Meng, G. Wu, J. Zhou, H. Zhou, H. Fang, M. A. Loi, and Y. Zhang, "Understanding the impact of bismuth heterovalent doping on the structural and photophysical properties of ch 3 nh 3 pbbr 3 halide perovskite crystals with near-ir photoluminescence," *Chemistry - A European Journal*, vol. 25, pp. 5480–5488, 2019.

[34] Q. Chen, L. Chen, F. Ye, T. Zhao, F. Tang, A. Rajagopal, Z. Jiang, S. Jiang, A. K. Jen, Y. Xie, J. Cai, and L. Chen, "Ag-incorporated organic-inorganic perovskite films and planar heterojunction solar cells," *Nano Letters*, vol. 17, pp. 3231–3237, 2017.

[35] S. Zhou, Y. Ma, G. Zhou, X. Xu, M. Qin, Y. Li, Y. J. Hsu, H. Hu, G. Li, N. Zhao, J. Xu, and X. Lu, "Ag-doped halide perovskite nanocrystals for tunable band structure and efficient charge transport," *ACS Energy Letters*, vol. 4, pp. 534–541, 2019.

[36] Z. Fang, H. He, L. Gan, J. Li, and Z. Ye, "Understanding the role of lithium doping in reducing nonradiative loss in lead halide perovskites," *Advanced Science*, vol. 5, pp. 1–6, 2018.

[37] Q. Jiang, M. Chen, J. Li, M. Wang, X. Zeng, T. Besara, J. Lu, Y. Xin, X. Shan, B. Pan, C. Wang, S. Lin, T. Siegrist, Q. Xiao, and Z. Yu, "Electrochemical doping of halide perovskites with ion intercalation," *ACS Nano*, vol. 11, pp. 1073–1079, 2017.

[38] P. Schulz, L. L. Whittaker-Brooks, B. A. Macleod, D. C. Olson, Y. L. Loo, and A. Kahn, "Electronic level alignment in inverted organometal perovskite solar cells," *Advanced Materials Interfaces*, vol. 2, 2015.

[39] S. Olthof and K. Meerholz, "Substrate-dependent electronic structure and film formation of mapbi 3 perovskites," *Scientific Reports*, vol. 7, pp. 1–10, 2017.

[40] E. M. Miller, Y. Zhao, C. C. Mercado, S. K. Saha, J. M. Luther, K. Zhu, V. Stevanović, C. L. Perkins, and J. V. D. Lagemaat, "Substrate-controlled band positions in ch3nh3pbi3 perovskite films," *Physical Chemistry Chemical Physics*, vol. 16, pp. 22122–22130, 2014.

[41] A. Zohar, M. Kulbak, I. Levine, G. Hodes, A. Kahn, and D. Cahen, "What limits the open-circuit voltage of bromide perovskite-based solar cells?," *ACS Energy Letters*, vol. 4, pp. 1–7, 2019.

[42] B. Dänekamp, C. Müller, M. Sendner, P. P. Boix, M. Sessolo, R. Lovrincic, and H. J. Bolink, "Perovskite-perovskite homojunctions via compositional doping," *Journal of Physical Chemistry Letters*, vol. 9, pp. 2770–2775, 2018.

[43] P. Cui, D. Wei, J. Ji, H. Huang, E. Jia, S. Dou, T. Wang, W. Wang, and M. Li, "Planar p–n homojunction perovskite solar cells with efficiency exceeding 21.3%," *Nature Energy*, vol. 4, pp. 150–159, 2019.

[44] D. Regaldo, A. Bojar, S. P. Dunfield, P. Lopez-Varo, M. Frégnaux, V. Dufoulon, S. T. Zhang, J. Alvarez, J. J. Berry, J. B. Puel, P. Schulz, and J. P. Kleider, "On the equilibrium electrostatic potential and light-induced charge redistribution in halide perovskite structures," *Progress in Photovoltaics: Research and Applications*, 2021.

[45] F. Peña-Camargo, J. Thiesbrummel, H. Hempel, A. Musiienko, V. M. L. Corre, J. Diekmann, J. Warby, T. Unold, F. Lang, D. Neher, and M. Stolterfoht, "Revealing the doping density in perovskite solar cells and its impact on device performance," *Applied Physics Reviews*, vol. 9, 2022.

[46] P. Lopez-Varo, J. A. Jiménez-Tejada, M. García-Rosell, S. Ravishankar, G. Garcia-Belmonte, J. Bisquert, and O. Almora, "Device physics of hybrid perovskite solar cells: Theory and experiment," *Advanced Energy Materials*, vol. 8, 5 2018.

[47] Q. Jiang, J. Tong, Y. Xian, R. A. Kerner, S. P. Dunfield, C. Xiao, R. A. Scheidt, D. Kuciauskas, X. Wang, M. P. Hautzinger, R. Tirawat, M. C. Beard, D. P. Fenning, J. J. Berry, B. W. Larson, Y. Yan, and K. Zhu, "Surface reaction for efficient and stable inverted perovskite solar cells," *Nature*, vol. 611, pp. 278–283, 2022.

[48] B. Das, I. Aguilera, U. Rau, and T. Kirchartz, "Effect of doping, photodoping, and bandgap variation on the performance of perovskite solar cells," *Advanced Optical Materials*, vol. 2101947, 2022.

[49] M. Burgelman, P. Nollet, and S. Degrave, "Modelling polycrystalline semiconductor solar cells," *Thin Solid Films*, vol. 361, pp. 527–532, 2 2000.

[50] M. Burgelman, K. Decock, S. Khelifi, and A. Abass, "Advanced electrical simulation of thin film solar cells," *Thin Solid Films*, vol. 535, pp. 296–301, 2013.

[51] J. Diekmann, P. Caprioglio, M. H. Futscher, V. M. L. Corre, S. Reichert, F. Jaiser, M. Arvind, L. P. Toro, E. Gutierrez-Partida, F. Peña-Camargo, C. Deibel, B. Ehrler, T. Unold, T. Kirchartz, D. Neher, and M. Stolterfoht, "Pathways toward 30the role of mobile ions," *Solar RRL*, vol. 5, 2021.

[52] E. Raza, Z. Ahmad, F. Aziz, M. Asif, A. Ahmed, K. Riaz, J. Bhadra, and N. J. Al-Thani, "Numerical simulation analysis towards the effect of charge transport layers electrical properties on cesium based ternary cation perovskite solar cells performance," *Solar Energy*, vol. 225, pp. 842–850, 2021.

[53] T. Hellmann, M. Wussler, C. Das, R. Dachauer, I. El-Helaly, C. Mortan, T. Mayer, and W. Jaegermann, "The difference in electronic structure of mapi and masi perovskites and its effect on the interface alignment to the htms spiro-meotad and cui," *Journal of Materials Chemistry C*, vol. 7, pp. 5324–5332, 2019.

[54] E. Karimi and S. M. Ghorashi, "Investigation of the influence of different hole-transporting materials on the performance of perovskite solar cells," *Optik*, vol. 130, pp. 650–658, 2017.

[55] U. Mandadapu, S. Vedanayakam, K. Thyagarajan, M. Reddy, and B. Jagadeeshbabu, "Design and simulation of high efficiency tin halide perovskite solar cell," *International Journal of Renewable Energy Research*, 2017.

[56] C. Motta, F. El-Mellouhi, and S. Sanvito, "Charge carrier mobility in hybrid halide perovskites," *Scientific Reports*, vol. 5, 2015.

[57] C. Wehrenfennig, G. E. Eperon, M. B. Johnston, H. J. Snaith, L. M. Herz, C. Wehrenfennig, G. E. Eperon, M. B. Johnston, H. J. Snaith, and L. M. Herz, "High charge carrier mobilities and lifetimes in organolead trihalide perovskites," *Advanced Materials*, vol. 26, pp. 1584–1589, 3 2014.

[58] G. Xosrovashvili and N. E. Gorji, "Numerical analysis of tio2/cu2znsns4 nanostructured pv using scaps-1d," *Journal of Modern Optics*, vol. 60, pp. 936–940, 2013.

[59] T. Minemoto and M. Murata, "Device modeling of perovskite solar cells based on structural similarity with thin film inorganic semiconductor solar cells," *Journal of Applied Physics*, vol. 116, 2014.

[60] K. Kalyanasundaram, *Dye-sensitized Solar Cells (Fundamental Sciences: Chemistry)*. EPFL Press, 2010.

[61] S. J. Fonash, *Solar Cell Device Physics (2nd Edition)*. Academic Press, 2010.

[62] L. Schmidt-Mende and M. Grätzel, "Tio2 pore-filling and its effect on the efficiency of solid-state dye-sensitized solar cells," *Thin Solid Films*, vol. 500, pp. 296–301, 4 2006.

[63] Y. Raoui, H. Ez-Zahraouy, N. Tahiri, O. E. Bounagui, S. Ahmad, and S. Kazim, "Performance analysis of mapbi3 based perovskite solar cells employing diverse charge selective contacts: Simulation study," *Solar Energy*, vol. 193, pp. 948–955, 2019.

[64] P. K. Patel, "Device simulation of highly efficient eco-friendly ch3nh3sni3 perovskite solar cell," *Scientific Reports*, vol. 11, pp. 1–11, 2021.

[65] J. Jeong, M. Kim, J. Seo, H. Lu, P. Ahlawat, A. Mishra, Y. Yang, M. A. Hope, F. T. Eickemeyer, M. Kim, Y. J. Yoon, I. W. Choi, B. P. Darwich, S. J. Choi, Y. Jo, J. H. Lee, B. Walker, S. M. Zakeeruddin, L. Emsley, U. Rothlisberger, A. Hagfeldt, D. S. Kim, M. Grätzel, and J. Y. Kim, "Pseudo-halide anion engineering for α-fapbi3 perovskite solar cells," *Nature*, vol. 592, pp. 381–385, 2021.

[66] J. J. Yoo, G. Seo, M. R. Chua, T. G. Park, Y. Lu, F. Rotermund, Y. K. Kim, C. S. Moon, N. J. Jeon, J. P. Correa-Baena, V. Bulović, S. S. Shin, M. G. Bawendi, and J. Seo, "Efficient perovskite solar cells via improved carrier management," *Nature*, vol. 590, pp. 587–593, 2021.

[67] M. Kim, J. Jeong, H. Lu, T. K. Lee, F. T. Eickemeyer, Y. Liu, I. W. Choi, S. J. Choi, Y. Jo, H. B. Kim, S. I. Mo, Y. K. Kim, H. Lee, N. G. An, S. Cho, W. R. Tress, S. M. Zakeeruddin, A. Hagfeldt, J. Y. Kim, M. Grätzel, and D. S. Kim, "Conformal quantum dot-sno2 layers as electron transporters for efficient perovskite solar cells," *Science*, vol. 375, pp. 302–306, 2022.

[68] M. Saliba, T. Matsui, J. Y. Seo, K. Domanski, J. P. Correa-Baena, M. K. Nazeeruddin, S. M. Zakeeruddin, W. Tress, A. Abate, A. Hagfeldt, and M. Grätzel, "Cesium-containing triple cation perovskite solar cells: Improved stability, reproducibility and high efficiency," *Energy and Environmental Science*, vol. 9, pp. 1989–1997, 2016.

[69] X. Li, D. Bi, C. Yi, J. D. Décoppet, J. Luo, S. M. Zakeeruddin, A. Hagfeldt, and M. Grätzel, "A vacuum flash-assisted solution process for high-efficiency large-area perovskite solar cells," *Science*, vol. 353, pp. 58–62, 2016.

[70] P. Zhao, B. J. Kim, X. Ren, D. G. Lee, G. J. Bang, J. B. Jeon, W. B. Kim, and H. S. Jung, "Antisolvent with an ultrawide processing window for the one-step fabrication of efficient and large-area perovskite solar cells," *Advanced Materials*, vol. 30, 2018.

[71] S.-G. L. D. S. H. P. Nam-Gyu Zhang, Yong; Kim, "Bifacial stamping for high efficiency perovskite solar cells," *Energy and Environmental Science*, vol. 12, pp. 308–321, 2019.

[72] N. Ahn, D.-Y. Son, I.-H. Jang, S. M. Kang, M. Choi, and N. gyu Park, "Highly reproducible perovskite solar cells with average e ffi ciency of 18.3best e ffi ciency of 19.7iodide," *Journal of the American Chemical Society*, vol. 137, pp. 8696–8699, 2015.

[73] N. K. Noel, S. N. Habisreutinger, B. Wenger, M. T. Klug, T. H. Maximilian, M. B. Johnston, R. J. Nicholas, D. T. Moore, and H. J. Snaith, "A low viscosity, low boiling point, clean solvent system for the rapid crystallisation of highly specular perovskite films," *Energy & Environmental Science*, vol. 10, pp. 145–152, 2017.

[74] J. Euvrard, Y. Yan, and D. B. Mitzi, "Electrical doping in halide perovskites," *Nature Reviews Materials*, vol. 6, pp. 531–549, 2021.

[75] C. Xiao, F. Zhang, Z. Li, S. P. Harvey, X. Chen, K. Wang, C. S. Jiang, K. Zhu, and M. Al-Jassim, "Inhomogeneous doping of perovskite materials by dopants from hole-transport layer," *Matter*, vol. 2, pp. 261–272, 2020.

[76] S. P. Dunfield, A. Bojar, S. Cacovich, M. Frégnaux, T. Klein, R. Bramante, F. Zhang, D. Regaldo, V. Dufoulon, J. B. Puel, G. Teeter, J. M. Luther, M. Bouttemy, D. Nordlund, K. Zhu, D. T. Moore, M. F. van Hest, J. P. Kleider, J. J. Berry, and P. Schulz, "Carrier gradients and the role of charge selective contacts in lateral heterojunction all back contact perovskite solar cells," *Cell Reports Physical Science*, vol. 2, 2021.

[77] N. K. Noel, S. N. Habisreutinger, B. Wenger, Y. H. Lin, F. Zhang, J. B. Patel, A. Kahn, M. B. Johnston, and H. J. Snaith, "Elucidating the role of a tetrafluoroborate-based ionic liquid at the n-type oxide/perovskite interface," *Advanced Energy Materials*, vol. 10, 2020.

[78] N. R. V. H. N. M. L. Chabinyc E. E. Perry, J. G. Labram, "N-type surface doping of mapbi3 via charge transfer from small molecules," *Advanced Electronic Materials*, vol. 4, 2018.

[79] H. Chen, Y. Zhan, G. Xu, W. Chen, S. Wang, M. Zhang, Y. Li, and Y. Li, "Organic n-type molecule: Managing the electronic states of bulk

perovskite for high-performance photovoltaics," *Advanced Functional Materials*, vol. 30, 2020.

[80] N. K. Noel, S. N. Habisreutinger, A. Pellaroque, F. Pulvirenti, B. Wenger, F. Zhang, Y. H. Lin, O. G. Reid, J. Leisen, Y. Zhang, S. Barlow, S. R. Marder, A. Kahn, H. J. Snaith, C. B. Arnold, and B. P. Rand, "Interfacial charge-transfer doping of metal halide perovskites for high performance photovoltaics," *Energy and Environmental Science*, vol. 12, pp. 3063–3073, 2019.

[81] Arramel, H. Pan, A. Xie, S. Hou, X. Yin, C. S. Tang, N. T. Hoa, M. D. Birowosuto, H. Wang, C. Dang, A. Rusydi, A. T. Wee, and J. Wu, "Surface molecular doping of all-inorganic perovskite using zethrenes molecules," *Nano Research*, vol. 12, pp. 77–84, 2019.

[82] Q. Jiang, Z. Ni, G. Xu, Y. Lin, P. N. Rudd, R. Xue, Y. Li, Y. Li, Y. Gao, and J. Huang, "Interfacial molecular doping of metal halide perovskites for highly efficient solar cells," *Advanced Materials*, vol. 32, 2020.

[83] W. Q. Wu, Q. Wang, Y. Fang, Y. Shao, S. Tang, Y. Deng, H. Lu, Y. Liu, T. Li, Z. Yang, A. Gruverman, and J. Huang, "Molecular doping enabled scalable blading of efficient hole-transport-layer-free perovskite solar cells," *Nature Communications*, vol. 9, pp. 1–8, 2018.

[84] E. A. Gaulding, J. Hao, H. S. Kang, E. M. Miller, S. N. Habisreutinger, Q. Zhao, A. Hazarika, P. C. Sercel, J. M. Luther, and J. L. Blackburn, "Conductivity tuning via doping with electron donating and withdrawing molecules in perovskite cspbi3 nanocrystal films," *Advanced Materials*, vol. 31, 2019.

[85] S. Tan, I. Yavuz, M. H. Weber, T. Huang, C. H. Chen, R. Wang, H. C. Wang, J. H. Ko, S. Nuryyeva, J. Xue, Y. Zhao, K. H. Wei, J. W. Lee, and Y. Yang, "Shallow iodine defects accelerate the degradation of α-phase formamidinium perovskite," *Joule*, vol. 4, pp. 2426–2442, 11 2020.

2.3.7   Supplementary Materials

Shedding light on electronically doped perovskites

Alexander W. Stewart[*1,2], Arthur Julien[2], Davide Regaldo[2], Philip Schulz[3], Bernabé Marí Soucase[1], Davide R. Ceratti[*3], Pilar Lopez Varo[*2]

[1] Universitat Politècnica de València, Camí de Vera, s/n, 46022 Valencia, Spain
[2] Insitute Photovoltaïque d'Ile de France, 18 Bd Thomas Gobert, 91120 Palaiseau, France
[3] CNRS, UMR 9006, IPVF, Institut Photovoltaïque d'Ile-de-France, 18 Boulevard Thomas Gobert, 91120 Palaiseau, France

[*] Alste5@doctor.upv.es [*] davide.ceratti@cnrs.fr [*] pilar.lopez-varo@ipvf.fr

Table 1: Summary of literature values and those used for simulations. The solar cells in Figure 1 were carried out using the bold values.

	MAPbI$_3$	(MA$_{0.17}$FA$_{0.83}$)$_{0.95}$ Cs$_{0.05}$PbBr$_{0.51}$I$_{2.49}$	TiO$_2$	Spiro-OMeTAD
Thickness (nm)	400	400	50	50
Bandgap (eV)	**1.5**[1–3]	**1.61**[4], 1.62 [5], 1.5 [6]	3.2[2,3,7], 3.26[8]	3[7], 2.9[3], 3.06[2,9]
Electron affinity (eV)	3.9[2], 4.17[1], 3.93[3]	3.79[4], 3.90[5], 4[6]	**3.9**[2,7], 4.22[1], 4[3]	**2.2**[3], 2.05[2,9], 2.45[7]
Relative permittivity	**30**[2,3], 6.5[1]	23, 64[5], 6.5[6]	9[2,7], 10[8], 100[3]	3[2,3,7,10]
Nc (cm^{-3})	**10^{18}**, 2.5×10^{20} [2,3], 2.2×10^{15} [11]	**10^{19}** [5], 1.66×10^{19}[6]	10^{21} [3], 10^{19} [2], 10^{17} [8]	**10^{20}**, 2.8×10^{19} [2,12], 2.5×10^{20} [3]
Nv (cm^{-3})	**10^{18}**, 2.5×10^{20} [2,3], 2.2×10^{17} [11]	**10^{19}** [5], 5.41×10^{18}[6]	10^{21}, 6×10^{17}[8], 10^{19} [2], 2×10^{20} [3]	**10^{20}**, 10^{19} [2,12], 2.5×10^{20} [3]
Carriers thermal velocity (cm.s^{-1})	10^7 [2]	10^7	10^7 [2]	10^7 [2]
Electron mobility (cm^2.V^{-1}.s^{-1})	**1**, 7.5[13], 50[2,3], 10 [14]	**1**, 0.5[5], 50[6]	100[8], 20 [2,7], 6×10^{-3}[3]	**0.001**, 10^{-4} [2,15], 2.1×10^{-3} [3], 2×10^{-4}[7]
Hole mobility (cm^2.V^{-1}.s^{-1})	**1**, 2.5 [13], 50 [2,3], 10[14]	**1**[5], 50[6]	25[8], 10 [2,7], 6×10^{-3}[3]	**0.001**, 2×10^{-4} [2,7,15], 2.6×10^{-3} [3]
Donor density (cm^{-3})	10^{10} to 10^{17}	10^{10} to 10^{17}	10^{19}, 10^{17} [8], 10^{16} [2,7], 5.06×10^{19} [3]	0
Acceptor density (cm^{-3})	10^{10} to 10^{17}	10^{10} to 10^{17}	0	10^{18} [2,3]
Radiative recombination coefficient (cm^3.s^{-1})	5.3x10^{-11}	5.3x10^{-11}	5.3x10^{-11}	5.3x10^{-11}
Defect density in bulk (cm^{-3})	10^{15}	10^{15}	0	0
Defect density at ETL interface (cm^{-2})	10^{12}	10^{12}	0	0
Defect density at HTL interface (cm-2)	10^{12}	10^{12}	0	0

Note that in many cases, such as DOS or carrier mobilities, values found in the literature can span several orders of magnitude.
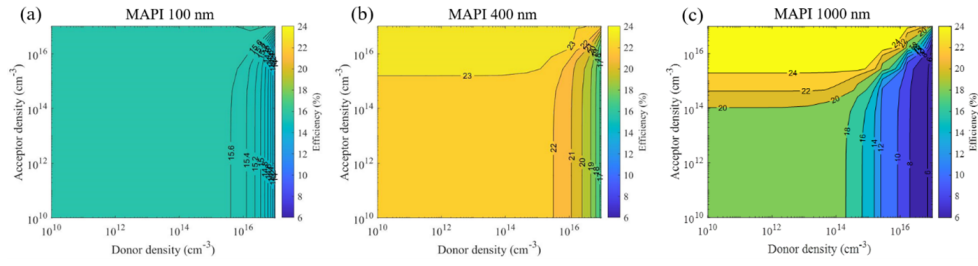
Figure S1: Impact of changing the perovskite layer's thickness on PCE as a function of dopant concentration. MAPbI3 thickness is (a) 100nm (b) 400nm (c) 1000nm.

Table 2: Parameters defining the hypothetical ETL and HTL in the solar cells associated to the results in Figure 2.

	ETL	HTL
Thickness (nm)	50	50
Bandgap (eV)	3	3
Electron affinity (eV)	3.79	2.4
Relative permittivity	10	10
N_c (cm^{-3})	10^{20}	10^{20}
N_v (cm^{-3})	10^{20}	10^{20}
Carriers thermal velocity (cm.s^{-1})	10^7	10^7
Electron mobility (cm^2.V^{-1}.s^{-1})	1	1
Hole mobility (cm^2.V^{-1}.s^{-1})	1	1
Donordensity (cm^{-3})	10^{18}	
Acceptordensity (cm^{-3})		10^{18}
Radiative recombination coefficient (cm^3.s^{-1})	5.3×10^{-11}	5.3×10^{-11}
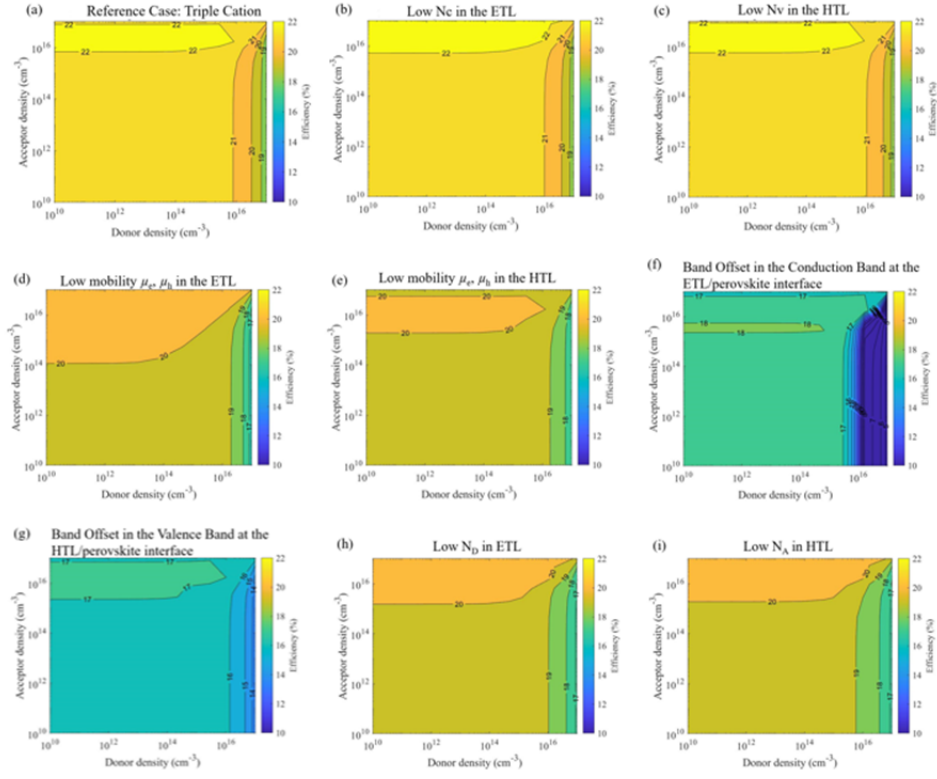
Figure S2: Impact of changing TL parameters from the reference n-i-p case (a) using the parameters in Table S1. The different changed parameters are the following: (1) Reduction of the conduction DOS (b) $N_c = 10^{18}$ cm^{-3} and valence DOS (c) $N_v = 10^{18}$ cm^{-3}. (2) Lower Mobility 10^{-5} cm^2/Vs in the ETL (d) and HTL (e). (3) Band offset of 0.4 eV in the conduction band (f) and valence band (g) at the ETL/perovskite interface and HTL/perovskite interface, respectively. (4) Lower doping concentration in the ETL (h) $N_D = 10^{16}$ cm^{-3} and HTL (i) $N_A = 10^{16}$ cm^{-3}.
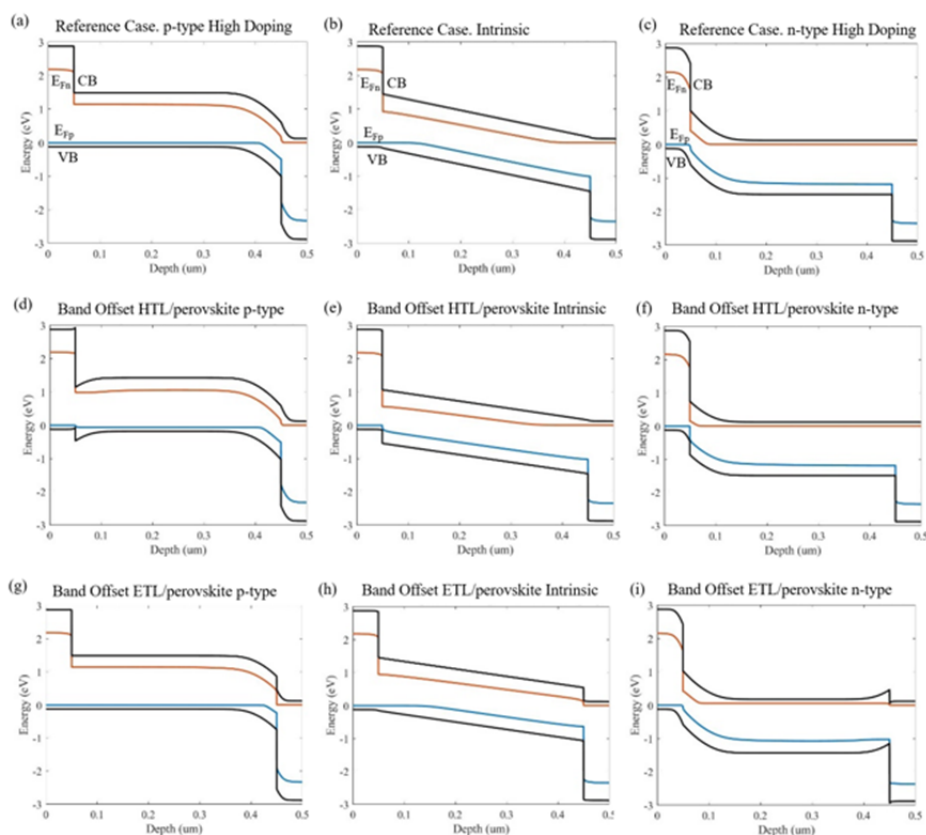
Figure S3: Band diagrams at short circuit condition corresponding to the study with the changed TL parameters. (a)-(c) Reference case Fig S1 (a). (d)-(f) Band offset HTL/perovskite Fig S1 (g). (g)-(h) Band offset ETL/perovskite Fig S1 (h).

In terms of performance, changing the ETL and HTL doping densities, mobilities and band offsets had an important impact on PCE (see Figure S2). Depending on the doping type, the band offset between the perovskite and the TL can either generate an additional electric field which opposes to the built-in one (Figure S3 (d) and (i)), or it can decrease the built-in field in the doped perovskite (Figure S3 (f) and (g)). Both conditions decrease the PCE, but the largest reduction is obtained if the band offset occurs at the back-side TL/perovskite interface (see Figure S3 (d)), where a Schottky barrier is created that hinders charge extraction.
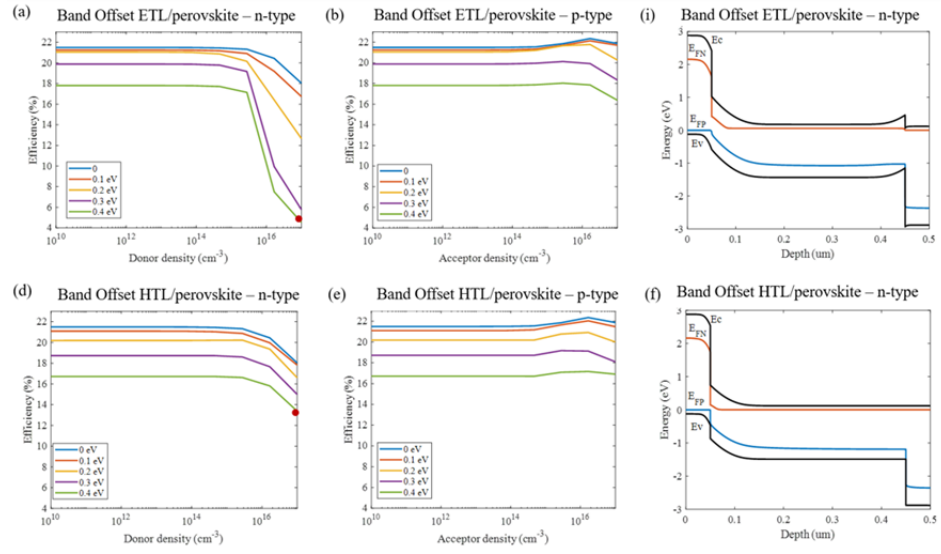
Figure S4: Efficiency of triple-cation based perovskite solar cell modifying the band offset of the ETL/perovskite (a-b) and HTL/perovskite (d-e) interfaces for different donor and acceptor dopant densities on the perovskite. (c) (f) Energy Diagrams for the worst scenario of the Figures (a-b) and (d-e), respectively (red point). The worst scenario is when the perovskite is highly n-type and the cell present the upper value of the band offset.
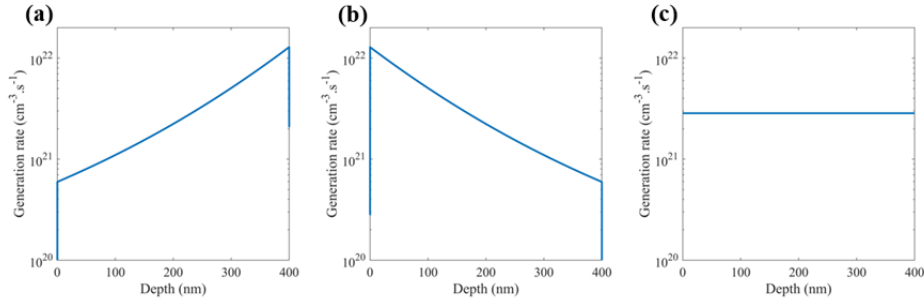
Figure S5: Photogeneration rate across the perovskite layer for the three structures in Fig 2 (main text). Depth scale starts from HTL interface (0 nm) to the ETL interface (400 nm). (a) n-i-p structure (photogeneration from illumination on ETL side using Lambert's law), (b) p-i-n structure (photogeneration from illumination on HTL side using Lambert's law), (c) symmetrical structure (synthetic constant photogeneration).

Table 3: Parameters defining perovskite materials in the solar cells associated to the results in Figure 2.
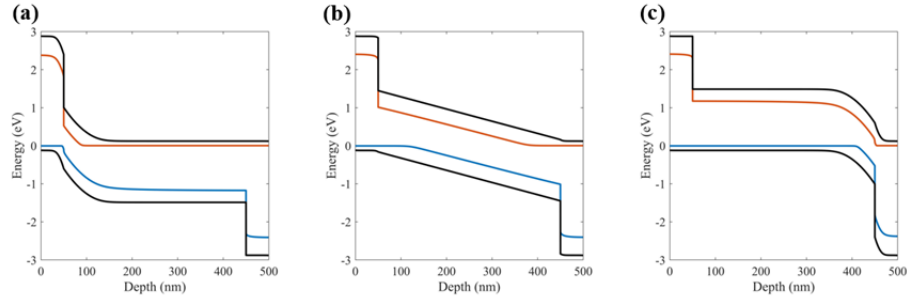
Figure S6: Band diagram of the same perovskite solar cell structure (TiO$_2$/ MAPbI$_3$/Spiro-OMeTAD) at short circuit, for three doping levels using the parameters in table 1. (a) n doping (Nd=10^{17}cm^{-3}), (b) no doping, (c) p doping (N$_d$=10^{17}cm^{-3}).
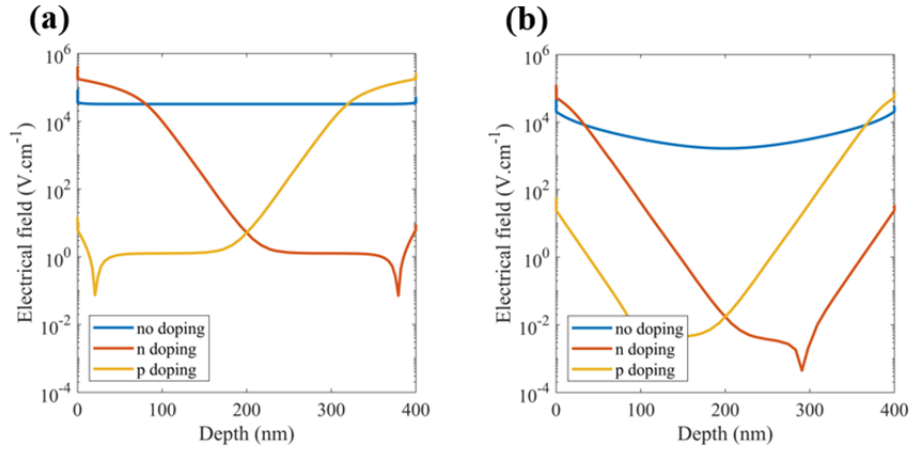

Figure S7: Electrical field intensity across the perovskite layer at (a) short circuit and (b) open circuit, for three doping levels (same cases simulated in the Figure S6).
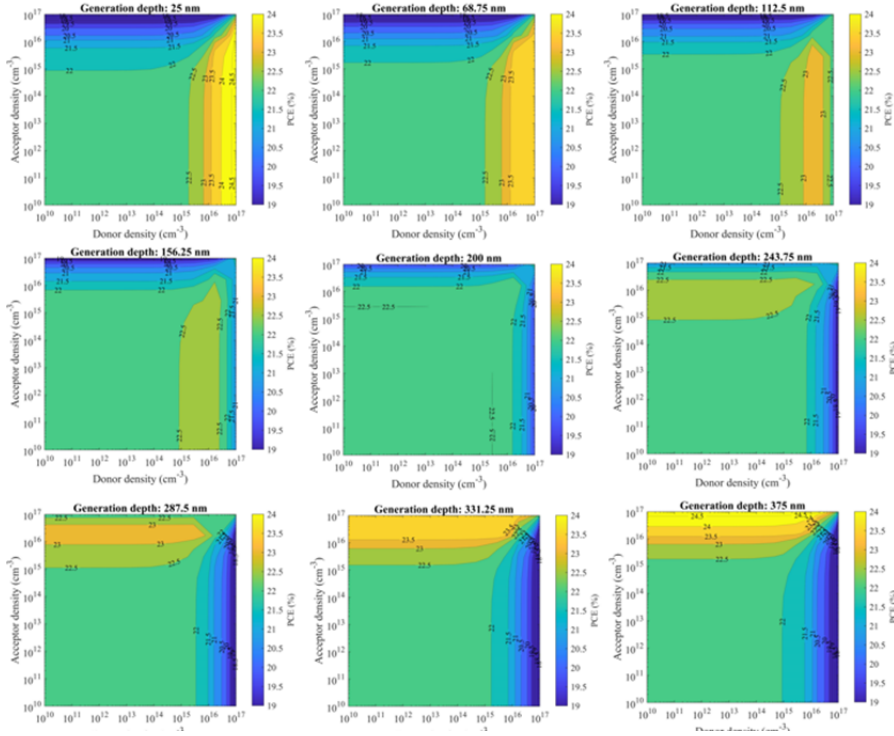
Figure S8: Mapping of the PCE difference depending on electron and hole mobility for the nine square generation profiles at different depth in the perovskite layer. Generation depth is the distance of the square generation profile with respect the HTL layer.

|	Reference	Very good layer	High bulk defects	High interface defects	Low carrier mobilities
Thickness (nm)	400	400	400	400	400
Bandgap (eV)	1.61	1.61	1.61	1.61	1.61
Electron affinity (eV)	3.79	3.79	3.79	3.79	3.79
Relative permittivity	23	23	23	23	23
Nc (cm^{-3})	10^{19}	10^{19}	10^{19}	10^{19}	10^{19}
Nv (cm^{-3})	10^{19}	10^{19}	10^{19}	10^{19}	10^{19}
Carriers thermal velocity (cm.s^{-1})	10^7	10^7	10^7	10^7	10^7
Electron mobility (cm^2.V^{-1}.s^{-1})	1	1	1	1	0.1
Hole mobility (cm^2.V^{-1}.s^{-1})	1	1	1	1	0.1
Radiative recombination coefficient (cm^3.s^{-1})	5.3x10^{-11}	5.3x10^{-11}	5.3x10^{-11}	5.3x10^{-11}	5.3x10^{-11}
Defect density in bulk (cm^{-3})	10^{15}	10^5	10^{17}	10^5	10^5
Defect density at ETL interface (cm^{-2})	10^{12}	10^5	10^5	10^{14}	10^5
Defect density at HTL interface (cm-2)	10^{12}	10^5	10^5	10^{14}	10^5

153
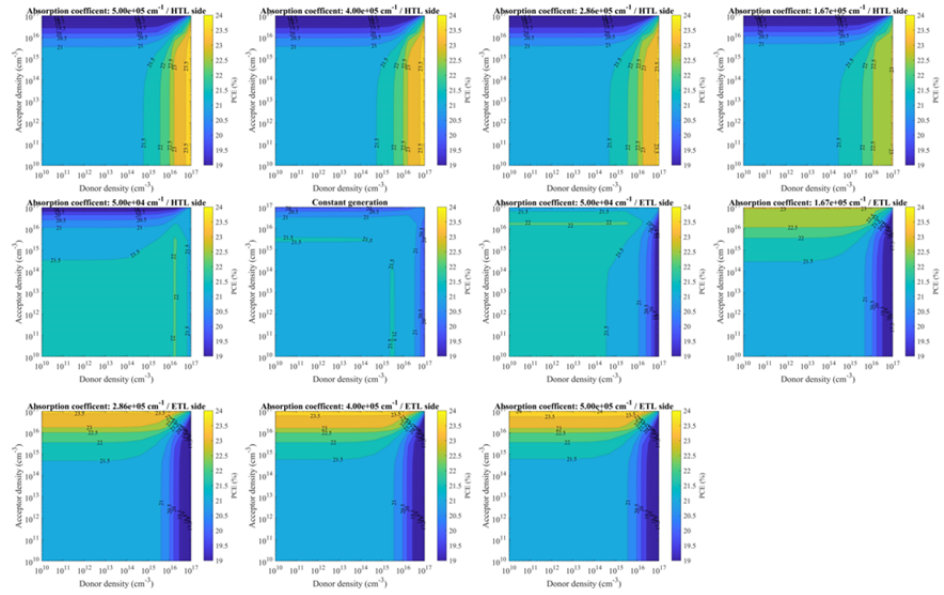
Figure S9: PCE of the reference device as a function of doping level for each of the exponential generation functions. Shows the symmetry between left and right-side illumination.
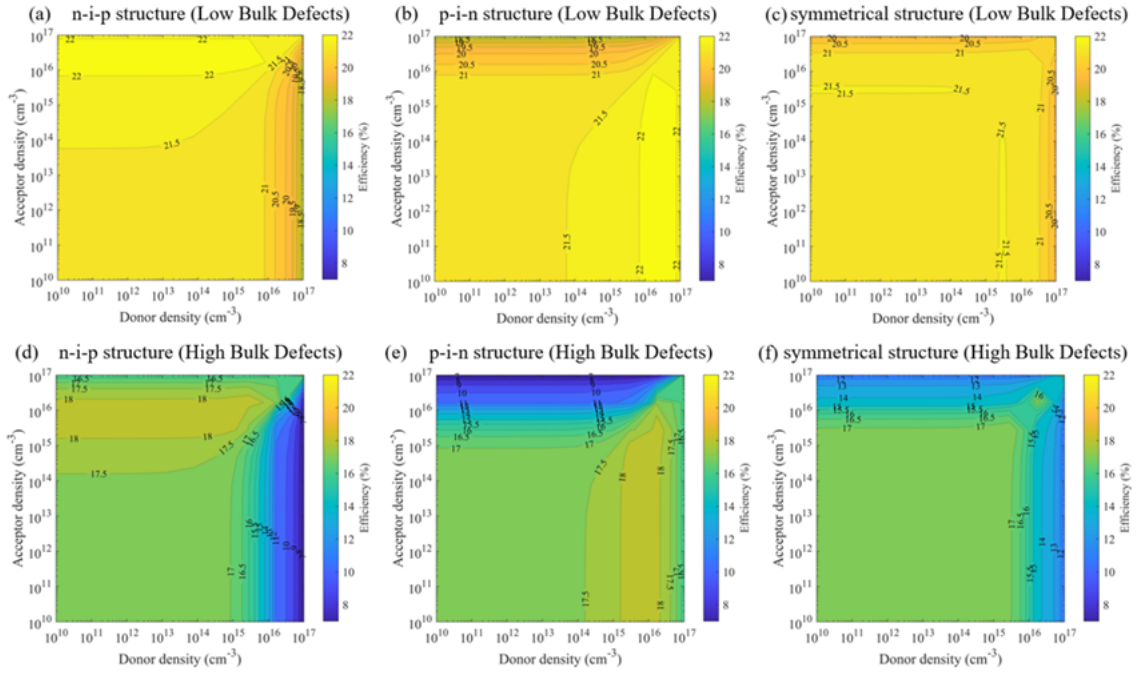
Figure S10: PCE of PSCs using physically realistic parameters for the perovskite layer, and symmetric TLs that have the same band offset, carrier mobilities and doping level. (a) and (d): n-i-p structure (photogeneration from illumination on ETL side). (b) and (e): p-i-n structure (photogeneration from illumination on HTL side). (c) and (f): symmetrical structure (constant generation rate throughout the perovskite layer). (a) to (c) have a defect density of 10^{15} cm^{-3} in the perovskite layer, (d) to (f) have 10^{17} cm^{-3}. Associated data: Table S3 (columns reference cell and high defect cell) and Figures S10 to S12.
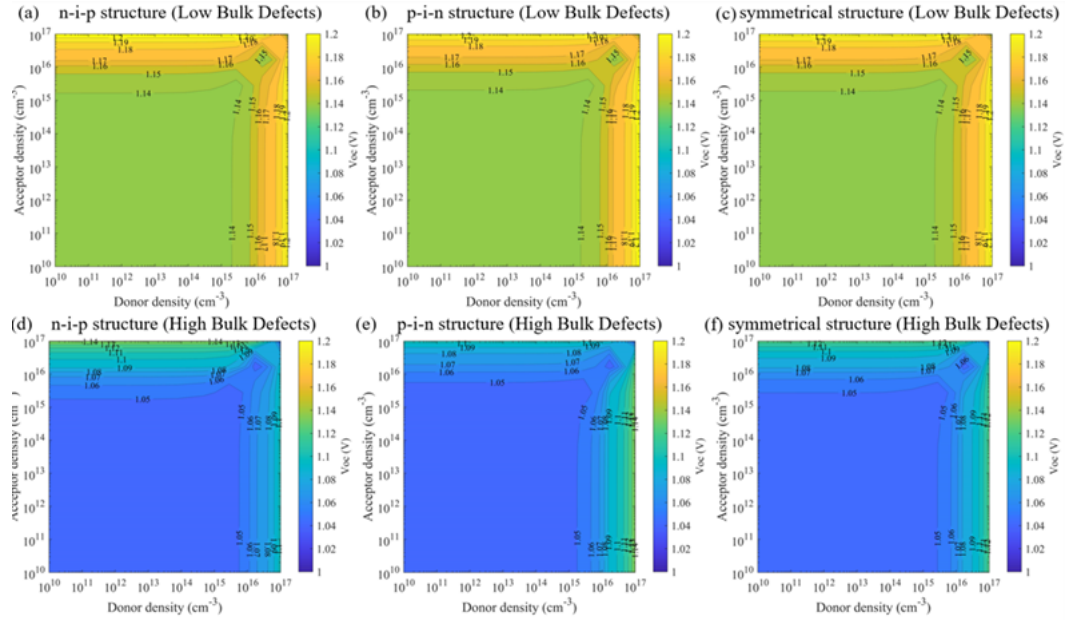
Figure S11: V_{oc} of PSCs simulated in Figure S9 using physically realistic parameters for the perovskite layer, and symmetric TLs that have the same band offset, carrier mobilities and doping level. (a) and (d): n-i-p structure (photogeneration from illumination on ETL side). (b) and (e): p-i-n structure (photogeneration from illumination on HTL side). (c) and (f): symmetrical structure (constant generation rate throughout the perovskite layer). Two defect densities in the perovskite are represented: 10^{15} cm^{-3} ((a) to (c)) and 10^{16} cm^{-3} ((d) to (f)).
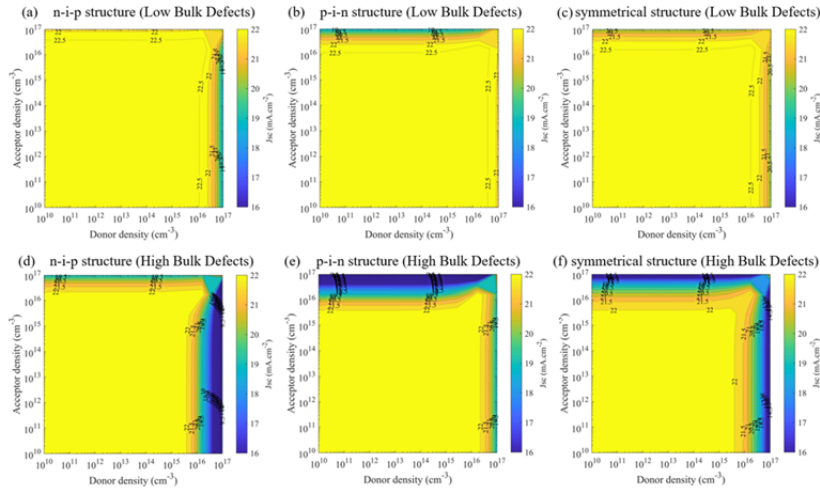
Figure S12: J_{sc} of PSCs simulated in Figure S9 using physically realistic parameters for the perovskite layer, and symmetric TLs that have the same band offset, carrier mobilities and doping level. (a) and (d): n-i-p structure (photogeneration from illumination on ETL side). (b) and (e): p-i-n structure (photogeneration from illumination on HTL side). (c) and (f): symmetrical structure (constant generation rate throughout the perovskite layer). Two defect densities in the perovskite are represented: 10^{15} cm^{-3} ((a) to (c)) and 10^{16} cm^{-3} ((d) to (f)).
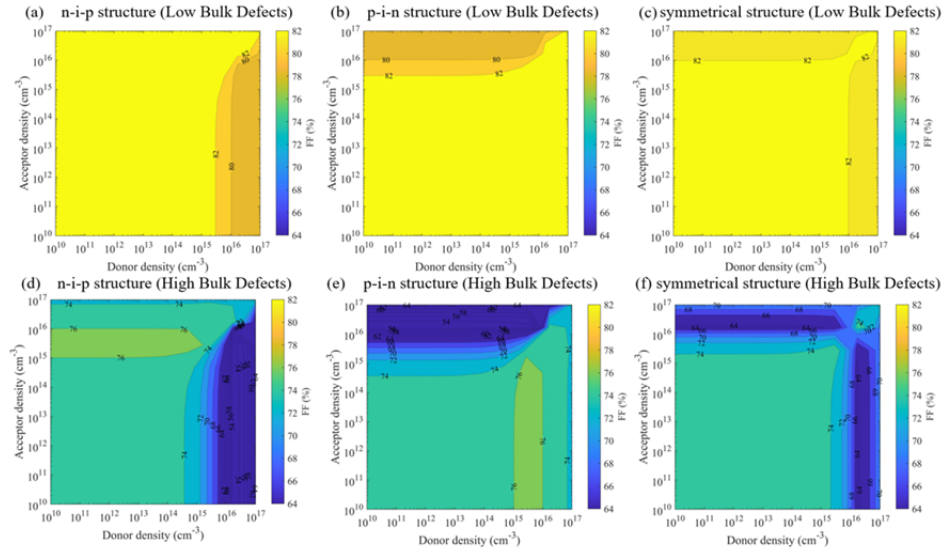
Figure S13: FF of PSCs simulated in Figure S9 using physically realistic parameters for the perovskite layer, and symmetric TLs that have the same band offset, carrier mobilities and doping level. (a) and (d): n-i-p structure (photogeneration from illumination on ETL side). (b) and (e): p-i-n structure (photogeneration from illumination on HTL side). (c) and (f): symmetrical structure (constant generation rate throughout the perovskite layer). Two defect densities in the perovskite are represented: 10^{15} cm^{-3} ((a) to (c)) and 10^{16} cm^{-3} ((d) to (f)).
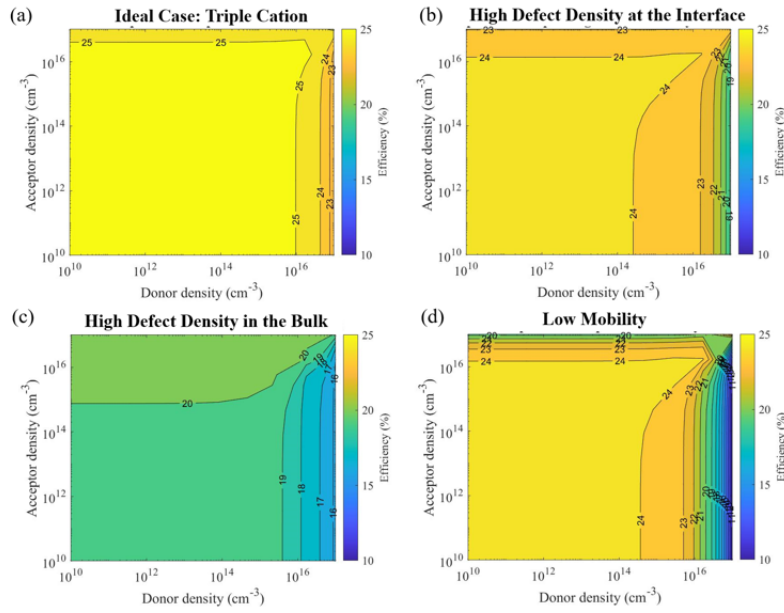
Figure S14: PCE as a function of dopant density when bulk parameters on the perovskite are modified. The parameters changed in each figure are the bulk defect density, the interface defects, and the electron/hole mobility in the perovskite: (a) Ideal Triple Cation/Spiro-OMeTAD 10^5 cm^{-3}, 10^{10} cm^{-2}, 1 cm^2/Vs, (b) High Defect density at the interface: 10^{12}cm^{-3}, 10^{10} cm^{-2}, 1 cm^2/Vs, (c) High Defect Density in the Bulk: 10^5 cm^{-3} , 10^{15} cm^{-2} , 1 cm^2/Vs, and (d) Low mobility in the bulk for electrons and holes: 10^5cm^{-3}, 10^{10} cm^{-2}, 0.1 cm^2/Vs.
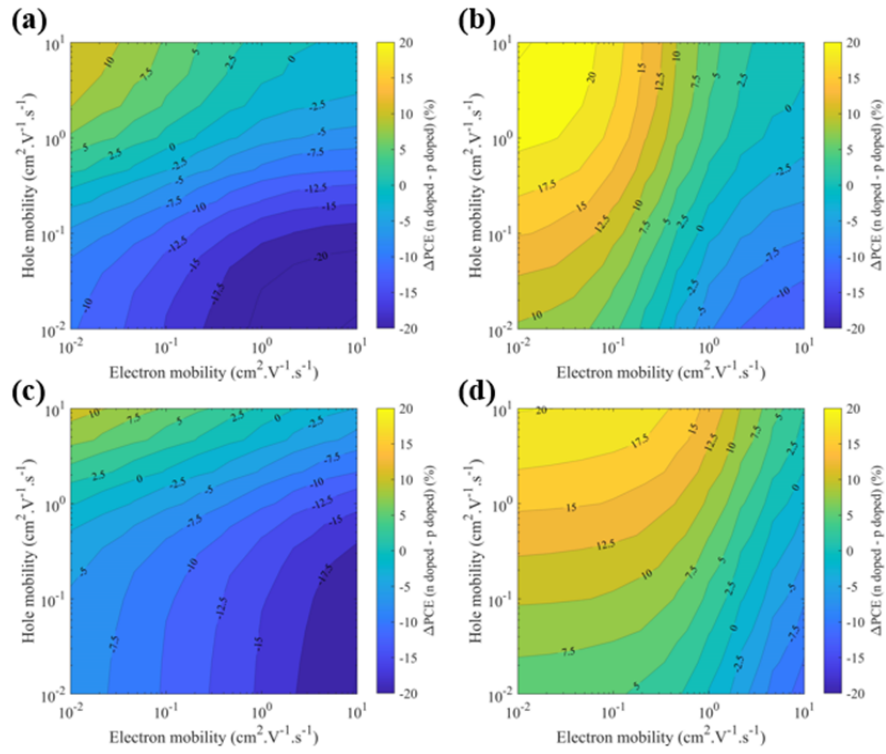
Figure S15: Mapping of the PCE difference between p-type perovskite ($Na=10^{17}cm^{-3}$) and n-type perovskite ($Nd=10^{17}$ cm^{-3}) depending on electron and hole mobility. (a) and (c) are n-i-p, and (b) and (d) are p-i-n configurations. Two defect densities in the perovskite are represented: 10^{15} cm^{-3} ((a) and (b)) and 10^{16} cm^{-3} ((c) and (d)).

Bibliography

[1] T. Hellmann, M. Wussler, C. Das, R. Dachauer, I. El-Helaly, C. Mortan, T. Mayer, and W. Jaegermann, "The difference in electronic structure of mapi and masi perovskites and its effect on the interface alignment to the htms spiro-meotad and cui," *Journal of Materials Chemistry C*, vol. 7, pp. 5324–5332, 2019.

[2] E. Karimi and S. M. Ghorashi, "Investigation of the influence of different hole-transporting materials on the performance of perovskite solar cells," *Optik*, vol. 130, pp. 650–658, 2017.

[3] Y. Raoui, H. Ez-Zahraouy, N. Tahiri, O. E. Bounagui, S. Ahmad, and S. Kazim, "Performance analysis of mapbi3 based perovskite solar cells employing diverse charge selective contacts: Simulation study," *Solar Energy*, vol. 193, pp. 948–955, 2019.

[4] M. Deepa, M. Salado, L. Calio, S. Kazim, S. M. Shivaprasad, and S. Ahmad, "Cesium power: Low cs+ levels impart stability to perovskite solar cells," *Physical Chemistry Chemical Physics*, vol. 19, pp. 4069–4077, 2017.

[5] J. Peng, D. Walter, Y. Ren, M. Tebyetekerwa, Y. Wu, T. Duong, Q. Lin, J. Li, T. Lu, M. A. Mahmud, O. L. C. Lem, S. Zhao, W. Liu, Y. Liu, H. Shen, L. Li, F. Kremer, H. T. Nguyen, D. Y. Choi, K. J. Weber, K. R. Catchpole, and T. P. White, "Nanoscale localized contacts for high fill factors in polymer-passivated perovskite solar cells," *Science*, vol. 371, pp. 390–395, 2021.

[6] M. Shahiduzzaman, M. I. Hossain, S. Otani, L. L. Wang, S. Umezu, T. Kaneko, S. Iwamori, K. Tomita, Y. H. Tsang, M. Akhtaruzzaman, D. Knipp, J. M. Nunzi, M. Isomura, J. A. Zapien, and T. Taima, "Low-temperature treated anatase tio2 nanophotonic-structured contact design for efficient triple-cation perovskite solar cells," *Chemical Engineering Journal*, vol. 426, p. 131831, 2021.

[7] T. Minemoto and M. Murata, "Device modeling of perovskite solar cells based on structural similarity with thin film inorganic semiconductor solar cells," *Journal of Applied Physics*, vol. 116, 2014.

[8] G. Xosrovashvili and N. E. Gorji, "Numerical analysis of tio2/cu2znsns4 nanostructured pv using scaps-1d," *Journal of Modern Optics*, vol. 60, pp. 936–940, 2013.

[9] T. Leijtens, I. K. Ding, T. Giovenzana, J. T. Bloking, M. D. McGehee, and A. Sellinger, "Hole transport materials with low glass transition temperatures and high solubility for application in solid-state dye-sensitized solar cells," *ACS Nano*, vol. 6, pp. 1455–1462, 2 2012.

[10] K. Kalyanasundaram, *Dye-sensitized Solar Cells (Fundamental Sciences: Chemistry)*. EPFL Press, 2010.

[11] U. Mandadapu, S. Vedanayakam, K. Thyagarajan, M. Reddy, and B. Jagadeeshbabu, "Design and simulation of high efficiency tin halide perovskite solar cell," *International Journal of Renewable Energy Research*, 2017.

[12] S. J. Fonash, *Solar Cell Device Physics (2nd Edition)*. Academic Press, 2010.

[13] C. Motta, F. El-Mellouhi, and S. Sanvito, "Charge carrier mobility in hybrid halide perovskites," *Scientific Reports*, vol. 5, 2015.

[14] C. Wehrenfennig, G. E. Eperon, M. B. Johnston, H. J. Snaith, L. M. Herz, C. Wehrenfennig, G. E. Eperon, M. B. Johnston, H. J. Snaith, and L. M. Herz, "High charge carrier mobilities and lifetimes in organolead trihalide perovskites," *Advanced Materials*, vol. 26, pp. 1584–1589, 3 2014.

[15] L. Schmidt-Mende and M. Grätzel, "Tio2 pore-filling and its effect on the efficiency of solid-state dye-sensitized solar cells," *Thin Solid Films*, vol. 500, pp. 296–301, 4 2006.

Chapter 3

Discussion

The objectives of this chapter are to clarify some of the caveats of the publications included in this doctoral thesis, point out some of the claims which need further evidence as well as to put into better context some of the results. This is largely due to developments in both the literature and the authors' understanding of the field that have occurred since the publication of these articles. For sake of simplification, references [1–3] will correspond to the articles in sections 2.1, 2.2 and 2.3 that make up this thesis.

The apparent contradiction that rubidium can both simultaneously improve film properties while decreasing stability [1] is in fact completely consistent with published work on HaPs. It has previously been shown that the addition of 5% to 10% of rubidium to high performance triple cation devices led to an improvement in device performance and the removal of lead excess and yellow-phase impurities [4]. This is consistent with our findings in that the substitution of 6% of caesium with rubidium atoms led to an observable increase in film quality and absorption coefficient [1], which could be caused by a reduction in defect density. At the same time, caesium-lead HaP are known to be thermodynamically unstable [5] and they have been shown to be made more stable by tuning their tolerance factor [6]. Due to the small ionic radius of caesium and the rather large one of iodine, one can either substitute caesium for a larger atom or substitute iodine for a smaller one, such as bromine, in order to improve stability. Applying this logic in reverse, since rubidium has a smaller radius than caesium, one would expect HaP stability to be inversely proportional to rubidium content, which is what was observed [1].

Whilst the aforementioned reason may explain why there has been no previous investigation into chemically doping $CsPbIBr_2$ with rubidium, the fact that rubidium appears to occupy caesium vacancies [1] is itself an interesting finding which has implications for its use in quadruple cation devices. This substitutional behaviour is not a given since rubidium is too small to form a perovskite structure by itself [4] and previous studies, which were

shown to be incorrect [7], have made claims about small halides being able to occupy iodine vacancies in the lattice [8]. The observed change in band gap energy as rubidium content was increased is also an interesting finding, which as far as we are aware was not documented in the literature previously.

There have also been several developments with respect to the context of the findings in Chapter 2.2. At the time of publication, there was only one other report from Zhang and coworkers [9] that used an antisolvent quenching technique while all other reports relied on the natural drying of the precursor solution which leads to an especially poor film quality. Fortunately, there are now a plethora of reports using antisolvent quenching to produce CsPbIBr$_2$ [10–12], some of which have further refined our method by adding co-solvents [13] or additives [14]. Some of these publications also point out benefits of using isopropanol, such as it being nontoxic and more environmentally friendly [14]. Since publication, there have been several new insights which would have been included in the discussion section of Chapter 2.2 had they been known at the time.

Firstly, as mentioned in the Methods section of Chapter 1, Taylor and coworkers have established that different types of antisolvents should be applied in different ways depending on their miscibility and solubility [15]. While in the discussion section of Chapter 2.2 we pointed out that the first antisolvent quenching method, pioneered by Zhang and coworkers [9], relied on using diethyl ether which is not miscible with the host solvents, we overlooked the fact that using larger quantities may have yielded higher quality films. Similarly, toluene is not miscible with the host solvents, therefore we may have obtained better results if more toluene was used.

Secondly, upon further reflection it seems that the most likely explanation for the tapering off of the crystal quality when isopropanol was applied later than 10 seconds was likely due to drying induced crystallisation. It is possible that around this period the film started drying and crystallising in the same way that it would without the antisolvent quenching, making the antisolvent quenching step less effective.

Another important point that could have been further elucidated in Chapter 2.2 was that during the screening of the antisolvents, toluene and chlorobenzene were rejected based on their poor surface morphology, as seen using SEM. However, at the same time these films showed the highest PL emission, which is usually indicative of an improved HaP film. The decision to reject these antisolvents, despite the PL results, was a result of the following reasoning; interfaces tend to play an important role in current extraction, and high-performance devices tend to use homogeneous HaP films, with low surface roughness, since it leads to better contact between the HaP and the HTL. Small crystals can also have high PL emission in some instances due to the reduced number of surface defects. This can be seen in the limiting case of quantum dots, which are strong emitters.

Finally, we also believe that the simulations used to model CsPbIBr$_2$

HaPSCs could be improved. Firstly, the increased open circuit voltage that was observed when using TiO_2 was not explained, and it is most likely due to the band offset at the perovskite-ETL interface limiting the quasi-Fermi level splitting. In the simulations, the electron affinity of the $CsPbIBr_2$ HaP was taken to be 3.49eV, which was significantly closer to that of TiO_2 at 4.22eV than ZnO at 4.4eV. The result and analysis behind the cell using ZnO without an HTL has also been called into question. The text refers to differences in parasitic absorption; however, these cells are being simulated in the regular (n-i-p) configuration and therefore these losses should be negligible. The curve also has an S-shape, which is sometimes seen in poor cells. An S-shape IV curve may occur when at one of the contacts an electric field impedes the correct current flow. While V_{OC} may not be impacted by this field since there is no current flow at this working point, as soon as the cell starts conducting current the field impedes the flow and reduces the number of carriers that can be collected at the contact. A possible explanation for the observed behaviour was that there was a high amount of interface recombination at HaP-HTL interface for the ZnO-based cells, which was removed during the removal of the spiro layer, leading to a significant reduction in recombination, hence the increases in V_{OC}. That said, to our best understanding, it is unusual that the ZnO cell should outperform one based on TiO_2 when no HTL was used as well as having increases in VOC when an HTL was not used, making the repetition of these results necessary to substantiate these claims.

The 3rd work that makes up this doctoral thesis, found in Chapter 2.3, already includes an extensive analysis of the state of the art, making the inclusion of another one here redundant. That said, one thing that has come to our attention since its publication is that SCAPS can, in some cases, be limited in modelling HaPSCs because it fails to capture the dynamic nature of defects and ions. This could be especially important in the case when considering high densities of electronically active defects since mobile charges can screen the electric field and change the space-charge region. That said, given that it was only recently published, we are glad to see that our work has already been cited by several different groups and we expect the findings to be relevant for the further development of future high-performance devices.

Bibliography

[1] A. W. Stewart, A. Bouich, and B. Marí, "Inorganic perovskites improved film and crystal quality of cspbibr2 when doped with rubidium," *Journal of Materials Science: Materials in Electronics*, pp. 1–9, 9 2021.

[2] A. W. Stewart, A. Bouich, and B. M. Soucase, "Enhancing the stability and crystallinity of cspbibr2 through antisolvent engineering," *Journal of Materials Science*, 2021.

[3] A. Stewart, A. Julien, D. Regaldo, P. Schulz, B. M. Soucase, D. Ceratti, and P. López-Varo, "Shedding light on electronically doped perovskites," *Materials Today Chemistry*, vol. 29, p. 101380, 4 2023.

[4] M. Saliba, T. Matsui, J. Y. Seo, K. Domanski, J. P. Correa-Baena, M. K. Nazeeruddin, S. M. Zakeeruddin, W. Tress, A. Abate, A. Hagfeldt, and M. Grätzel, "Cesium-containing triple cation perovskite solar cells: Improved stability, reproducibility and high efficiency," *Energy and Environmental Science*, vol. 9, pp. 1989–1997, 2016.

[5] D. B. Straus, S. Guo, A. M. Abeykoon, and R. J. Cava, "Understanding the instability of the halide perovskite cspbi3 through temperature-dependent structural analysis," *Advanced Materials*, vol. 32, pp. 1–8, 2020.

[6] G. Kieslich, S. Sun, and A. K. Cheetham, "Solid-state principles applied to organic–inorganic perovskites: new tricks for an old dog," *Chemical Science*, vol. 5, pp. 4712–4715, 10 2014.

[7] M. Grätzel, "The light and shade of perovskite solar cells," *Nature Materials 2014 13:9*, vol. 13, pp. 838–842, 8 2014.

[8] M. M. Lee, J. Teuscher, T. Miyasaka, T. N. Murakami, and H. J. Snaith, "Efficient hybrid solar cells based on meso-superstructured organometal halide perovskites," *Science (New York, N.Y.)*, vol. 338, pp. 643–647, 11 2012. Shows perovskite can act as an ETL.

[9] B. Zhang, W. Bi, Y. Wu, C. Chen, H. Li, Z. Song, Q. Dai, L. Xu, and H. Song, "High-performance cspbibr2 perovskite solar cells: Effectively promoted crystal growth by antisolvent and organic ion strategies," *ACS Applied Materials and Interfaces*, vol. 11, pp. 33868–33878, 2019.

[10] H. Wang, M. Yang, W. Cai, and Z. Zang, "Suppressing phase segregation in cspbibr2films via anchoring halide ions toward underwater solar cells," *Nano Letters*, vol. 23, pp. 4479–4486, 5 2023.

[11] P. Ghosh, J. Bruckbauer, C. Trager-Cowan, and L. K. Jagadamma, "Crystalline grain engineered cspbibr2 films for indoor photovoltaics," *Applied Surface Science*, vol. 592, p. 152865, 8 2022.

[12] F. Wang, D. Duan, M. Singh, C. M. Sutter-Fella, H. Lin, L. Li, P. Naumov, and H. Hu, "Ionic liquid engineering in perovskite photovoltaics," *ENERGY & ENVIRONMENTAL MATERIALS*, 5 2022.

[13] J. Yang, H. Yu, S. Wu, C. Cai, J. Gao, X. Lu, X. Gao, L. Shui, S. Wu, and J. M. Liu, "A mixed antisolvent-assisted crystallization strategy for efficient all-inorganic cspbibr2perovskite solar cells by a low-temperature process," *ACS Applied Energy Materials*, vol. 5, pp. 2881–2889, 3 2022.

[14] Q. He, H. Zhang, S. Han, Y. Xing, Y. Li, X. Zhang, and R. Wang, "Improvement of green antisolvent-isopropanol and additive-thiourea on carbon based cspbibr2 perovskite solar cells," *Materials Science in Semiconductor Processing*, vol. 150, p. 106940, 11 2022.

[15] A. D. Taylor, Q. Sun, K. P. Goetz, Q. An, T. Schramm, Y. Hofstetter, M. Litterst, F. Paulus, and Y. Vaynzof, "A general approach to high-efficiency perovskite solar cells by any antisolvent," *Nature Communications 2021 12:1*, vol. 12, pp. 1–11, 3 2021.

Chapter 4

Conclusion

The three published works that comprise this PhD thesis have contributed towards the improvement of HaPSC stability and performance. The first two works are focused on the development of $CsPbIBr_2$ thin films using solvent engineering, whereas the third provides the framework for further advances in high performance devices using electronic doping techniques.

In the 1st work, the effect of substituting caesium for rubidium in $CsPbIBr_2$ was investigated. Firstly, confirmation that rubidium atoms are occupying caesium vacancies was inferred independently from shifts in XRD interference maxima and EDS results. Substitution of 6% of caesium atoms with rubidium was shown to provide beneficial effects to film morphology, where it resulted in the best film coverage and largest grain size. Optically, 6% also resulted in the highest absorption coefficient. Analysis based on PL emission and absorption both suggested a consistent, albeit rather small, increase in band gap energy proportional to rubidium content. At the same time, films were shown to become less stable as rubidium made up an increasingly large part of the composition.

The 2nd published work developed an antisolvent quenching technique for one-step spin coated $CsPbIBr_2$. Characterisation of the thin films demonstrated the formation of highly crystalline and oriented cubic perovskite layers with a thickness of 296nm. All films showed the formation of iodine rich phases under illumination. Common antisolvents were screened before optimising the time-wise application of the best antisolvent. During the initial screening, FESEM micrographs revealed the formation of inhomogeneous films when toluene or chlorobenzene was applied, which led to their subsequent rejection as suitable antisolvent candidates. Crystallite sizes in the films, which were inferred from the XRD spectra using the Scherrer equation, revealed that only isopropanol led to an improvement. All other films led to a dimming of the XRD spectra as well as an inhomogeneous distribution of crystallites, which were also smaller on average than the reference film where no antisolvent was used. Based upon these results, isopropanol

was selected as the most promising antisolvent and its application was further optimised by changing the application time. Varying the application time from 5 to 20 seconds, in steps of 5 seconds, always resulted in films with brighter XRD spectra than the reference film. However, a significant jump in PL emission and XRD spectra brightness was observed when the antisolvent was applied at 10 seconds. Increasing the application time past this value resulted in a slow decrease of these metrics.

To determine the effect of antisolvent treatment on thin film stability, a novel procedure based on the quantification of XRD spectra was employed and results were compared with a qualitative analysis based on absorbance spectra of the same films. The findings of this method were largely consistent with the results in the previous sections, namely the antisolvent screening tests and the optimisation of the time-wise application of isopropanol. In contrast to the reference sample, the application of toluene, diethyl ether and chlorobenzene all led to the apparition of new XRD maxima, evidencing the formation of new and unwanted crystalline phases which were byproducts of accelerated phase degradation. Apart from when isopropanol was applied too early, all films treated with isopropanol after 10 seconds or later resulted in decreases in XRD spectra brightness and no new crystalline phases being formed. Moreover, even after the films had been aged for 5 weeks in ambient air, XRD spectra of the 10 and 15 second films were higher than the freshly prepared reference film's, demonstrating their vastly enhanced stability. These results were consistent with a qualitative analysis of stability based on film absorption, in which films treated with isopropanol showed the smallest change after aging. The application of isopropanol after 10 seconds or later also resulted in only small changes after ageing, and were comparable to the freshly prepared reference film, even after ageing.

For completeness, devices were simulated using measured film properties. The highest obtained PCE was 13.7%, which was only slightly higher than experimentally produced devices. These simulations also highlighted the importance of selecting appropriate transport layers.

The 3rd published work in this doctoral thesis consisted of investigating the origin and dependence of optimal electronic doping levels in HaPSCs, using computational simulations. Simulations of realistic devices revealed that up to a 6% difference in PCE can be obtained depending on whether the HaP is heavily n-doped or p-doped. The impact of transport layer properties was systematically studied, leading to the conclusion that the underlying factors leading to the dependence of PCE on HaP doping level dependence was ultimately due to the properties of the HaP absorber layer itself. Optimal doping levels in realistic devices were then shown to be a consequence of the low carrier mobilities and high absorption coefficients of solution-based HaP thin films, with the former causing photogenerated carriers to become highly localised while the latter impeding their successful extraction.

More generally, four regimes were shown to exist, in which different physical processes limited the PCE of the HaPSC device. Given a certain HaP thickness, the probability of a carrier type recombining before extraction is a function of that carrier's mobility. This means that there are four limiting cases when either (i) all charges are extracted because mobilities are very high (ii) electron and hole mobilities are comparable (iii) electron mobility is low with respect to hole mobility (iii) hole mobility is low with respect to electron mobility. To reduce the probability of recombination in the latter two cases, it is better to make the carrier which is difficult to extract the majority carrier. Optimal doping levels in region (ii), thought to be the case in most real devices, are dependent on a photogenerated carrier profile within the HaP layer. This profile is directly influenced by illumination conditions and device architecture since more carriers are photogenerated near the front of the device. This results in conventional devices, commonly known as n-i-p devices, operating more efficiently when the HaP is p-doped, whereas inverted devices when the HaP is n-doped.

4.1   Future work

This doctoral thesis has laid the foundation for future work in the commercialisation and large-scale deployment of HaPSCs. On one hand, it has contributed towards advancing the quality of wide-bandgap HaP compositions. These wide-band gap HaP compositions are expected to be useful for producing tandem devices as well as serving as a platform for investigating important processes occurring in HaPs, such as halide segregation. On the other hand, the third article presented in this thesis highlights the importance of electronic doping in HaP devices. Moreover, it develops the theory behind these systems and connects these results with existing experimental work found in the literature. In this way, it highlights potential experimentally-based avenues of research for the development of high-performance devices with optimised HaP doping levels. These will be the subject of future investigations.